Investigation of the three-dimensional shear layer between confined coaxial jets with swirl

Christian Nayeri
aus Berlin

Vom Fachbereich 10
Verkehrswesen und Angewandte Mechanik
der Technischen Universität Berlin
zur Erlangung des akademischen Grades
Doktor-Ingenieur
genehmigte Dissertation

Promotionsausschuß:
Vorsitzender: Prof. Dr.-Ing. H. Schoop
Gutachter: Prof. Dr.-Ing. H.-H. Fernholz,
Prof. Dr. rer.nat. A. Dillmann, Dr.-Ing. D. Hilberg

Tag der wissenschaftlichen Aussprache: 16. Juni 2000

Berlin 2000

D 83

Contents

Abstract

This is an experimental investigation of the flow structure and turbulence characteristics of a turbulent axisymmetric shear layer between two primary streams under the influence of three-dimensional stationary boundary conditions. These conditions result from skewing the primary streams relative to the trailing edge. Two configurations were investigated: both primary streams were parallel but skewed relative to the trailing edge (i.e. slanted trailing edge) and the primary streams were non-planar (i.e. had cross-shear). Although these flows are simplified models, their understanding should provide more insight into the mechanisms of real life three-dimensional shear flows than studies on classical two-dimensional shear flows have done to date.

The investigated shear layers were generated at the interface between two coaxial jets with different axial velocities. Additionally, azimuthal velocity components were imposed by means of a swirl generator on the shear layer either in the same or the opposite direction. Results from various experimental measurements including 4-sensor hot-wire probes, hot-wire rakes and visualizations indicate an increase of the total turbulent kinetic energy, and of the growth rates compared to cases with no skewing. Further, the vortex rings resulting from the the Kelvin-Helmholtz instability were deformed by coherent structures having axis not parallel to the trailing edge. It is assumed that these structures are helical vortices competing with the vortex rings in a complex structural manner which lead to the observed increase of the turbulent quantities.

Zusammenfassung

Diese Arbeit beinhaltet die experimentelle Untersuchung der Strukturen und Turbulenzeigenschaften einer turbulenten, axialsymmetrischen Scherschicht zwischen zwei Primärströmen unter Einfluß dreidimensionaler, stationärer Randbedingungen. Diese Bedingungen werden durch die schräge Anordnung der Primärströme relativ zu der Abströmkante erreicht. Zwei Konfigurationen wurden untersucht: Im erstem Fall sind beide Primärströme parallel zueinander aber schräg zur Abströmkante (Scherschicht mit schräger Abströmkante), und im zweiten Fall sind die Primärströme nicht parallel zueinander (zusätzliche Scherung in Querrichtung). Obwohl diese Strömungen Vereinfachungen darstellen, trägt ihr Verständnis zu einem besseren Einblick in die Mechanismen von realen dreidimensionalen Strömungen bei, als die bis heute durchgeführten Untersuchungen in klassischen zweidimensionalen Scherströmungen.

Die untersuchten Scherschichten wurden an der Berührungsfläche zweier koaxialer Strahlen erzeugt, die unterschiedliche axiale Geschwindigkeiten besaßen. Zusätzlich wurde Drall (azimuthale Geschwindigkeitskomponente) auf die einzelnen Strahlen über eine Drallerzeugereinheit aufgeprägt. Es konnte entweder gleichsinniger Drall oder gegensinniger Drall aufgeprägt werden.

Die Ergebnisse der verschiedenen Untersuchungsmethoden inklusiver 4-Drahtsonden-Messungen, Messungen mit Hitzdrahtrechen und Sichtbarmachungen zeigen einen Anstieg der gesamten turbulenten Energie und der Ausbreitungsraten verglichen mit den nicht-schrägen oder nicht-gekreuzten Fällen. Zusätzlich wurden die Wirbelringe, die von der Kelvin-Helmholtz-Instabilität herrühren, durch schräge (nicht parallel zur Abströmkante) kohärente Strukturen verformt . Es wird angenommen, dass diese Strukturen spiralfömige Wirbel sind, die mit den Wirbelringen interagieren und zu dem erhöhtem Niveau der turbulenten Strömungsgrößen beitragen.

Vorbemerkung

Die vorliegende Arbeit entstand während meiner Tätigkeit als wissenschaftlicher Mitarbeiter am Centre d'Études Aérodynamiques et Thermiques (CEAT) in Poitiers und am Hermann-Föttinger-Institut für Strömungsmechanik der Technischen Universität Berlin (HFI). Finanziert wurde das Projekt durch die europäische Kommission und durch die Deutsche Forschungsgemeinschaft (DFG). Beiden Institutionen danke ich an dieser Stelle.

Meine besonderer Dank gilt Herrn Prof. Dr.-Ing. Heinrich E. Fiedler der dieses Projekt initiiert und mich ständig fachlich und moralisch unterstützt hat. Durch sein tragisches und vorzeitiges Ableben konnte er nicht an dem Abschluß dieser Arbeit teilhaben.

Bei Herrn Prof. Dr.-Ing. H.-H. Fernholz bedanke ich mich für seine vorbehaltslose Bereitschaft als Nachfolger von Prof. Dr.-Ing. Fiedler, die Betreuung dieser Arbeit in der Abschlußphase übernommen zu haben.

Ich danke ebenfalls dem Team in Poitiers: Jean-Paul Bonnet, Joel Delville, Henry Garem und Stefan Beharélle. Sie haben mich in jeder Hinsicht unterstützt und mir durch ihre herzliche Art das Gefühl gegeben Teil einer französischen Familie zu sein.

Für die fachliche, technische und menschliche Unterstützung danke ich auch meinen Kollegen in Berlin: Dipl. Ing. Bastian Blümel und Dipl. Ing. René Spieweg, die meine EDV-Probleme stets zu lösen wussten; Dipl. Ing. Jork Rother, der für mich Versuche durchführte; Körling Pölkow, dessen handwerklichen Fähigkeiten ich meinen Windkanal verdanke; Dr.-Ing. Olaf König, dem "alten Hasen" des Labors, der stets für fachliche Anregung sorgte und natürlich Herr Dipl.-Ing. Rainer Nagel ohne dessen Ordnungsinn die Arbeit im Labor nur halb so effizient gewesen wäre.

Ich bedanke mich bei allen Mitarbeitern des HFI inbesondere bei Herrn Dipl.-Ing. Leutz und Frau Lindemann, deren Einsatz die Bewältigung aller organisatorischen Probleme ermöglichte. Allen Mitarbeitern der Metall-Werkstatt, des Sondenlabores und Herrn Franke von der Holzwerkstatt danke ich für ihre Werke und Ratschläge, ohne die mein Versuchsaufbau nicht denkbar gewesen wäre.

Mein herzlicher Dank gilt meiner Frau, Manuela Nayeri, die mir durch ihre

Liebe und Unterstützung die Fertigstellung dieser Arbeit ermöglichte, obwohl sie in dieser Zeit unsere beiden Töchter, Rahel und Daria, zur Welt brachte.

1. List of notations

latin letters

b	geometric shear layer thickness
D_0, D_1	jet exit diameter: inner jet, outer jet, respectivly
$\underline{C}_{con}$	convection velocity vector
$\underline{C}$	velocity vector
$\overline{\underline{C}}$	time or ensemble averaged velocity vector
f	frequency
G_φ	angular momentum
G_x	axial momentum
$K_\alpha(\alpha,\beta), \quad K_\beta(\alpha,\beta), \quad K_C(\alpha,\beta),$	non-dimensionalized coefficients for 4-wire probe measurement
P	pressure
t	time
R_0, R_1	jet exit radius inner jet, outer jet, respectivly
Re_D	Reynoldsnumber based on $\overline{U}D/\nu$
Re_Θ	Reynoldsnumber based on $\overline{U}\Theta/\nu$
r	radial coordinate
S	Swirl number base on $\frac{G_\varphi}{RG_x}$
S_W	Swirl number based on $\overline{W}_{max}/\overline{U}_0$
St	Strouhal number
St_{δ_ω}	Strouhal number based on the vorticity thickness

latin letters (continued)

$\Delta\overline{W}^{\star}$	modified velocity difference based on $\overline{W}_0\ r_0 - \overline{W}_1\ r_1$
$\overline{U}$,$\overline{V}$, $\overline{W}$	time averaged velocity components corresponding to the directions *x*, *y*, *z*
$\overline{U}_b$	bulk axial velocity at the jet exit based on the volume flow rate
$\overline{u'^2}, \overline{v'^2}, \overline{w'^2}$	fluctuating parts of the velocity components
$y_{0.05}, y_{0.5}, y_{0.95}$	isotachs defined by $(\overline{U} - \overline{U}_1)/(\overline{U}_0 - \overline{U}_1)$=0.05, 0.5 and 0.95
x, y, z	cartesian coordinates
x^*, y^*, z^*	cartesian coordinates system where x^* is perpendicular to the trailing edge

greek letters

α, β	flow angles defining $\underline{C}$
δ_ω	vorticity shear layer thickness
φ	azimuthal angle of the polar coordinate system
λ	shear layer parameter
ν	cinematic viscosity
Ψ_0, Ψ_1	vane angles of the swirl generator; inner jet, outer jet, respectivly
$\underline{\omega}$	instantanious vorticity vector
$\underline{\overline{\omega}}$	time averaged vorticity vector
$\overline{\omega}_x$, $\overline{\omega}_y$, $\overline{\omega}_z$	time averaged vorticity vector components
Θ	momentum loss thickness

2. Introduction

In most practical situations three-dimensional flow-fields are the rule rather than the exception. Examples are the flow past an aircraft wing at incidence where the flow separates from the leading edge and forms a shear layer with non-parallel streams. In the flow field of a lobed mixer, where the upper and lower streams are alternately turned into the troughs, the two streams are locally non-parallel and form an array of counter-rotating streamwise vortices near the mixer. Other examples of three-dimensional shear layers are swirling jets, the flow over sails or tilted roofs. The analysis of the complex character of three-dimensional shear layers is a difficult task and therefore most laboratory investigations are concentrating on two-dimensional configurations. A simple extrapolation of the flow behavior from two-dimensional flows to three-dimensional situations does, however, not necessarily lead to even qualitatively correct results. It seems therefore worthwhile to study elementary three-dimensional shear layers and their interactions to provide a basis of understanding. Elementary three-dimensional shear flows can be understood as constituents or building blocks of more complex flows as in meteorological flows or industrial flows. The aim of the present work is to contribute to the understanding of three-dimensional shear layers by studying an axisymmetric shear layer subjected to three-dimensional stationary boundary conditions. These conditions result from skewing the primary streams relative to the trailing edge. Two configurations are investigated: both primary streams are parallel but skewed relative to the trailing edge (i.e. a situation analog to a slanted trailing edge is generated) and the primary streams are non-planar (i.e. cross-shear is generated).

The research reported in this thesis was carried out both in the Centre d'Études Aérodynamiques et Thermiques (CEAT) in Poitiers (France) and in the Hermann-Föttinger Institute (HFI) in Berlin. It was a part of a collaborative research project where several configurations of three-dimensional shear flows were investigated.

2.1 Background of the investigation

In a preceeding work by Gründel [1] experiments in a shear layer with skewed primary streams were carried out. As can be seen in fig. 2.1 the configuration is symmetrical with respect to the *x*-axis. The resulting velocity profiles consisted of a wake type profile in the *x*-*y*-plane and a shear layer profile in the *y*-*z*-plane. Therefore, characteristic wake structures (Fig. 2.3a) with axes parallel to the trailing edge were formed, which interfered with the shear layer structures (Fig. 2.3 b). This is visualized in a model shown in fig. 2.2. The evolving stationary structures had streamwise orientation (parallel to *x* and the direction of mean vorticity $\overline{\omega}_x$) and were of helical shape. Fotographs from smoke visualizations in fig. 2.3c show these structures.

Additionally, bleeding and suction at the trailing edge were applied to suppress the wake structure. At optimal bleeding or suction rate the wake structures were indeed suppressed while formation of the helical structures was more pronounced.

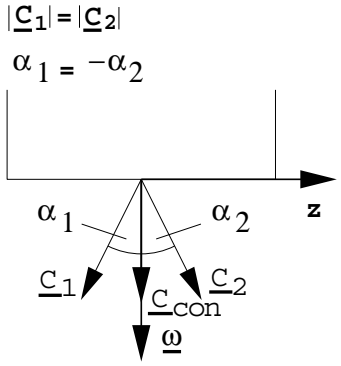

Fig. 2.1: Symmetric flow configuration investigated by Gründel [1], $|\alpha_1| = |\alpha_2| = 15°$, $|\underline{C}_1| = |\underline{C}_2|$

After modifying the experimental setup Gründel performed experiments corresponding to the configuration in fig. 2.4 which is asymmetric due to $|\underline{C}_1| \neq |\underline{C}_2|$.

It was expected that the helical structures would now be convected in spanwise direction. However this behaviour was not observed. It was believed that this unexpected behaviour is a consequence of the plane configuration

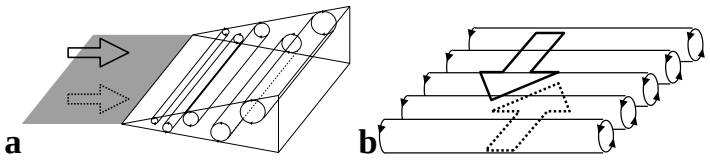

Fig. 2.2: Model of wake structures interfering with shear layer structures by Gründel[1]

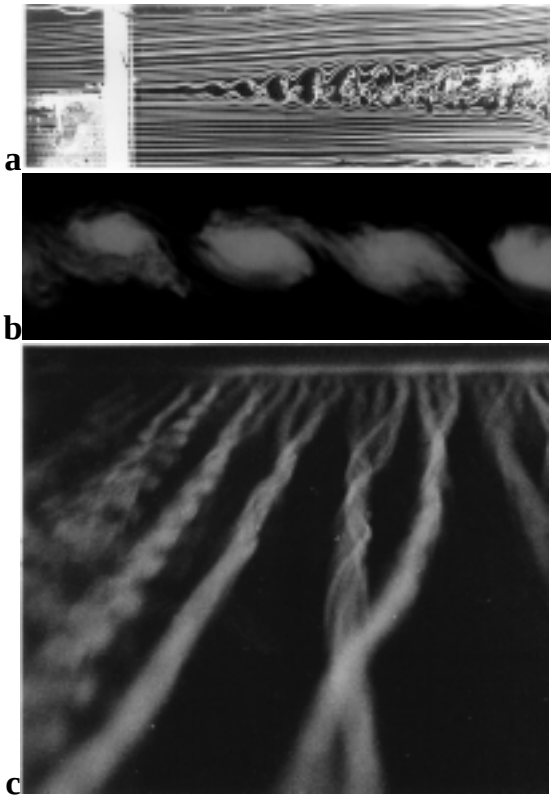

Fig. 2.3: Visualizations from the symmetric flow configuration investigated by Gründel [1]; **a**: streamwise section (x – y-plane) with wake structures visualized by Gründel's co-worker Nayeri [2] (flow from left to right); **b**: Cross-section (y – z-plane)of helical vortices; **c**: top view of helical vortices , flow direction is out of the plane)

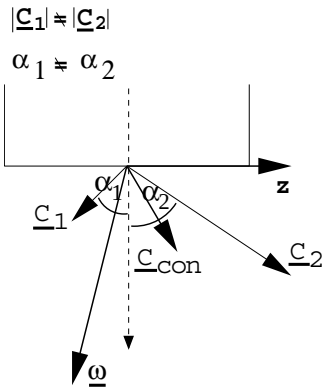

Fig. 2.4: Asymmetric flow configuration investigated by Gründel [1], $|\alpha_1| = |\alpha_2| = 15°$, $|\underline{C}_1| \neq |\underline{C}_2|$

which involves side-walls (the trailing edge is of finite length). This was the motivation for designing an axisymmetric wind tunnel with two rotating (or swirling) coaxial jets (Fig. 2.5). Swirl is generated by a system of rotating perforated plates and honey combs for either stream. The rotating frequency can be adjusted independently for both streams.

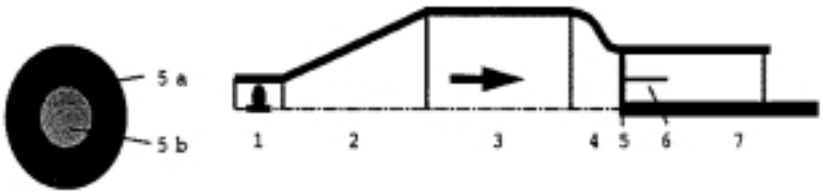

Fig. 2.5: Wind tunnel with two rotating coaxial jets by Gründel [1] (1 axial blower, 2 diffusor, 3 settling chamber, 4 contraction, 5 swirl generator: rotating perforated plates and honey combs for the central stream (5a) and the external stream (5b), 6 cylindrical trailing edge, 7 test-section)

The generated flow profiles corresponded to a top-hat profile for $\overline{U}$ and to a solid-body profile for $\overline{W}$. The results showed stationary streamwise structures in a helical formation about the jet axis. However, the mechanism of swirl generation didn't work satisfactory resulting in pertubations of the flow. Furthermore, the velocity distribution of the azimuthal component corresponding to a solid-body rotation generated constant level of streamwise

vorticity $\overline{\omega}_x$ across the entire flow region. This made the configuration less comparable with the plane configuration where $\overline{\omega}_x$ only exists in the shear layer center (due to cross shear). Under those conditions it was decided not to continue the experiments and the construction of a new wind tunnel was suggested. This was realized in the present investigation.

In the same work experiments in a shear layer with parallel primary streams but with a slanted trailing edge were carried out. This flow configuration is also not symmetric with respect to the *x*-axis. In some visualizations structures parallel to the trailing edge were observed. Numerical investigations of the same configuration by Gründel's coworker Spieweg [3] showed that the primary structures were in fact oriented perpendicular to the streamwise direction which corresponded to the axis of the vorticity $\overline{\omega_z}$ generated by the velocity gradient $\partial\overline{U}/\partial y$. The observed oblique "structures" were waves produced by the piecewise deflection of the primary structures (Fig. 2.6).

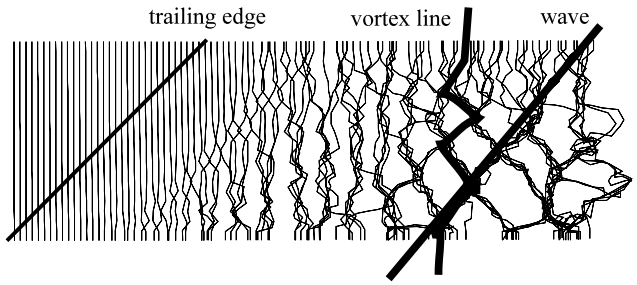

Fig. 2.6: Primary structures (vortex line) retain on the average their orientation parallel to the spanwise direction while their piecewise deflection produces waves parallel to the trailing edge [1]

.

In summary the investigations by Gründel and Spieweg showed that the formation of well defined structures in three-dimensional shear layers are favorized by symmetric flow configurations.

2.2 Classification of three-dimensionality in shear layers

Since three-dimensionality in shear flows is a vague concept due to its manifold manifestations it seems useful to develop a classification of three-dimensional shear layers. In this section a classification is presented and the flow configuration under investigation will be specified.

A general three-dimensional turbulent velocity field is described by $\underline{C} = \overline{\underline{C}}(x,y,z) + \underline{C'}(x,y,z,t)$. The first term on the right hand side denotes the mean or averaged flow, and the second one the fluctuations. However, most experiments are carried out in "basic" configurations where the mean flow is two-dimensional, i.e. $\underline{C} = \overline{\underline{C}}(x,y) + \underline{C'}(x,y,z,t)$. The fluctuating term is always three-dimensional, unless the three-dimensional motion is artificially suppressed as e.g. by magneto-hydrodynamic forces (MHD) or by stratification.

Sometimes the fluctuating term is further divided into a random and a coherent motion (see Hussain [4]), where the coherent part may be two-dimensional, in particular when two-dimensional excitation is applied.

Fiedler et al.[5] presented a generalized concept of three-dimensionality in shear layers by identifying three conditions or mechanisms: (1)three-dimensionality of the basic flow[2] , (2)three-dimensionality of the basic geometry - both being primary causes and (3) secondary three-dimensionality by structural development.

Condition I: Three-dimensionality of the basic flow is the most general condition for three-dimensional properties in turbulent shear flows, when a non-uniform velocity profile represents the main cause leading to three-dimensionality (e.g. fig 2.7a). This kind of three-dimensionality - whatever its upstream cause - is an upstream flow condition for the flow of interest.

When neglecting configurations where the two streams have gradients of scalar properties such as temperature or density, *three-dimensionality of the basic flow* is defined as a non-uniformity of the velocity distribution of at least one of the two streams. In fig. 2.7a the most general type of flow satisfying the above definitions is shown. In this flow both streams have velocity profiles which are non-uniform in the z direction. This is a very complex situation and hardly suited for experimental studies.

In fig. 2.7b-d some simplified configurations of shear layers with a three-dimensional of the basic flow and different λ are sketched ($\lambda = |\underline{C_1} - \underline{C_2}|/|\underline{C_1} + \underline{C_2})|$. The simplification is obtained by the planar arrangement of the primary streams and the variation of the axial velocity component in z-direction. In fig. 2.7b both streams vary symmetrically along the span, so that λ becomes zero at $z = 0$. In the case shown in fig. 2.7c one stream is kept uniform, so that λ varies from 0 to about 1/3. The example in fig. 2.7d

[2] Here the term "basic flow" specifies that part of a flow which is commonly referred to as free stream, primary stream or outer flow in the literature.

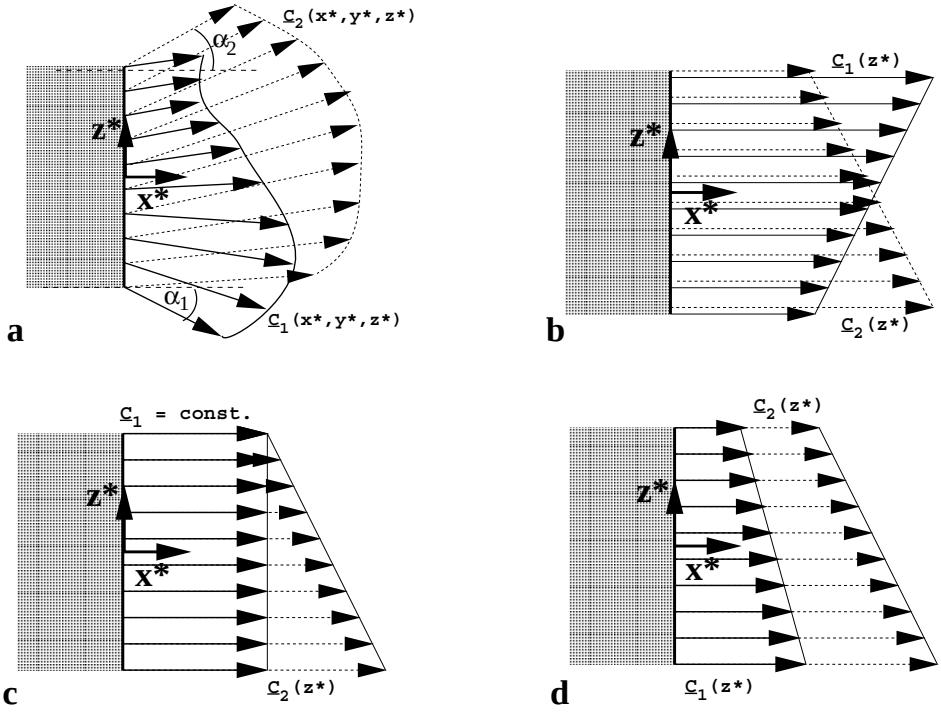

Fig. 2.7: Cases of three-dimensionality of the basic flow; **a** general configuration; **b-d** special cases of increasing simplicity.

shows a configuration where λ is constant over the span while the convection velocity decreases linearily in *z*-direction.

Although confined to parallel velocity vectors and linear velocity distribution in *z*, these examples of *three-dimensional basic flows* represent interesting cases for studies of "weak" three-dimensionality in shear layers. To the authors knowledge no flow cases of this kind have been reported so far.

Condition II: Three-dimensionality of the basic geometry or flow refers to all three-dimensionalities of stationary boundary conditions of or in the test-section. A slanted or corrugated trailing edge or non-parallel test-section side-walls (Paschereit [6]) are obvious examples for a three-dimensional geometry where the basic flow upstream is, however, two-dimensional. Here we have introduced swirl to an axisymmetric coxial shear layer and thus changed the direction of the convection velocity $\underline{C}_{con}$. Fig. 2.8 juxtaposes four specific cases: The *non-parallel oblique shear layer* is formed by two streams with velocity vectors $\underline{C}_1$ and $\underline{C}_2$, flow angles α_1 and α_2, convection velocity $\underline{C}_{con} = (\underline{C}_1 + \underline{C}_2)/2$ and mean vorticity vector $\underline{\omega}$ (fig. 2.8a). This flow is asymmetric. The classical plane, or two-dimensional shear layer is obtained when $|\underline{C}_1| \neq |\underline{C}_2|$ and $\alpha_1 = \alpha_2 = 0$ (fig. 2.8b). The conditions $\alpha_1 = -\alpha_2$ and $|\underline{C}_1| = |\underline{C}_2|$ describe the case of the *symmetric oblique shear layer*[2] (fig. 2.8c). Another interesting case is the *shear layer between parallel oblique streams*[3] (fig. 2.8d) when $\alpha_1 = \alpha_2$, $|\underline{C}_1| \neq |\underline{C}_2|$. Obviously, cases *a* and *d* are asymmetric, while *b* and *c* are of symmetric quality, a distinction found to be of considerable relevance regarding the formation and strength of coherent structures as was shown by Gründel and Spieweg whose results were presented above.

In this work the shear flows investigated satisfy condition II and correspond to the cases *a*, *b* and *d* in fig. 2.8.

In section 3.1 a description is given on how these shear flows cases are realized. Case *c* is studied currently by Béharelle [7] from the partner group in Poitiers. In a plane configuration Gründel [8] also carried out investigations on this case.

Condition III: Secondary three-dimensionality by structural development occurs naturally as a consequence of the instability of two-dimensional primary structures, such as the rollers in a plane shear layer, which lead to

[2] In the literature this flow is also referred to as skewed or grazing shear layer

[3] Sometimes sometimes referred to as shear layer past a slanted trailing edge

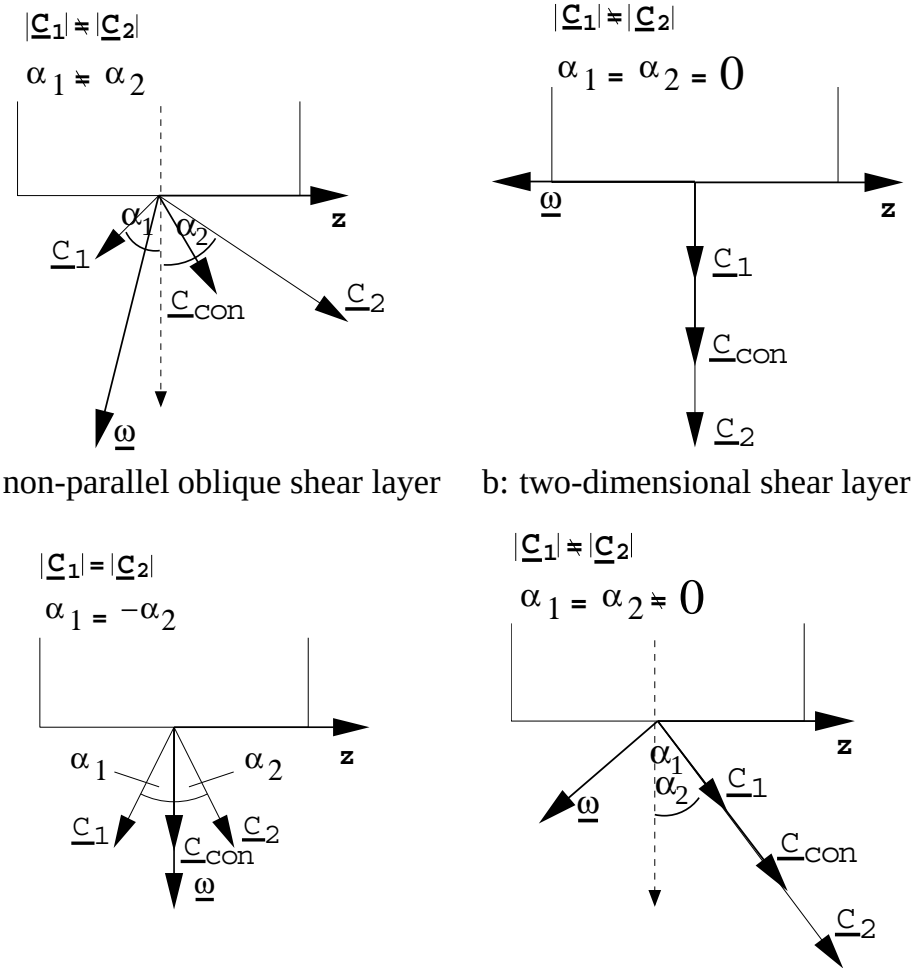

a: non-parallel oblique shear layer

b: two-dimensional shear layer

c: symmetric oblique shear layer

d: shear layer between parallel oblique streams

Fig. 2.8: Cases of three-dimensionality of the basic geometry.

the formation of longitudinal streaks. Controlled intensification of structural three-dimensionality is possible by excitation with either phase- or amplitude variation along the third dimension (Fiedler [9]).

2.3 Research objectives

A classification was presented to describe three basic mechanisms or conditions which lead to three-dimensionality in shear layers. In this work we intend to study the effect of condition II on axisymmetric shear layers. Condition II is realized by two different configurations corresponding to case a, b and d in fig. 2.8 with the help of a particularly designed experimental set-up. Based on the description of the background of the present investigation in section2.1 the research objectives can be summarized by the following points:

1. Design, construction and evaluation of an experimental set-up suitable for the generation of the desired flow configurations
2. Evaluation of the feasibility of the axisymmetric configuration to reproduce results valid also for plane configurations (e.g. the non-existence of mean streamwise vorticity in the free streams; competition between Kelvin-Helmholtz and centrifugal instability)
3. Evaluation of the effect of condition II on the mean turbulent properties (e.g. shear enhancement, spread)
4. Evaluation of the effect of condition II on the primary flow structure (e.g. vortex rings, streamwise vortices, helices)

2.4 Parameters, definitions and equations

In this section parameters characterizing shear layers are presented. A shear layer is the region between two adjacent streams differing in at least one quantity. We will treat only the case in which the velocity vector differs in magnitude or direction. In the classical two-dimensional case the most important parameter is the velocity difference $\Delta\overline{U} = \overline{U}_0 - \overline{U}_1$ which is the driving force for the shear generation. The sketch in fig. 2.9 illustrates how two streams of different velocities $\overline{U}_0$ and $\overline{U}_1$ form a shear layer which grows

with downstream distance x. The free stream velocity values remain constant in axial direction and their streamlines are parallel. Isotachs are commonly used to describe the shear layer growth ([10, 11]). In this work the isotachs used are defined by $(\overline{U}-\overline{U}_1)/(\overline{U}_0-\overline{U}_1)$=0.05, 0.5 and 0.95 also written as $y_{0.05}$, $y_{0.5}$ and $y_{0.95}$, respectively. These lines represent the low speed side boundary, the centerline and the high speed side boundary, respectively, of the shear layer. The position x_0 represents the virtuell origin and depends on the initial conditions such as the turbulence intensity of the free streams or of the boundary layer regime [12].

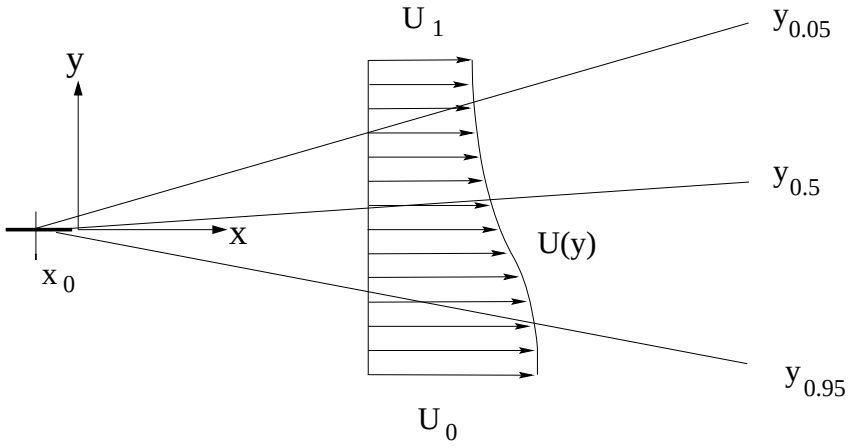

Fig. 2.9: Definition sketch of a two-dimensional shear layer

For the discussion and comparison of shear layers an indispensable property is a measure of the width normal to the mean free stream velocity. Commonly three definitions are used:

geometric width:

$$b(x) = y_{0.05}(x) - y_{0.95}(x) \tag{2.1}$$

momentum loss:

$$\Theta(x) = \int_{-\infty}^{\infty} \frac{\overline{U}(x,y)-\overline{U}_1}{\overline{U}_0-\overline{U}_1}\left(\frac{\overline{U}(x,y)-\overline{U}_1}{\overline{U}_0-\overline{U}_1}\right) dy \tag{2.2}$$

vorticity thickness:

$$\delta_\omega(x) = \Delta\overline{U}/\frac{\partial\overline{U}(x,y)}{\partial y}\Big|_{max}$$

(2.3)

The first, the geometric width b, is defined by the distance between the two isotachs $y_{0.05}(x)$ and $y_{0.95}(x)$ for a given axial position. The second is the *momentum loss thickness* Θ. The third is the ratio between the difference of the velocity, i.e. $\Delta\overline{U} = (\overline{U}_0 - \overline{U}_1)$ and the maximum velocity gradient. It is called the *vorticity thickness* δ_ω. A fully developed turbulent shear layer has a linear growth and shows self-similar behavior which means that when normalized with a characteristic length (e.g. any of the shear layer widths) and a characteristic velocity (e.g. $\Delta\overline{U}$) the profiles of the mean flow quantities at different axial positions collapse on to each other. In the literature (e.g. Browand [13]) the ratio between the vorticity and momentum thickness is given as $\delta_\omega/\Theta \approx 5$.

For the classical planar configuration of a shear layer Abramovich [14] and Sabin [15] defined the spread parameter

$$\lambda = \frac{U_0 - U_1}{U_0 + U_1} \tag{2.4}$$

which enables a universal scaling of plane shear layers with arbitrary velocity ratios such that $db/dx \propto \lambda$, where b is the aforementioned width.

For the three-dimensional case an extension of the shear layer parameter λ was suggested by Fiedler and used by Gründel [1]:

$$\lambda_v = \frac{|\underline{C}_0 - \underline{C}_1|}{|\underline{C}_0 + \underline{C}_1|} \tag{2.5}$$

where the magnitudes and directions of the velocity vectors are taken into account. λ_v describes the ratio between the diffusive $\Delta\underline{C}_{0,1}$ and the convective $\underline{C}_{con}$ ($\propto \Sigma\underline{C}_{0,1}$) components of the free stream velocities. Fig. 2.10 juxtaposes the plane and a three-dimensional case, where in case (*b*) for equal velocities the flow parameter λ_v is larger and consequently the spread must also be larger.

According to Brown & Roshko [10] a spreading constant for all velocity ratios in plane shear layers can be determined as

$$k = \frac{\delta_\omega}{x - x_0}\lambda \tag{2.6}$$

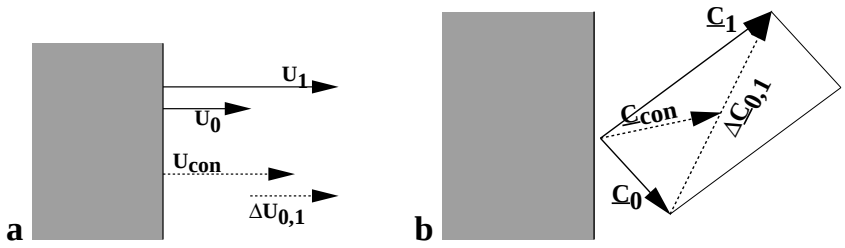

Fig. 2.10: Diffusive and convective components in a plane (**a**) and a three-dimensional shear layer (**b**).

In addition to the classical shear layer normalization a different one is used to take into account the effects of streamline curvature and of additional cross-shear of the free streams. The investigated shear layer with cross-shear, i.e. the asymmetric oblique shear layer (see fig.2.8a), consists of two shear layers perpendicular to each other (fig.2.11). The first one is directed in the $x-y$-plane with a velocity gradient $\partial\overline{U}/\partial y$ and the second one in the $y-z$-plane with a velocity gradient $\partial\overline{W}/\partial y$. As the second shear layer is a curved flow (the y-Koordinate is in fact the radius r) , the angular momentum and not the velocity remains constant along a streamline in the potential flow. Therefore, a modified velocity difference - and thereby momentum difference - defined by

$$\Delta\overline{W}^{\star} = \overline{W}_0\, r_0 - \overline{W}_1\, r_1 \tag{2.7}$$

with $r = R + y$ should be used instead of $\Delta\overline{U}$ as proposed by Plesniak et. al. [16]. It is also convenient to define a new representation of the centerline such that $y^{\star}_{0.5}$ is the position at which the angular momentum corresponds to 50% of $\Delta\overline{W}^{\star}$.

In the introductory part we have mentioned that in plane shear layers coherent structures are generated parallel to the trailing edge. While convected downstream their spacing and diameter increases proportional to the shear layer width. As a consequence, dominating frequencies f_d can be found embedded in measured velocity signals. A commonly used expression describing the relation between f_d, the convection velocity U_c and the shear layer width δ_ω is the Strouhal number:

$$St_{\delta_\omega} = \frac{f_d\ \delta_\omega}{\overline{U}_c} \tag{2.8}$$

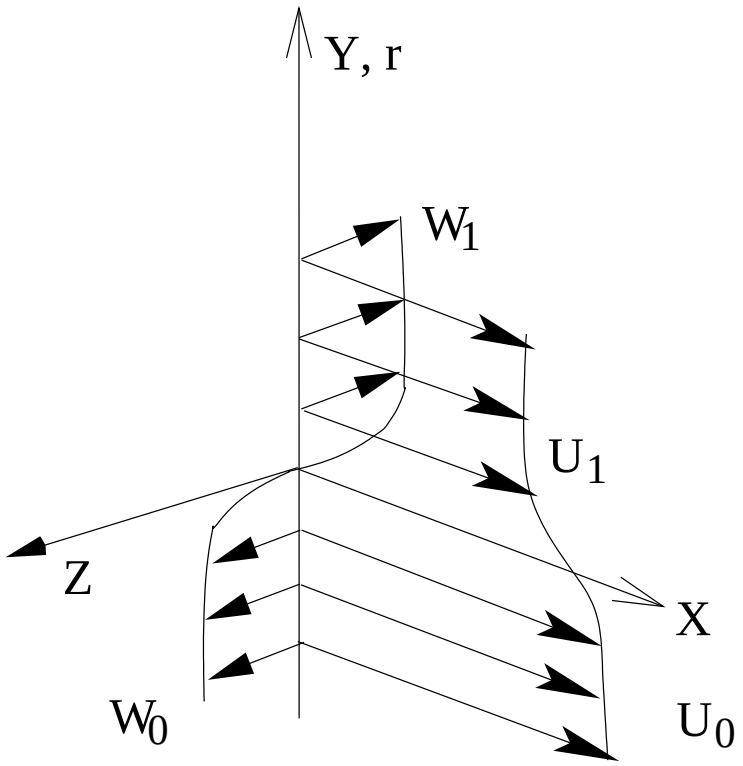

Fig. 2.11: Two shear layers: The first one is directed in the $x-y$-plane with a velocity gradient $\partial\overline{U}/\partial y$ and the second one in the $y-z$-plane with a velocity gradient $\partial\overline{W}/\partial y$.

In this case the convection velocity is $U_c = (\overline{U}_1 + \overline{U}_0)/2$ which has been successfully used for the Taylor-hypothesis. In the literature on plane shear layers St_{δ_ω} is found to be in the neighborhood of 0.3.

Reynolds stress transport equations

To provide a basis for the analysis of the dynamics of the Reynolds stresses their transport equations are given in eqns. 2.9-2.14 in cylindrical coordinates (from R.D. Mehta et al.[17]). They were obtained by applying the thin layer approximation $\frac{\partial}{\partial r} \gg \frac{\partial}{\partial x}$ and by setting terms containing $\frac{\partial}{\partial \varphi}$ to zero because of axisymmetry. Diffusive, convectiv and dissipative terms are also neglected. The terms containing the extra strain $\overline{W}/r$ are not true productions terms, but represent the effects of rotation of the coordinate axis [18].

$$\partial\overline{u'^2}/\partial t \approx -\overline{u'v'}\ \frac{\partial\overline{U}}{\partial r} \tag{2.9}$$

$$\partial\overline{v'^2}/\partial t \approx 2\ \overline{v'w'}\ \frac{\overline{W}}{r} \tag{2.10}$$

$$\partial\overline{w'^2}/\partial t \approx -\overline{v'w'}\ \frac{\partial\overline{W}}{\partial r} - \overline{v'w'}\ \frac{\overline{W}}{r} \tag{2.11}$$

$$-\partial\overline{u'v'}/\partial t \approx \overline{v'^2}\ \frac{\partial\overline{U}}{\partial r} - \overline{u'w'}\ \frac{\overline{W}}{r} \tag{2.12}$$

$$-\partial\overline{u'w'}/\partial t \approx \overline{u'v'}\ \frac{\overline{W}}{r} - \overline{v'w'}\ \frac{\partial\overline{U}}{\partial r} \tag{2.13}$$

$$-\partial\overline{v'w'}/\partial t \approx (\overline{v'^2} - 2\overline{w'^2})\ \frac{\overline{W}}{r} + \overline{v'^2}\frac{\partial\overline{W}}{\partial r} \tag{2.14}$$

2.5 Bibliographic Review

Investigations with the focus on the structural evolution of mixing layers under the influence of three-dimensional boundary conditions (condition II as described in section 2.2) are scarce. Although many investigations considered swirling jets which satisfy condition II, they focused only on the description of the mean behavior and provide no information on the structural behaviour.

Plane configurations and then some axisymmetric configurations including swirling jets are presented. For completion some major results from studies on classical plane shear layer are presented first.

Plane shear layers and the role of coherent structures

Plane shear layers have been the object of intense research over the last decades as they are the simplest practical flow capturing the essential features of free turbulent shear flows while being somewhat of a hybrid between jet and wake.

The concept of three-dimensional structures - assumed to be a general characteristic of turbulence - was to some extent first modified by observations of Brown & Roshko [10] in a plane shear layer, who found the flow to be dominated by quasi two-dimensional ”coherent” structures (rolls), which are distorted by longitudinal structures (streaks) to form three-dimensional coherent scenarios. A numerical simulation by Silvestrini [19] shows clearly the rolls and the streaks.

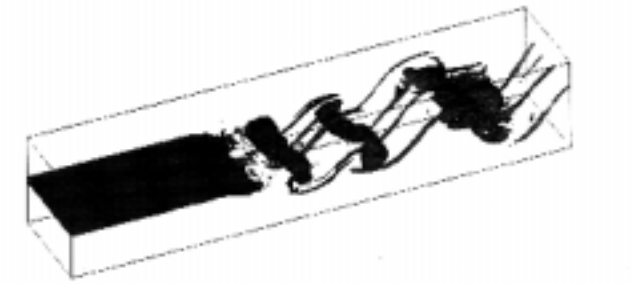

Fig. 2.12: Numerical simulation of a plane shear layer showing rolls and streaks (from [19])

There is no unique definition of coherent structures, Fiedler[20] provides a global description: ”the transient yet repetitive manifestation (in concentrated vorticity) of an instability mode”. Coherent structure are responsible for flow-noise, affect chemical engineering processes, influence mixing, combustion, drag and lift of aircrafts. They can be - on the other hand - influenced by outside conditions thus representing a principle ”vehicle” to control turbulent flows. Flow stability is responsible for their origin and their decay (by creation of smaller structures as a consequence of their instability). For

more detailed discussions of coherent structures and the aspect of their control the reader is referred to the following literature [21, 22, 23, 20, 4, 24].

Bernal & Roshko [25] developed a model for the flow structure of plane shear layers where counter-rotating vortices are part of a vortex system winding back and forth between the high-speed side of a primary vortex and the low-speed side of the following one (Fig. 2.13). The pairs of counter-rotating vortices move up and down across the braids and appear as mushroom-shaped structures in visualized cross-sections. The streamwise vortices and the ensuing three-dimensionality of the fluctuating large scale motion enhances the mixing processes. Some workers attempted to force these secondary structures by various means: Corcos and Lin [26] applied spanwise perturbations in a numerical approach, Lasheras and Choi [27] used corrugated splitter plates and Nygaard and Glezer [28] employed strip heaters.

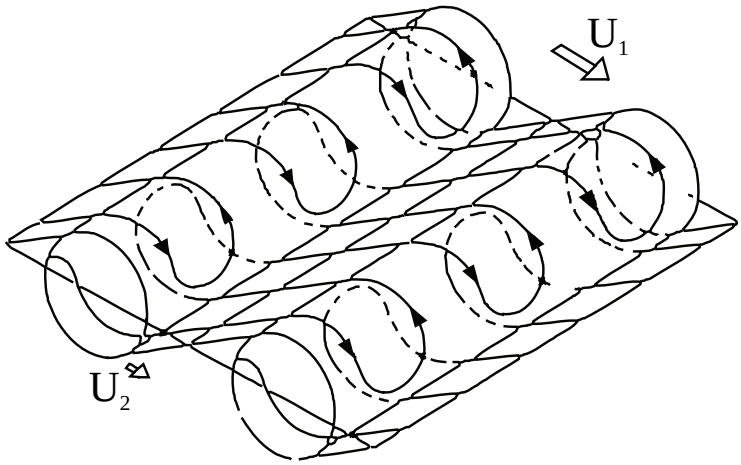

Fig. 2.13: Principle sketch of vortex structures in plane shear layers (from [25])

Plane three-dimensional mixing layers

The first investigation of a three-dimensional mixing layer in a plane configuration was performed by Hackett & Cox [29] who studied the mixing layer between two streams skewed at 90°. The axial velocity components were of the same magnitude. This configuration was similar to that investigated by Gründel [30] with the latter having a skewing angle of 30°. Both belong to case **c** of fig. 2.8 (condition II: three-dimensionality of the basic geometry).

The experimental investigation of a forced mixing layer past an oblique trailing edge by Kibens et al.[31] showed that large coherent structures oriented either parallel to the trailing edge or normal to the flow direction, depending on the forcing frequency.

In a numerical investigation of a similar configuration Fiedler et al. [5] observed diamond shaped patterns formed by individual vortices which retain on the average their orientation normal to the mean flow direction while being partly bulged out in the upstream and downstream direction. From a top view these deformations create the impression of diamond shaped patterns.

In a temporally developing shear layer with cross-shear generated in a stratified tilting tank P. Atsavapranee [32] observed co-rotating streamwise vortices and enhanced mixing.

Axisymmetric three-dimensional shear layers

Swirling jets - representing the axisymmetric counterpart of the above shear layers were - were already studied in the early sixties and numerous investigations have followed since then motivated by the application of swirl in many engineering devices such as industrial burners or cyclonic separators. Swirl is an undesired feature of aircraft wake flows. In nature swirling motion is observed in the ocean and in the atmosphere (tornados). Many of its applications involve a zone of reverse flow (“recirculation bubble”) which is used to increase flame stability and combustion intensity. The onset of flow reversal is related to the phenomenon of *vortex breakdown*. In other words if one considers a swirling jet as a columnar vortex, then the appearance of longitudinal recirculation can be interpreted as vortex breakdown. When recirculation occurs various flow field structures can evolve such as a central recirculation zone , a torodial recirculation zone (”donut shape”) or a long reverse-flow region or columnar flow. The initial velocity profile has a significant influence on swirling flows and, most likely, on the shape of the recirculation zone. In swirling shear layers Kelvin-Helmholtz and centrifugal (Rayleigh) instabilities act on the flow.

The swirl number S is an important parameter to characterize swirling jets. Here it is a non-dimensional integral measure to denote the degree of flow rotation and is defined by the ratio of axial flux of angular momentum G_φ to the axial momentum G_x:

$$S = \frac{G_\varphi}{G_x} = \frac{2\pi\rho \int_0^\infty r^2 \overline{U}\,\overline{W}\,dr}{R2\pi \int_0^\infty (\rho\overline{U}^2 + \Delta p) r\,dr} \tag{2.15}$$

R is the radius of the jet.

There exist different definitions of the swirl number which make it rather difficult to compare results of different authors. However, as an integral measure it does not give information on the shape of the underlying velocity profiles which have a significant influence on the flow evolution. For this reason the swirl number does not play an important role in the present work although swirling jets are used. A discussion on the definition of the swirl number is given in [33].

Samet and Einav [34] studied a swirling jet in a co-flowing uniform stream with a 5-hole pressure probe. S=0 ,0.12, 0.31, 0.40 and 0.49. Velocity ratios between inner and outer flow 0, 0.08, 0.02 and 0.3. X/D=4 to 15. They observed that by increasing the swirling motion of the central flow the influence of the co-flowing flow can be diminished and vice versa.

R.D. Mehta et al. [17] investigated the effects of swirl on a turbulent axisymmetric mixing layer with a tripped initial boundary layer. The swirl generator was a rotating honeycomb. Measurements were obtained in the near-field between X/R=0.2 to 4.2 . Three swirl numbers were studied: S_W= 0, 0.2, and 0.4, where $S_W = \overline{W}_{max}/U_0$. These correspond to S_W=0, 0.1, and 0.2 for the above swirl number $S = G_\varphi/G_x$. The one point measurements were done with an X probe for the turbulence measurements and a slanted-wire probe for the $\overline{U}$ and $\overline{W}$ measurements using a modified X probe. With increased swirl intensity the Reynolds stress levels and the shear layer thickness increased. At S_W=0.4 $\overline{u'v'}$ grew by 50% compared to the zero swirl case and the secondary stresses $\overline{v'w'}$ and $\overline{u'w'}$ reached about 30% of the primary stress values. At S_W=0 and S_W=0.2 the growth rate was almost equal at about $d\delta/dX$=0.72 and 0.71 whereas for S=0.4 it was 0.099. The stress increase is partly explained by extra production activated by the presence of the swirl. These terms are further increased when angular momentum instability occurs ($\partial\overline{W}/\partial r < 0$).

Control and stability of swirling jets

Taghavi et al. [35] were the first to investigate the excitability of a swirling jet with S= 0.l2 by plane acoustic waves varying the Strouhal numbers St =

fD/U. It was found that the jet was excitable with a "preferred" Strouhal number of St=0.39 . The maximum amplitude used was 6.8 % of the time-mean axial velocity $\overline{U}$. This resulted in increased jet spread and mixing.

Panda & McLaughlin [36] performed experiments of instabilities of a swirling jet with vortex break down. Axisymmetric and helical instability waves were acoustically excited. Instability waves grew less compared to the non-swirling case. Pairing was suppressed.

Martin & Meiburg [37] demonstrated by a linear stability analysis of a swirling jet shear layer that the centrifugally stable flow case becomes destabilized by sufficiently short Kelvin-Helmholtz waves. In the centrifugally unstable case disturbances with positive azimuthal wave number have a greater growth rate than their negative counterparts, due to their alignment with the helical vortex lines. Also centrifugal instability dominates in the case of long axisymmetric waves while for long helical waves Kelvin-Helmholtz instability dominates.

Trailing vortex

Singh and Uberoi [38] studied an isolated trailing vortex of a laminar flow wing at a sectional lift-to-drag ratio of 60. They found that the vortex has a turbulent core and an axial jet in the near-field of the wing (down to z/c=2.4 ; c=chord) as opposed to cases with a lift-to-drag ratio of 20 where axial velocity defects occur. The axial jet is rapidly dissipated and a wake defect develops in the core (z/c=5). At the same time swirl velocity profiles showed that the initially concentrated vortex core is rapidly expanded outwards. Two unstable modes, m=0 and $|m|$=1, were found to exist with the helical mode being more energetic. The authors claim that the observed instabilities are those associated with large axial velocity difference between the core and potential part of the vortex. Later in the present investigation we will report a similar flow situation generated by a swirling jet.

3. Experimental set-up

3.1 The wind tunnel

The design and construction of a wind tunnel capable of generating shear layer configurations according to condition II described in the introduction was a major task of the present work. In the preceding work by Gründel [1] plane shear layers corresponding to the symmetric oblique shear layer and to the shear layer between parallel oblique streams were analyzed experimentally and numerically. Gründel remarked that his results might have been influenced by the side walls which were present in the set-up in the plane shear layer. Further, his axisymmetric configuration did not work satisfactory as well (see section 2.1). Therefore a new axisymmetric solution with coaxial swirling jets was designed for the present study to overcome the problems encountered in his configurations.

This solution allows to create three different flow configurations satisfying condition II: The asymmetric oblique shear layer (Fig. 2.8a), the symmetric oblique shear layer (Fig. 2.8c) and the shear layer between parallel oblique streams (Fig. 2.8d). Two identical facilities were built with the intention to establish a basis for a collaborative research project concerning several issues and configurations of three-dimensional shear flows. The facilities are located in the Centre d'Études Aérodynamiques et Thermiques (CEAT) in Poitiers (France) and in the Hermann-Föttinger Institute (HFI) in Berlin.

This chapter describes considerations which lead to the realized configuration: An open-circuit wind tunnel (Fig. 3.1, 3.2, 3.3, 3.4, 3.5) consisting of two coaxial plenum chambers with attached swirl generators and coaxial contractions. Each swirl generator consists of 36 adjustible radial inlet vanes allowing the generation of three different basic swirl combinations, non swirling, co-swirling and counter-swirling jets. Each swirl generator is

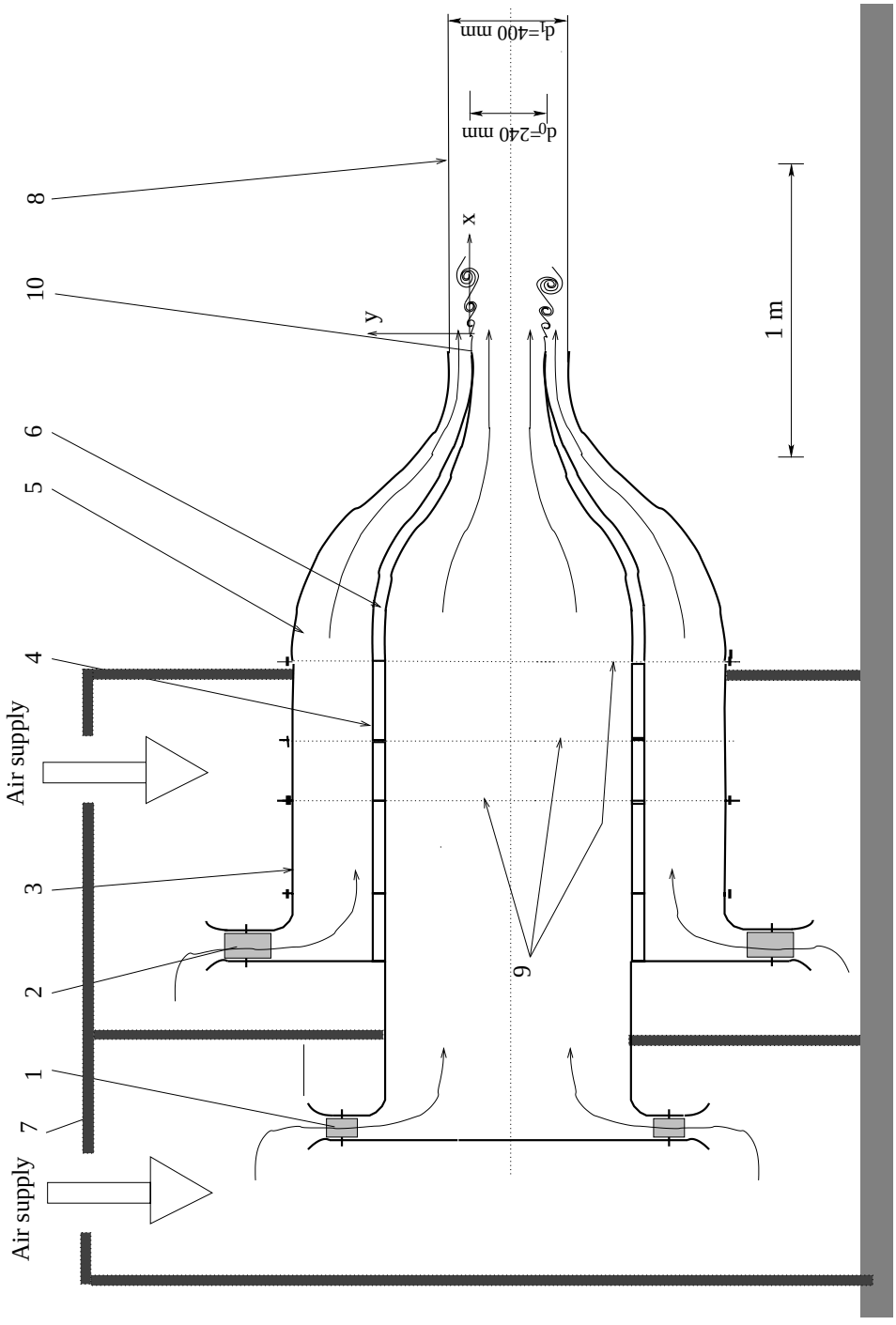

Fig. 3.1: The wind tunnel: 1, 2 radial inlet with vanes; 3 annular plenum chamber; 4 central plenum chamber; 5, 6 contractions; 7 cabin; 8 test section; 9 screens; 10 axisymmetric trailing edge and coordinate system

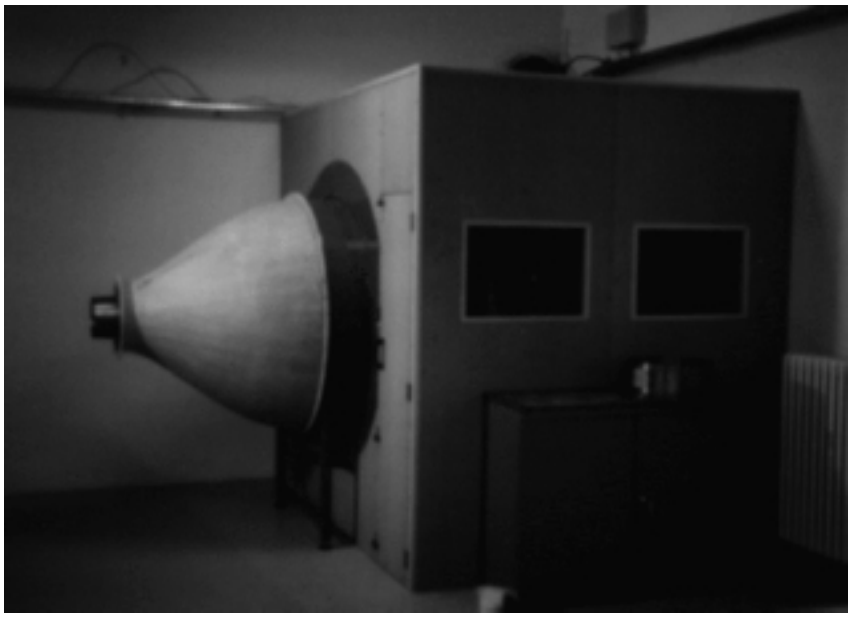

Fig. 3.2: The wind tunnel without test section (photo taken in Poitiers)

enclosed in a separate cabin. These are supplied with air by means of two independent centrifugal blowers. In the appendix a sketch of the wind tunnel including the major dimensions and the arrangement of the adjustible vanes is shown in section 6.1.

In order to obtain results in the axisymmetric configurations representative also of a plane configuration, the ratio between the shear layer momentum thickness and the diameter of the axisymmetric splitter plate (i.e. the nozzle wall of the central jet) needs to be small, i.e.:

$$\frac{b}{R} << 1. \tag{3.1}$$

Then the near-field shear layer dynamics behave essentially as a plane shear layer [39]. The initial shear layer momentum thickness is given by the thickness of the two boundary layers originating from the splitter plate. To obtain thin boundary layer momentum loss thicknesses the Reynolds numbers of the jets must be high. The inner nozzle diameter should also be as large as possible. With this in mind and taking also practical and economical aspects into account an inner nozzle diameter of d_i=240 mm, an outer nozzle diameter of d_o=400 mm and a maximum free stream velocity of U=30 m/s (for either stream) were chosen. Another important aspect with regard to the

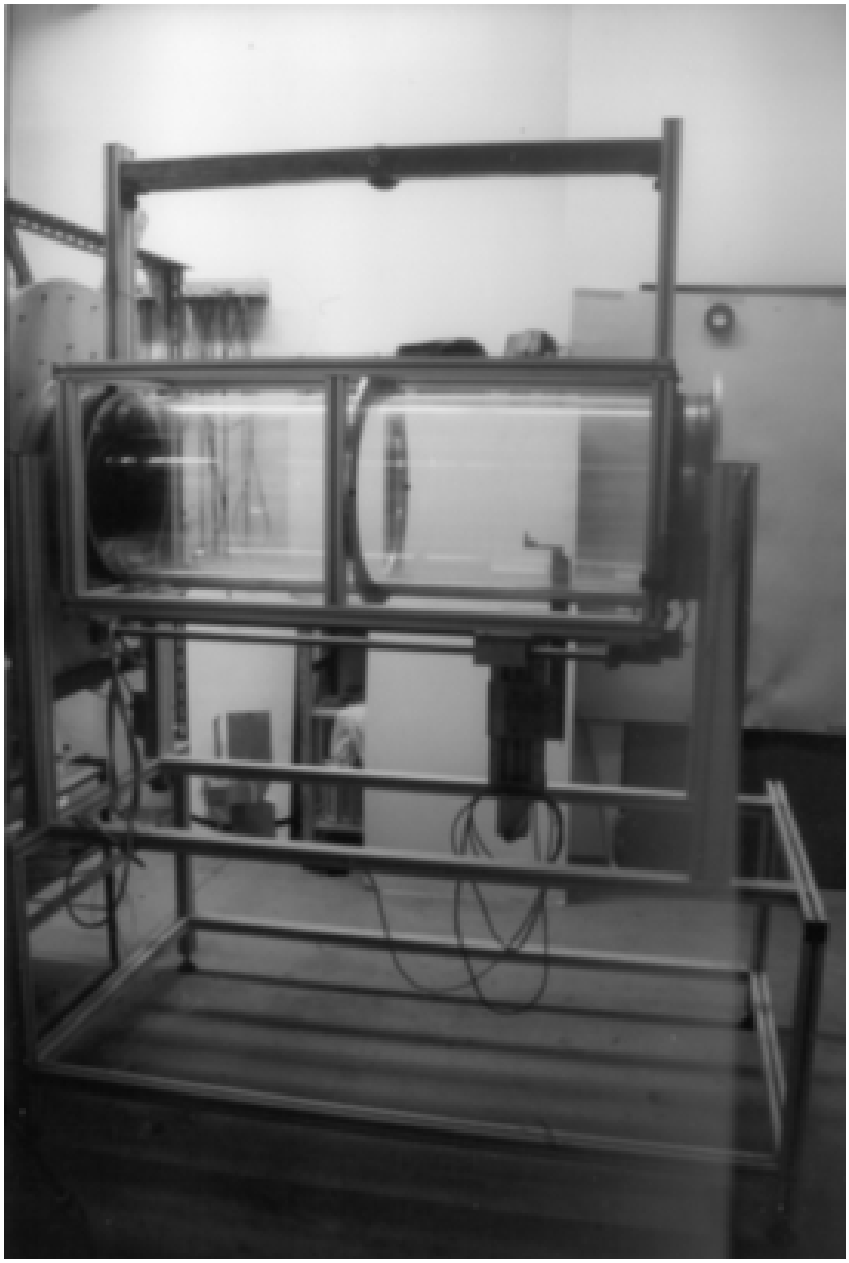

Fig. 3.3: The test section with the traversing mechanism (photo taken in Berlin)

Fig. 3.4: The coaxial plenum chambers consist of four cylindrical segments allowing to span the screens (not shown) across the total cross-section (photo taken in Poitiers)

Fig. 3.5: The central jet exit (”milk bottle”) , the contration of the outer jet is dismanteled (photo taken in Poitiers)

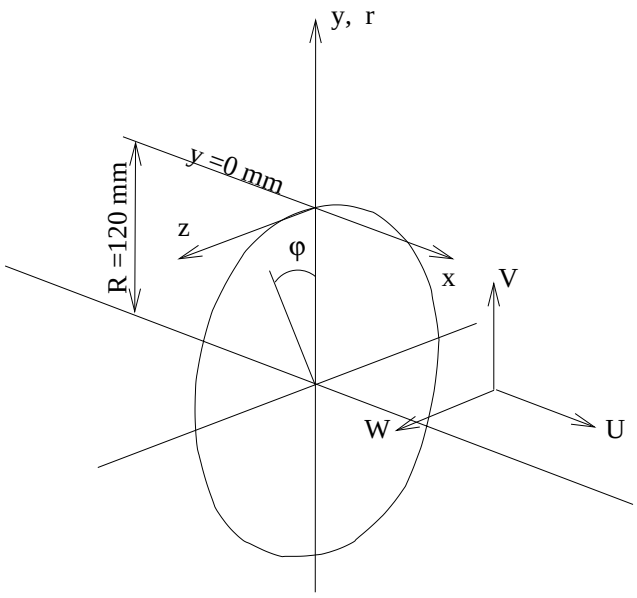

Fig. 3.6: Axisymmetric trailing edge and coordinate system

comparability to plane configurations is the existence of mean streamwise vorticity in the free streams. In a plane configuration no such vorticity is present. This issue will be addressed below.

A low free-stream turbulence level and low mean flow non-uniformities are important aims in wind tunnel design and are generally achieved by the use of honeycombs, screens and contractions [40, 41]. However, the concept of this wind tunnel necessitated a swirl generator to introduce the tangential velocity component. This lead, depending on the type of the swirl generator used, inevitably to non-uniformities, e.g. wakes of swirl vanes or discrete tangential jets preserving their identities far downstream [42]. Therefore, it was decided to position the swirl generator far upstream of the test-section entry and upstream of the turbulence reducing devices.

A model wind tunnel with a single swirling jet was constructed to investigate the effects of screens as turbulence reducing devices. The model consists of a swirl generator, a cylindrical plenum chamber and a contraction. Its overall length is about 60 cm. Experiments on the single swirling jet generated in the model wind tunnel indicated that screens significantly reduced turbulence intensities even in swirling flows but at the same time had a strong influence on the shape of the mean velocity profile. In experiments without screens the velocity profile at the jet exit showed a central trough for the axial mean

velocity and high tangential velocities near the jet perimeter (Fig. 3.8). When a screen was applied the central trough in the axial velocity profile became a hump and the maximum tangential velocity near the jet perimeter was shifted towards the center as for a potential vortex profile. An explanation for this change in profile shape might be the following: As the flow was generated by two tangential inlets (Fig. 3.7) upstream of the screen, the greatest tangential velocities are found not in the center of the jet but at its edge. This velocity distribution persists also at the jet exit when no screen is applied. In the case with a screen the periphal tangential flow suffers a strong deflection through the screen forcing the flow towards the center. This results in the above mentioned axial and tangential velocity peaks in the jet center.

Three screens with successively decreasing mesh sizes (meshsizes= 5; 2; 1.15 mm and wirediameters= 1.0; 0.71; 0.45 mm) were installed in the plenum chambers. To avoid any flow perturbation by mounting devices within the plenum chambers, the screens were stretched over both plenum chambers which are made of cylindrical segments (see fig. 3.4).

For a further reduction of the turbulence and the boundary layer thickness a contraction was used. The inner stream contraction had a ratio of 9.8:1 and the annular stream a contraction of 12:1. The contraction contours were designed such that both flows were continually subjected to a favorable pressure gradient. They resulted from matching two cubic arcs. It was believed that the tendency of separation of the annular flow from it's inner walls is higher at the first arc than at the second because unfavorable streamwise curvature and centrifugal forces act on the flow at the same time. To reduce this effect it was decided to use a larger radius for the first arc than for the second. Consequently the matching point for the two arcs was chosen at $0.7L$ (L, contraction length) resulting in a larger radius for the first. The increased danger for the formation of Görtler vortices at the second arc is expected to be compensated by the swirling motion. This was indicated in a study of the Görtler instability under the influence of crossflow [43]. Still, suction of the boundary layers immediately downstream of the contraction was possible through a cylindrical gap. However, this was not applied in the current work. The nozzle-walls were made of fiberglass and mounted together to form a single hollow contraction-cone. At its downstream end 36 holes terminate the cavity in the cone.

The axisymmetric trailing edge is made of a metal cylinder of 150 mm length and 10 mm wall thickness. The downstream edge is tapered to a knife-edge with a minimum thickness of 0.3 mm. It is attached to the contraction-cone

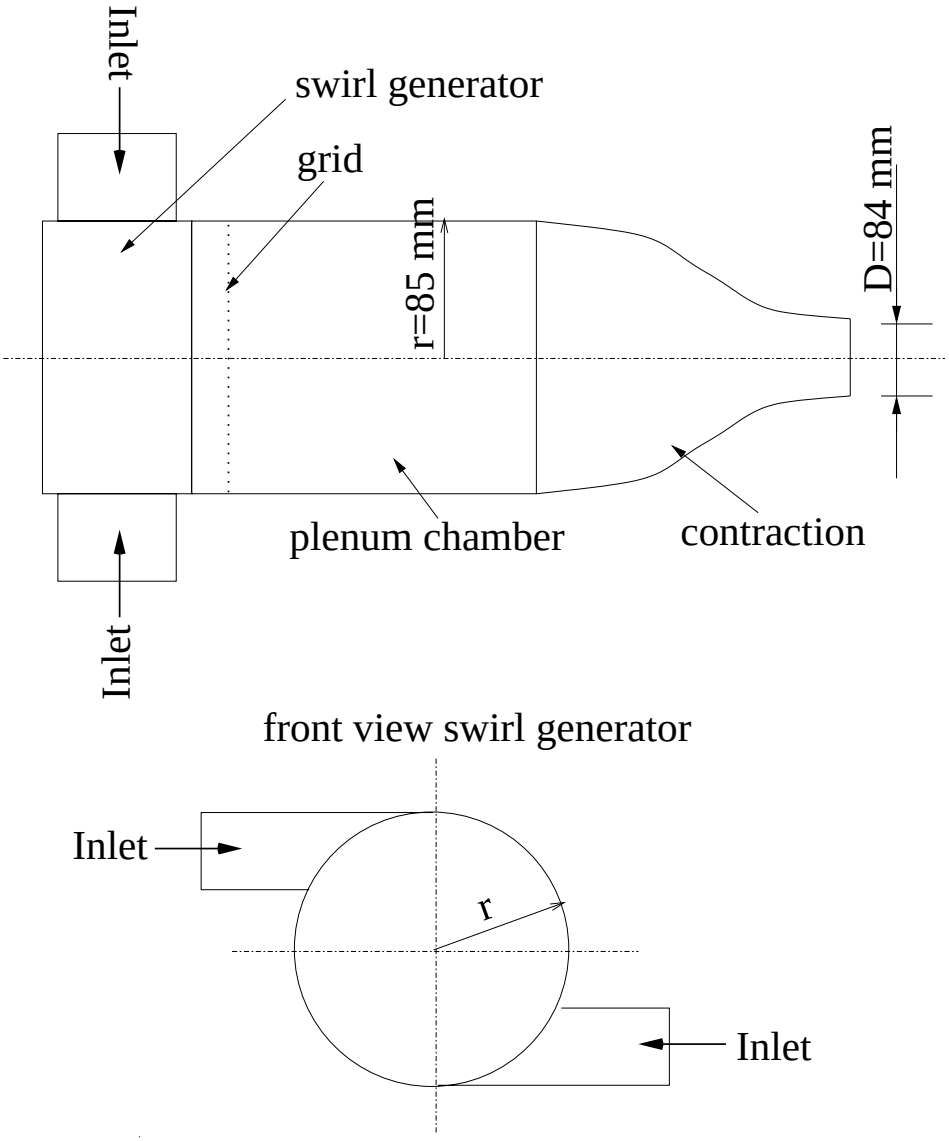

Fig. 3.7: The model wind tunnel (single swirling jet): The swirl generator consists of two tangential inlets

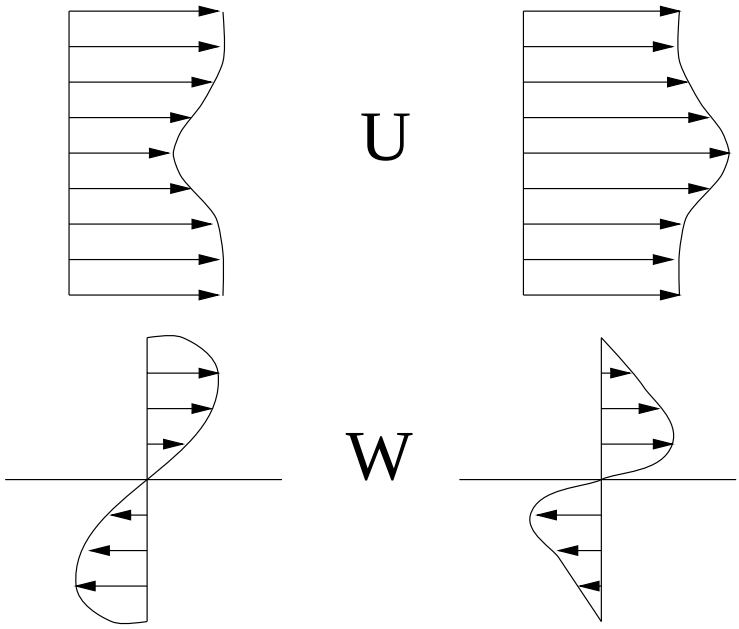

Fig. 3.8: The effect of a screen on the axial and azimuthal velocity profiles. left:no screen; right: with screen

so that, if desired, the aforementioned cylinder gap can be adjusted (see foto in fig. 3.9). It also allows suction or injection of smoke for flow visualizations. Either the inner side or the outer side of the gap can be sealed with tape, what allows to have suction or smoke injection only on one side of the trailing edge.

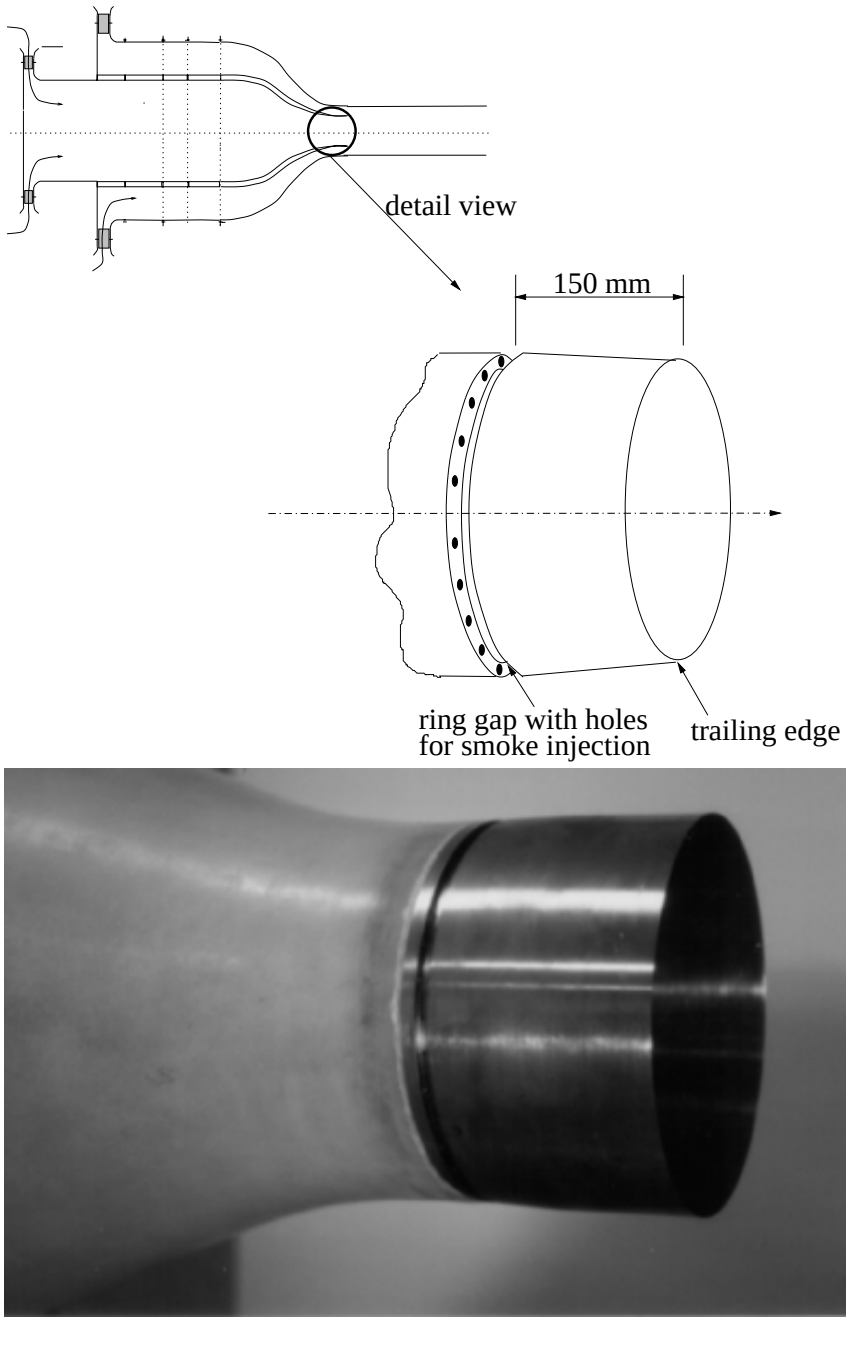

Fig. 3.9: Sketch and foto of the trailing-edge and the ring gap for smoke injection and suction. The width of the gap can be adjusted.

The consideration leading to the swirl generator with adjustable radial inlet vanes, were guided by the following objectives:

- Easy change of swirl direction and continuous variation of its magnitude including the no swirl case.
- A high degree of axisymmetry of the jet exit velocity profiles.

To satisfy these requirements it was decided to use a large number of vanes, i.e. 36, and to arrange them regularly around the circumference of both radial inlets. In the next section experimental results are presented which document the satisfactory flow quality obtained in this way. The vanes were made of rectangular pieces of sheet metal with soldered axles. A mechanism consisting of gears and a transmission cable permits the rotation of all vanes between -80° and +80°. The vane angles of the central and the outer jet are denoted by α_0 and α_1, respectively.

To shield the shear layer from outside disturbances, a cylindrical test-section of 1.5 m length and 400 mm diameter made of a transparent sheet of polycarbonate was used. A PC-controlled traversing mechanism was mounted in the test-section. Hot-wire probes and rakes can be traversed in all three directions x, r and φ.

Coordinate system

In the coordinate system used, the radial direction is denoted by r or by y with y=0 being the trailing edge radius R=120 mm (Fig. 3.6). Negative y-values define radial positions in the central jet while positive values define positions in the annular jet. The y-definition is analogous to those used in plane configurations.

Throughout the work the subscript ”0” denotes properties of the inner jet (except for the virtual origin x_0) while the subscript ”1” denotes those of the annular jet.

3.2 Measurement Techniques

Two techniques of data acquisition were employed: hot-wire and laser Doppler anemometry (LDA). In this chapter we address various aspects of these experimental methods. These include the different hot-wire probes used and their characteristics.

Hot-wire anemometry is the principal technique of data acquisition in this investigation because of its low operational costs and its high frequency response. In particular for multi-point measurements necessary for studies of turbulent structures rakes of with hot-wires were used.

3.3 Hot-wire technique

Depending on the flow information, particular probe types were employed ranging from simple N-wire probes to complex 6-wire probes. Most of them were designed and made in the Hermann-Föttinger Institute (HFI) while the rake with 24 N-wire originated from CEAT (see [44]). The following table gives an overview of the probes with some of their specifications.

The N-wire probes were of standard geometry and do not need any further description. The 4-sensor probes (fig. 3.11) were built by using two orthogonal pairs of X-probes and were used to measure simultaneously the 3 velocity components U , V and W being the axial, radial and azimuthal components, respectively. The distance between two prong planes belonging to the same wire pair is 0.7 mm for both 4-wire probe types used. The wires of

Probe	origin	wire	
		diameter	sensitive length
a) N-wire	HFI	5 μm	1.0 mm
b) N-wire	HFI	2.5 μm	0.5 mm
c) N-wire	CEAT	2.5 μm	0.7 mm
d) 4-wire	HFI	5 μm	1.0 mm
e) mini-4-wire	HFI	2.5 μm	0.5 mm
f) 6-wire	HFI	5 μm	1.0 mm

Tab. 3.1: hot-wire probes

the standard 4-wire probe were arranged so that one wire pair belonging to one X-probe was 2 mm downstream of the other. The mini-4-wire probe had the same arrangement as the ”Kovasnay-probe” [45] but with much smaller dimensions. The 6-wire probe consisted of three pairs of x-wires and was developed by Kim [46] (Fig. 3.10). It was designed to measure the instantaneous vorticity component ω_x and ω_y or ω_z depending on its orientation. However, for this application it would have been necessary to design a mechanism which aligns the probe parallel to the mean flow direction at each radial position. Such a mechanism would have required an extensive modification of the test section which could not be carried out during this investigation. Therefore the 6-wire probe was only used as a 4-wire probe and was calibrated in the same way as the other 4-wire probes. The 6-wire probe was then used only for comparison of the results obtained from all probes. The accuracy of the 6-wire probe was checked in the work by Kim [46]. It should be mentioned that its output was erroneous in the case of wake type flows, i.e. where the two jets have the same axial velocity. This is attributed to the large velocity-gradient which could not resolved spacially by the probe.

Temperature was kept constant within one degree Celsius. Calibrations were made in situ except those for the angular calibration which is described below. A Prandtl-tube provided the reference velocity by measuring the dynamic pressure. As already mentioned, the resolution of the AD-converter is N_b=12 (number of bits). The corresponding voltage range used is $\Delta V = 10V$. Thus the voltage resolution is about 2.5 mV. This quantization effect results in a white noise in the high frequency range of the signal.

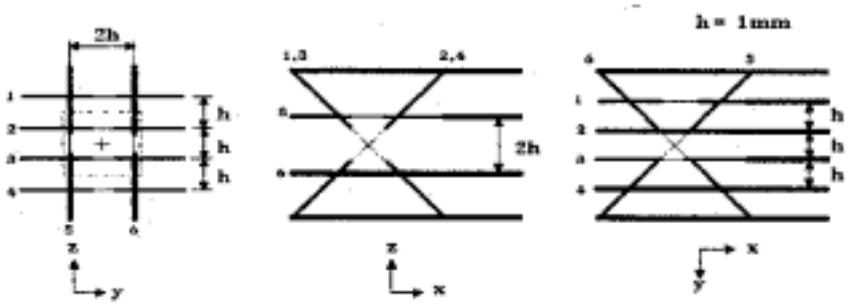

Fig. 3.10: Schematic of the 6-wire-probe by Kim [46]

3.3.1 Calibration of the 4-wire probes

In the following the principle of the angular calibration of the 4-wire probes is presented. It was proposed by Jacquin et al.[47] and is described in detail as the ”4F” method. The principle is based on the assumption that the velocity response is independent of the angular response. This behaviour has been found to exist in cases where the flow angles are smaller than about 45°.

The advantage of this method is that only a simple calibration just as in the case of a N-wire is needed prior to each experiment. The angular calibration is made only once (as long as the probe geometry remains unchanged, e.g. no wire replacement).

The sensor voltages of the HFI probes were measured with AA Lab Systems constant-temperature anemometers with built-in gain/offset and low-pass filter circuitry. The data were sampled by a PC with a 16-channel 12-bit AD-converter. The overheat ratio was 1.7 for the 5 μm wires and 1.5 for the 2.5 μm wires. The calibration equation $U_{eff} = F(E)$ was approximated by polynomes $U_{eff} = Pol_n(E)$ where the effective cooling velocity U_{eff} was assumed to be perpendicular to the wire (cosine law). E is the anemometer output voltage. The order of the polynomes n was 3. This calibration method has shown to have an error less than 1% (Kim [46]) as long as the angle between the velocity vector and the wire normal is less than $|20°|$. In two-dimensional flow situations the axial velocity for an N-wire probe was obtained from $U = U_{eff}$ while for the X-wire probes the velocity components were obtained by $U = (U_{eff_1} + U_{eff_2})/2$ and $V = (U_{eff_1} - U_{eff_2})/2$. During calibration and measurements the ambient temperature was kept constant within 1° Celsius. Calibrations were made in situ except those for the

angular calibration which is described below. A Prandtl-tube provided the reference velocities by measuring the dynamic pressure. As already mentioned, the resolution of the AD-converter is N_b=12 (number of bits). The corresponding voltage range used is $\Delta V = 10V$. Thus the lowest detectable voltage variation is about 2.5 mV. This quantization effect results in a white noise in the high frequency range of the signal.

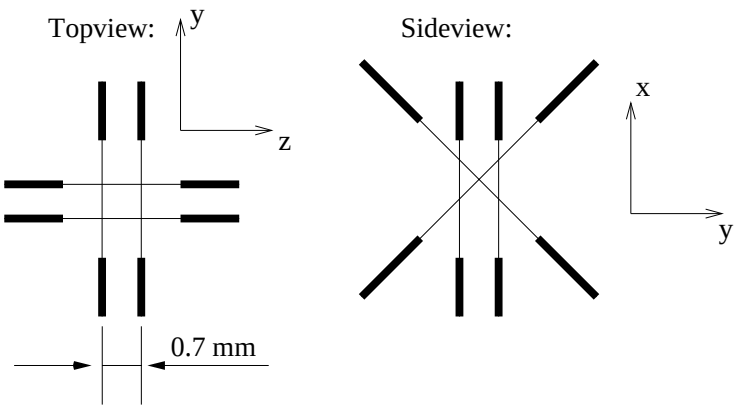

Fig. 3.11: Schematic of the 4-wire-probe

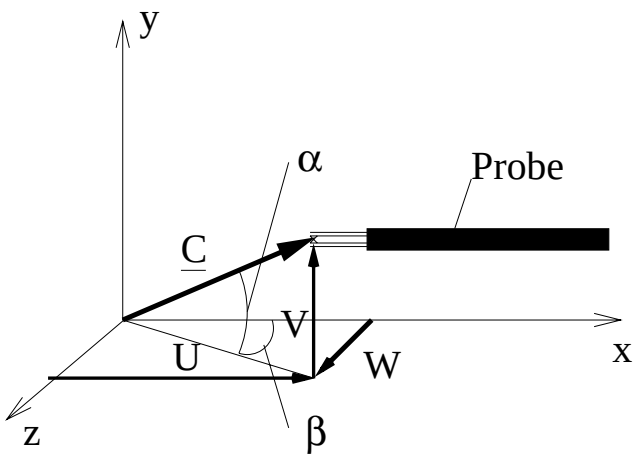

Fig. 3.12: Relations between velocity vector, yaw and pitch angles

$|\underline{C}|$ is the resultant velocity at a given point in the flow field. With the knowledge of C, α and β, the components at that point are defined (Eqns. 3.2 to 3.4) as

$$U = |\underline{C}| \cos\alpha \cos\beta \quad (3.2)$$
$$V = |\underline{C}| \cos\alpha \sin\beta \quad (3.3)$$
$$W = |\underline{C}| \sin\alpha \quad (3.4)$$

The angular calibration is performed in two steps:

1. voltage-velocity calibration
2. angular calibration

From the voltage-velocity calibration, during which the probe axis was parallel to the direction of $|\underline{C}|$, a polynome was obtained expressing the dependence of the output voltage E_i on the velocity $U_i^* = Pol_{ni}(E_i)$ for each wire i of the 4-wire probe.

In the second step the yaw (α) and pitch (β) angles of the 4-wire probe were varied between -25° and 25° in steps of 5° (fig. 3.12). For each of 121 positions mean values for the U_i^*'s were measured. The U_i^*'s do not represent the actual effective velocity $|\underline{C}|$ but a "fictious" effective velocity needed to compute the non-dimensionalized coefficients $K_\alpha(\alpha,\beta)$, $K_\beta(\alpha,\beta)$ and $K_C(\alpha,\beta)$ defined in equations 3.5 to 3.7. These coefficients represent the angular characteristics of the probe and are - within certain limits - which are given below - independent of the velocity. The surfaces formed by K_α and K_β are shown in fig. 3.13 as functions of α and β for the mini-4-wire probe.

$$K_\alpha(\alpha,\beta) = \frac{U_1^{*2} - U_2^{*2}}{U_1^{*2} + U_2^{*2}} \quad (3.5)$$
$$K_\beta(\alpha,\beta) = \frac{U_3^{*2} - U_4^{*2}}{U_3^{*2} + U_4^{*2}} \quad (3.6)$$
$$K_C(\alpha,\beta) = \frac{U_1^{*2} + U_2^{*2} + U_3^{*2} + U_4^{*2}}{|\underline{C}|^2} \quad (3.7)$$

The surfaces of K_α and K_β in fig. 3.13 show a tendency of forming plateaus (i.e. reaching constant values) for angle $> |25|°$. These regions represent the limits of the method beyond which as the angles can not be determined

unambigiously. A quantitative method to determine the limits is to compute the Jacobian-matrix of the functions K_α and K_β at all calibration points α_i, β_j:

$$Jac(\alpha,\beta) \quad = \quad \left| \frac{\partial(K_\alpha, K_\beta)}{\partial(\alpha,\beta)}(\alpha_i,\beta_j) \right| \tag{3.8}$$

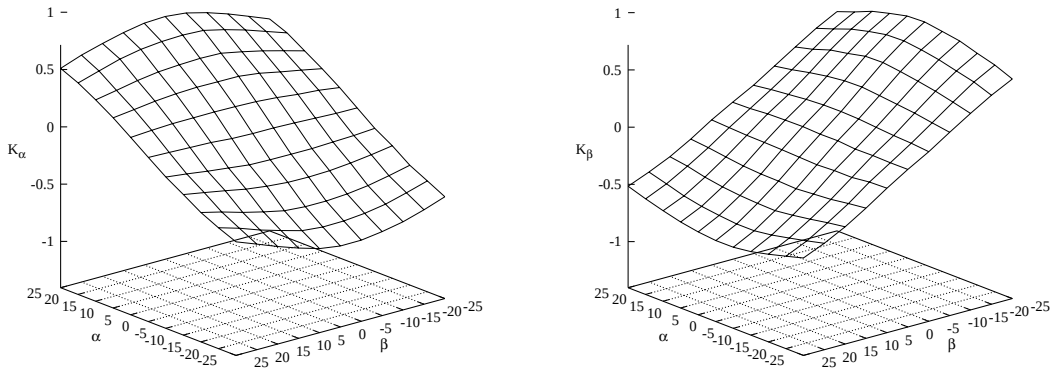

Fig. 3.13: Coefficients for angular calibration $K_\alpha(\alpha,\beta)$, $K_\beta(\alpha,\beta)$ and $K_C(\alpha,\beta)$

For those values at which Jac$(\alpha,\beta)\leq 0$ the flow angles cannot be determined unambigiously. The Jacobian for the mini-4-wire probe are shown in fig. 3.15 for a calibration velocity of C =21 m/s. In this case these limits are outside of a circle given by 30°. The same limits are found for the 6-wire and 4-wire probes.

The independence of the angular characteristics from the velocity characteristics were verified by comparing three sets of calibration coefficients obtained at different calibration velocities C. The lowest velocity was about 10 m/s which is well below the lowest velocity encountered in the flow under investigation.

To obtain the three velocity components in an experiment all three coefficients K_α, K_β, K_C were measured at each time step. By means of a numerical interpolation of the relations in equations 3.9 to 3.11 the corresponding val-

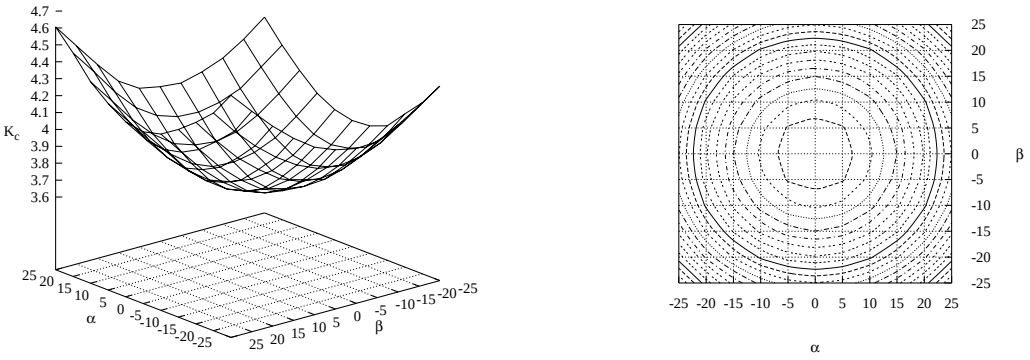

Fig. 3.14: left: Coefficients $K_C(\alpha,\beta)$; right: Contour plots of $K_C(\alpha,\beta)$

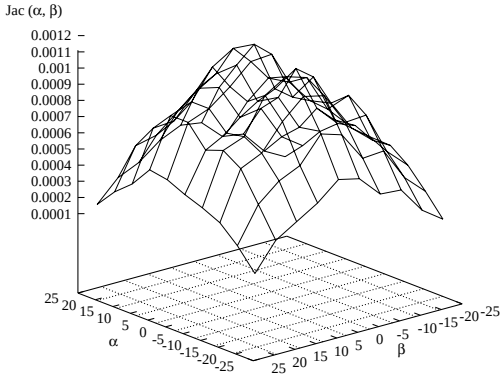

Fig. 3.15: Jacobian of $K_\beta(\alpha,\beta)$ and $K_C(\alpha,\beta)$

ues for α,β and C were derived. From fig. 3.12 the equations 3.2 to 3.4 were obtained and used to compute the three components u, v and w.

$$\alpha = f(K_\alpha, K_\beta) \tag{3.9}$$

$$\beta = f(K_\alpha, K_\beta) \tag{3.10}$$

$$C = \sqrt{\frac{U_1^{*2} + U_2^{*2} + U_3^{*2} + U_4^{*2}}{K_C(\alpha, \beta)}} \tag{3.11}$$

The static accuracy was examined by comparing velocity data computed by the processing method with the actual velocity in the test set-up. The maximal angular error was found to be about 2.5°.

3.4 Laser Doppler Anemometry

As second method for the acquisition of mean flow field data LDA was used. LDA is a non-intrusive method and is able to identify reserve flow (which is a not really possible task with hot-wires). Thus it is an ideal method to quantify the global flow characteristics of the swirling jets and to provide a data basis for comparison with the hot-wire data.

LDA experiments were performed with a two-component system with four beam two channel optics for the velocity components in the directions of $\pm 45^o$ off axis. The laser beams were focused to the crossing volume by transmitting lenses with a focal length of 500 mm. The extension of the probe volume for horizontal traverses is about 4 mm and for vertical traverses 0.16 mm. The horizontal traversing step length is 5 mm and the vertical either 5 mm or 0.5 mm. Directional ambiguity is eliminated by frequency shifts of 40 MHz for both channels. The fringe spacing is about 12 μm and the number of fringes is 12. For each realization 1500 samples were taken which is too small to get reliable fluctuating components but sufficients to determin the mean velocity values.

Seeding was introduced through the chambers surrounding the swirl generators which lead to a homogeneous distribution across the jets upstream of the swirl generator.

3.5 Flow characteristics of the wind tunnel

This section is devoted to a description of the overall characteristics of the jet flows in the wind tunnel. We begin with the influence of the swirl generator on the mean velocity profiles at the jet exits. For this purpose velocity profiles were obtained for different free stream velocities and vane angles to vary the swirl.

The velocity profiles are the initial conditions of the flow regions in which the desired shear layers are produced.

3.5.1 Velocity profiles of the jets at the entry of the test section

Velocity profiles of $\overline{U}$ and $\overline{W}$ as a function of the vane angles at a constant mean bulk axial velocity of $\overline{U}_b$=30 m/s ($\overline{U}_b$ = flow rate in $[\frac{m^3}{s}]$ over cross section $[m^2]$) are shown in fig. 3.16 a and b. The measurements were performed with the two-component LDA-system at x=24 mm. The focal point of the LDA was traversed in radial direction from r=-170 mm to 170 mm. For 0° vane angles the streamwise velocity profiles are “top hat” shaped with thin shear layers. The deviation from axial symmetry was found to be less than 2%. A small azimuthal component corresponding to about 3.3% of U_b is observed. This residual rotation is attributed to the lack of honeycombs or to the nonuniform inflow into the settling chambers .

Fig. 3.16a shows that the shape of the $\overline{U}$-profiles changes continuously in both flows with increasing vane angles. The vanes of the two jets were rotated in the opposite direction so that the jets counter-rotated. A peak formed in the core region of the central jet and a small velocity increase formed in the annular jet in the neighborhood of the trailing edge. The experiences with the model tunnel described earlier in this chapter indicated the formation of the hump as an effect of the screens in the plenum chambers. As a consequence large velocity differences between regions near the nozzle and the core region were created within the central jet. An axial velocity difference of about 15 m/s is found for α_0=60°. Measurements at x=240 mm showed that the central hump still existed. Similar radial distributions of the streamwise velocity were reported, e.g. by Chigier and A. Chervinsky [48] in a swirling jet generated by tangential inlets and by Rose [49] in a swirling jet generated by a rotating pipe. Due to the cylindrical trailing edge a wake visible as a velocity deficit is formed. The off-sets of the wakes in the differ-

ent cases result from the traversing mechanism of the LDA and not from the flow.

Figure 3.16b illustrates the variation of the azimuthal velocity component which increases with increasing vane angle. In the $\overline{W}$-profiles we find a large constant gradient $\partial\overline{W}/\partial r$ in the core region of the central jet which denotes a solid body rotation. Here the highest values of the azimuthal velocity occur. The absolute values of $\overline{W}$ of the annular jet also increase towards the jet axis. For the extreme case of Ψ_0=60° the maximal $\overline{W}$-value is equal to 67% of U_b.

For a further evaluation of the inlet conditions the axial and azimuthal vorticity components $\overline{\omega}_x$ and $\overline{\omega}_z$ were computed using the following equations:

$$\overline{\omega}_x \cong \frac{1}{r}\left(\frac{\partial r\overline{W}}{\partial r}\right) \qquad \text{and} \qquad \overline{\omega}_z \cong \overline{\omega}_\varphi = -\left(\frac{\partial\overline{U}}{\partial r}\right) \tag{3.12}$$

In fig. 3.17 $\overline{\omega}_x$ and $\overline{\omega}_z$ are shown for the case where $\Psi_0 = 40°$ and $\Psi_1 = -40°$. Two peaks of opposite signs for $\overline{\omega}_z$ appear at the position of the trailing edge as a result of the wake-type $\overline{U}$-profile due to the trailing-edge. The $\overline{U}$-gradient in the jet core is responsible for another increase of $\overline{\omega}_z$ in that region. As the traversing mechanism of the LDA-equipment was limited in range, the measurements were only carried out from r=0 to r=-200 mm.

The distribution of $\overline{\omega}_x$ in the central jet shows zero vorticity in a region between the core and the trailing edge. In the annular region near the trailing edge, in which the shear layer between the two jets is created, only vorticity due to the counter-rotation is generated. This potential-vortex distribution is an important characteristic as the same situation is found in plane configurations. Thus another criterium for comparability with plane configurations is satisfied. In the annular jet $\overline{\omega}_x$ exists only in the periphery near the test-section wall outside of the region of interest, i.e. outside of the shear layer.

Although the object of this investigation is not swirling jets but rather three-dimensional shear layers, experiments were performed where only the inner jet was activated. For this case the influence of the vane angles Ψ_0, i.e. the swirl, on the generation of the rotational motion was evaluated. In the review section several swirling jet studies were presented in which the swirl number S was used for this purpose. We used the definition of S in eqn. 2.15 to compute swirl numbers as a function of Ψ_0. The vane angle α_0 was varied from 0° to 80° in steps of 20°. For each angle setting $\overline{U}_b$ was varied from 5 to 30 m/s in increments of 5 m/s. The measurements were taken at x =24

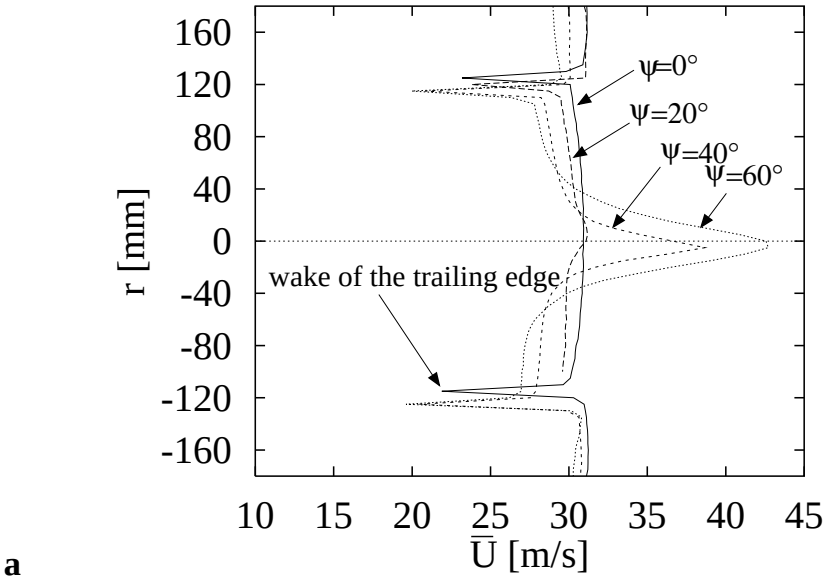

a

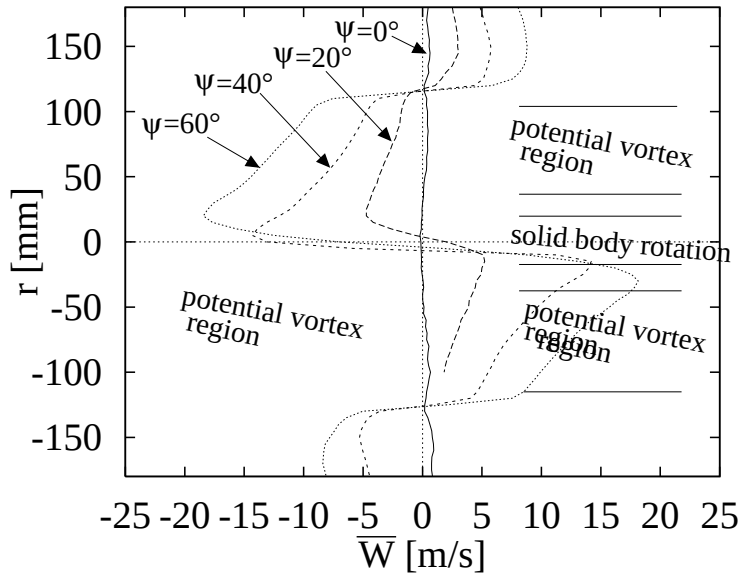

b

Fig. 3.16: Initial profiles (i.e. x=24 mm) of $\overline{U}$ (**a**) and $\overline{W}$ (**b**) as a function of the vane angles Ψ (absolute values)

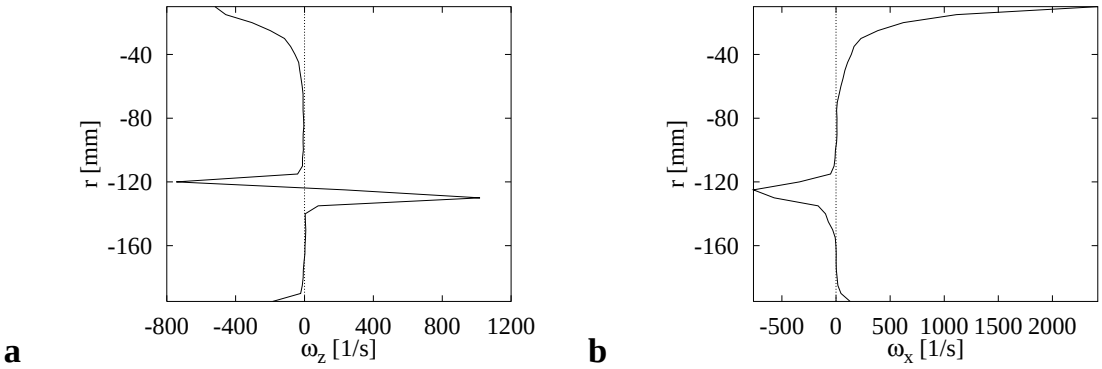

Fig. 3.17: Initial vorticity profiles of $\overline{\omega}_z$ (**a**) and $\overline{\omega}_x$ (**b**) for Ψ_0=-40° and Ψ_1=40°

mm downstream of the nozzle exit which corresponds to x/D=0.1. Fig. 3.18 shows that the swirl number increases with Ψ_0. The reason for this is that $\overline{U}$ and $\overline{W}$ grow at the same location resulting in a non-linear growth of the axial flux of angular momentum which is the nominator in the swirl number definition.

Increasing $\overline{U}_b$ results also in an increase of S. This influence gets smaller at higher $\overline{U}_b$-values. The maximum swirl number obtained is 0.6. At this values vortex breakdown, i.e. the beginning of flow reversal, has been observed in the literature for swirling jets ([36], [50]). In our case this was not observed but rather an enlargement of the hump in the jet core occurred. Obviously there forms no pressure gradient in our case which could cause a flow reversal.

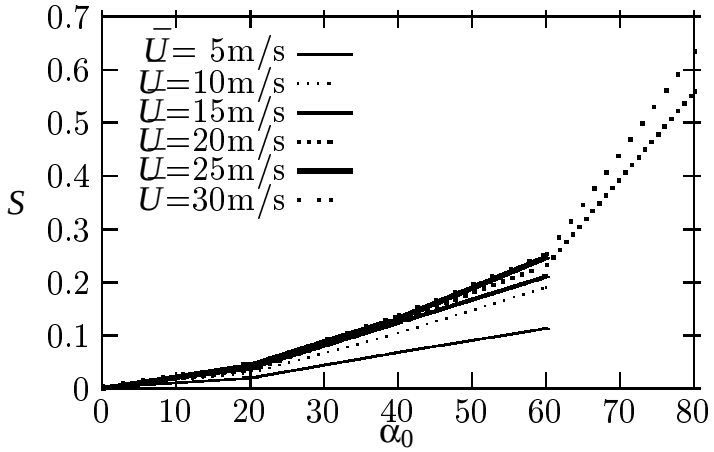

Fig. 3.18: Dependence of S on Ψ_0 and U_b

3.5.2 Initial conditions of the shear layer

The boundary layers originating from the trailing edge play an important role in the development of the downstream shear layers (see [12]). Hence, their degree of axisymmetry and their thicknesses were studied using a N-wire (type a according to section 3.3) oriented in the azimuthal direction and positioned 2 mm downstream of the trailing edge. Both boundary layers were tripped at x=-100 mm with sand paper (granulation 80). Fig. 3.19 shows the profiles of $\overline{U}$ and $\overline{u'^2}$ of the boundary layers without swirl. The free stream velocity was about 21 m/s and for the swirling case Ψ_0 and Ψ_2 were set to +40°. The profiles were obtained at 12 equidistant azimuthal positions covering the range of 0° to 360°. The $\overline{U}$-profiles show a good degree of collapse with a maximum velocity deviation of about 2.5%.

When subjected to rotational motion the thicknesses of the boundary layers vary in a different manner in the two jets (fig. 3.20). In table 3.2 different measures for the boundary layer thickness indicate this behavior (δ_1, Θ). The external layer decreases in thickness when subjected to rotation whilst the inner layer increases (This can be estimated from the $\overline{u'^2}$-profiles). For both flows the same free stream velocities and the same vane angle settings were chosen. It is assumed that this phenomenon results from the azimuthal velocity distribution: The outer distribution is centrifugaly stable as the azimuthal component increases with growing radius; in contrast the inner layer has a centrifugally unstable distribution.

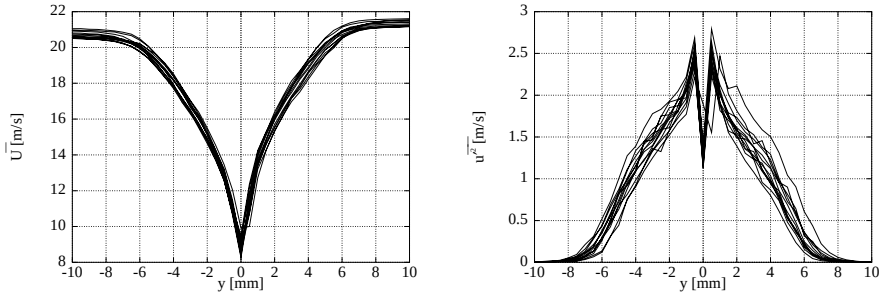

Fig. 3.19: Profiles of $\overline{U}$ and $\overline{u'^2}$ in the boundary layer without swirl

In the plots of $\overline{u'^2}$ over y (fig. 3.19 and fig. 3.20) the turbulence level in the inner boundary layer with swirl is higher than in the outer layer as a consequence of the different stability-behaviours.

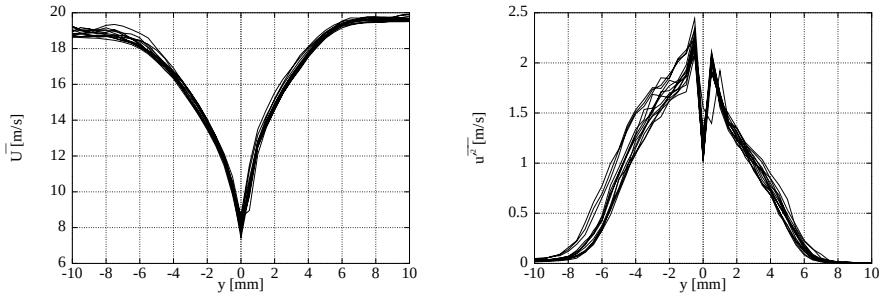

Fig. 3.20: Profiles of $\overline{U}$ and $\overline{u'^2}$ in the boundary layer with swirl

In tab. 3.2 some turbulence levels $\sqrt{\overline{u'^2}}/\overline{U}$ obtained outside of the boundary layers but within the initial shear layer region are presented. Both jet turbulence levels increase in the presence of rotation. The highest level of 0.5 % is found in the inner rotating jet and is sufficiently low for the desired purpose. However, the turbulence values near or within the core of the latter are much higher.

jet	central		annular	
$\overline{U}_b$ [m/s]	19		19	
α	0°	40°	0°	40°
δ_1 [mm]	1.87	2.05	1.41	1.16
Θ [mm]	1.09	1.18	0.89	0.75
$H = \delta_1/\Theta$	1.72	1.45	1.59	1.55
$\sqrt{\overline{u'^2}}/\overline{U}$	0.2	0.5	0.2	0.3
Re_Θ	1990	1065	1714	895
Re_D	8.0 x 10^5	4.8 x 10^5	8.0 10^5	4.8 10^5

Tab. 3.2: Initial properties of the jets with and without swirl. ($Re_\Theta = \Theta\ \overline{U}_b/\nu$; $Re_D = D\ \overline{U}_b/\nu$); $\sqrt{\overline{u'^2}}/\overline{U}$ measured at *y*=-10 mm (central jet) and *y*=+10 mm (annular jet).

Summarizing the observations from this section, we find that the flow conditions produced by the wind tunnel are suitable for the objective of this work. The central jet exhibits three characteristic domains at the presence of swirl: A solid body core about the centerline, an annular shear layer type domain at the boundary and an annular potential vortex type domain between the other two. The existence of the high vorticity core does not seem to have a measur-

able influence on the shear layers under investigation. The velocity signals in the core and in the shear layer measured simultaneously with two hot-wires did not reveal any correlation (the operating conditions were the same as in the shear layers to be investigated). Apparently the nozzle diameters chosen are large enough to inhibit the communication between disturbances in the core region and the shear layer. This favorable situation persists up to vane angles of Ψ_0=60$\circ$ which presents a limit. For the flow configurations investigated in this study the vane angles were kept below 60°.

It seems worthwhile to mention that in the study by Singh and Uberoi [38] on isolated trailing vortices presented in the introductory part a flow similar to the swirling central jet was created at the tip of a wing.

3.5.3 Modification of the velocity profiles of the central jet

While testing the wind tunnel a special modification was applied to the central jet with the intention to change the shape of the velocity profiles at the exit. The modification consisted of a circular inlet at the upstream end of the inner plenum chamber so that a non-rotating jet was created at the core of the central jet. This additional inlet has a diameter of 400 mm and is made of a round duct of 300 mm length containing a honey comb. Fig. 3.21 shows the resulting changes in the velocity profiles for two bulk velocities and two vane angle settings. For Ψ_0=60° the central hump in $\overline{U}$ has become much smaller and the profile of $\overline{W}$ shows a large core region (up to r=70 mm) with a linear distribution indicating solid body rotation. The swirl number in this case corresponds to the flow without axial inlet and Ψ_0=40°. Obviously, the inflow of non-rotating fluid through the axial inlet must be compensated by an increased vane angle in order to obtain the same swirl number.

In the case of Ψ_0=18° and $\overline{U}_b$= 20 m/s the resulting $\overline{W}$-profile shows a non-rotating core region which indicates that the angular momentum created by the vanes has not yet achieved to entrain the core region of the jet.

These results are interesting as they show that through a simple modification of the wind tunnel construction a jet with different flow characteristics, i.e. vorticity-distribution can be generated. This might be a useful feature for investigations on the influence of the azimuthal velocity profile on the evolution of rotating shear layers.

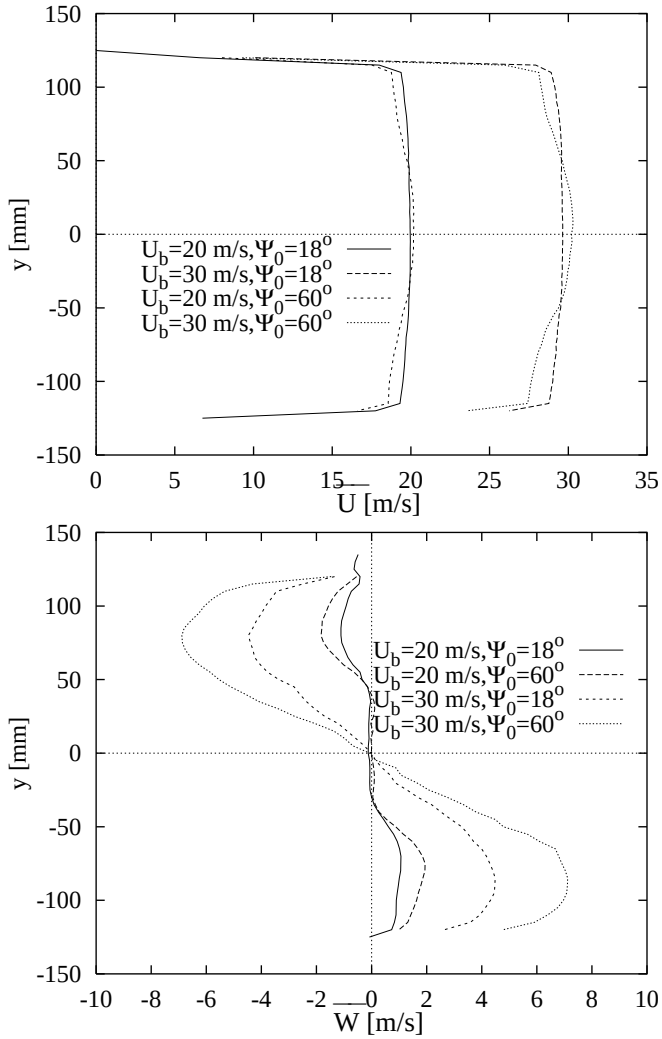

Fig. 3.21: Modified velocity profiles of the central jet via axial inlet, LDA measurements

4. Experimental results

As mentioned in the introductory part (2) , the aim of this investigation is to study the effects of three-dimensionality of the basic flow (condition II) on the behavior of shear layers. Here we investigated the asymmetric oblique mixing layer and the shear layer between parallel oblique streams. The symmetric oblique shear layer was studied by the research group in Poitiers.

It is convenient to use abbreviations for the different configurations investigated. These are:

- NPOSL : **n**on **p**arallel **o**blique **s**hear **l**ayer (counter-rotating jets)
- POSL : **p**arallel **o**blique **s**hear **l**ayer (co-rotating jets)
- CSL : **c**lassical **s**hear **l**ayer(non-rotating jets)

The first case will be denoted by NPOSL (**n**on **p**arallel **o**blique **s**hear **l**ayer) and the latter by POSL (**p**arallel **o**blique **s**hear **l**ayer). As a reference case results from measurements in the classical shear layer (CSL) are also presented.

Table 4.1 presents information on three vane angle settings of the swirl generators in order to generate the flow configuration investigated. The values for α_0 and Ψ_1 were adjusted such that the resulting profiles of $\overline{U}$ and $\overline{W}$ satisfied the desired shear layers. The parameters λ and λ_v (eqns. 2.4 and 2.5) are also listed in the table. The NPOSL is the only case where λ and λ_v differ significantly. λ_v is increased due to the effect of the additional cross-shear (i.e. $\Delta\overline{W}$).

4.1 Smoke visualizations

Flow visualizations are used together with quantitative measurements especially for the study of the structure of turbulent flow fields. A major advan-

Shear layer type	Ψ_0	Ψ_1	λ	λ_ν
CSL	0°	0°	0.228	0.228
NPOSL	-40°	+60°	0.247	0.348
POSL	+40°	+60°	0.250	0.251

Tab. 4.1: Investigated shear layer configurations

tage of this qualitative method is the quick and usually simple acquisition of instantaneous and spatially dense information on large regions of the flow. It is therefore not surprising that the early conceptual formulations of coherent structures were based on flow visualizations (e.g. Brown & Roshko[10]). The most common method of flow visualization is by tracers in the flow.

In the present work smoke was introduced in two ways into the flow. First the chamber around the swirl generator of the central jet was supplied with smoke so that it could travel downstream into the stream of the central jet. Secondly smoke was inserted through the ring gap (fig. 3.9) into the boundary layer of the inner jet. Experiments were done with various flow parameters: the central jet with and without swirl or both jets with and without swirl. The lowest free stream velocity was about 2 m/s. With a thin laser sheet (5 mm thickness) both the cross-section and longitudinal-section were illuminated providing a two-dimensional view. For a three-dimensional view the entire flow field was illuminated using strong light projectors. The flow visualized was then either recorded by VHS so that time sequences of about 20 s length were obtained or photographed with a camera (in this case a flash light was used).

It turned out that this visualization technique did not reveal sufficient details for a description of the structural organisation of the flow. It was impossible to get clear images of the global character of the flow structures. Apparently too many modes - instationary as well as stationary ones - coexist to allow an unambigious identification. This was the reason why the flow parameters chosen for the visualizations were not the same as those used for the hot-wire measurements. Of the few views which provided some details of the structure three samples are shown in figs. 4.1-4.3.

Experiments with no swirl (fig. 4.1), i.e. the classical shear layer cases, show the formation of vortex rings and their growth with increasing downstream distance. Visualizations of the cross-section show also the existence of stationary, streamwise structures. Variation of the free stream velocity $\overline{U}_b$

results in an increasing number of these structures.

In the case of the single swirling jet vortex rings are also observed (not shown here). It was not possible to determine whether the rings are tilted and thus an indication of a helical mode. To check wether this information is more accessible at higher values of swirl, visualizations were performed at higher swirl but even then the situation was not clear. The cross-section in fig. 4.2 shows that the boundary of the central jet has mushroom shaped bulges indicating the exsistence of streamwise vortices. The video sequences the impression was obtained that some of them are stationary while others travel along the circumference. Similar observations were also made in the case of two jets with different axial velocities and the inner one with swirl (fig. 4.3).

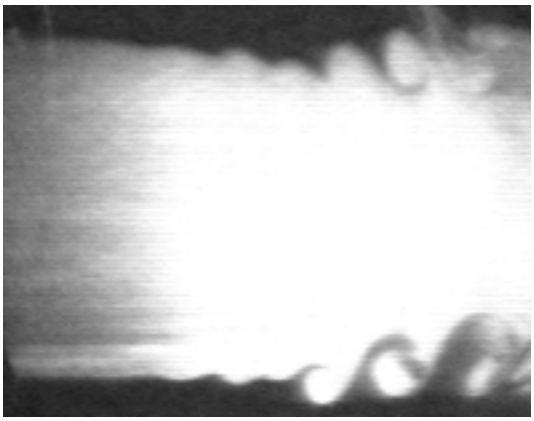

Fig. 4.1: Smoke visualization (x – r-plane) obtained at x/D=1.0, U_{b0}=1m/s, U_{b1}=0, Ψ_0=0^o

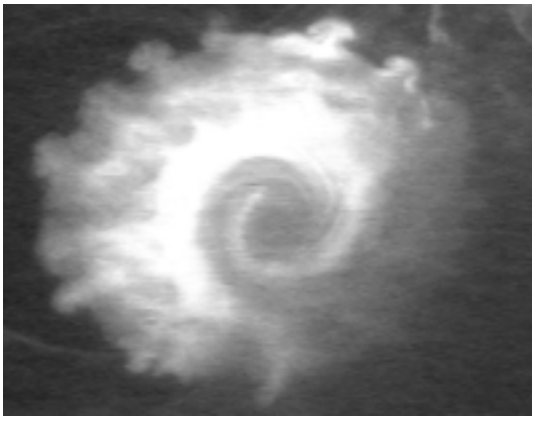

Fig. 4.2: Smoke visualization (plane x=const.) obtained at x/D=1.0, U_{b0}=2m/s, U_{b1}=0, Ψ_0=40^o

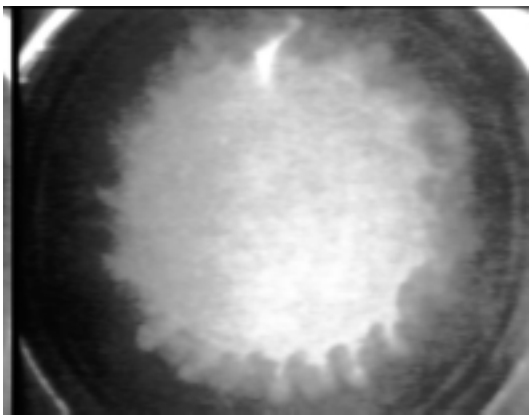

Fig. 4.3: Smoke visualization (plane x=const.) obtained at x/D=1.0, U_{b0}=2 m/s, U_{b1}=3.2 m/s, Ψ_0 =-80^o, Ψ_1= 0^o

4.2 Statistical description based on single point measurements

Profiles of mean and fluctuating velocities for the three cases CSL , NPOSL and POSL obtained with the 4-wire probe at five axial positions x=300, 400, 500, 600 and 700 mm are presented in the following. The sampling time was 16 s and the sampling frequency 2000 Hz. The data were low-pass filtered at 1000 Hz. The plots presented in the figures are typically ordered in three columns where the left column shows the CSL , the middle the NPOSL and the right the POSL .

4.2.1 Mean velocity profiles with classical normalization

Fig. 4.4 presents mean velocity profiles of the components $\overline{U}$, $\overline{V}$ and $\overline{W}$ normalized with $\overline{U}_0 - \overline{U}_1$. The transverse position was defined as $y - y_{0.5}/b$. $\overline{U}_0$ is about 26 m/s and $\overline{U}_1$ 16 m/s, both depend weakly on thedegree of swirl.

For all three cases the longitudinal component $\overline{U}$ shows a self-similar behaviour typical of shear layers. Furthermore, the profiles illustrate that in the shear layer region $\partial\overline{U}/\partial r$-gradients which were observed in the core region of the central jet and described in section 3.5.1 do not play any role in the actual shear layers.

For the CSL case $\overline{V}$ is negative in the central jet ($y < 0$) and about zero in the external jet. This means that there is a transverse motion from the low speed to the high speed side. The $\overline{V}$-profiles are no longer self-similar due to a negative gradient $\partial\overline{V}/\partial x$ but the shape of the profiles remains similar.

For the NPOSL case the values of $\overline{V}$ are positive in the central region while being near to zero in the external part. In contrast to the CSL -case the dominating transversal flow is now directed towards the external jet. This trend is further confirmed by the isotach contours of $\overline{U}$ presented later in section 4.2.5 which reveal a outward turn of the shear layer, suggesting that the $\overline{W}$-distribution influences also the $\overline{V}$-profiles.

The POSL configuration shows qualitatively a similar distribution as that of case CSL with the difference that in the central jet the $\overline{V}$-profiles are negative throughout.

Finally, we consider the $\overline{W}$ distributions which are the primary source for the different behavior of the three flows. In the CSL $\overline{W}$ should be nominally

zero. However, the results show that this is not quite true as small values are measured. This indicates that the vane angle settings $\Psi_0 = \Psi_1 = 0$ are not sufficient to avoid the flow in the wind tunnel to be free of swirl (this point was already addressed in section 3.1). It will be shown later that the shear stress $\overline{u'w'}$ is also affected by these residual values of $\overline{W}$.

The $\overline{W}$-profiles of the NPOSL case indicate that the velocity difference in $\overline{W}$ has about the same magnitude as the velocity difference in $\overline{U}$. The profiles do not show self-similarity as did the $\overline{U}$-profiles. This indicates that the normalization by $\overline{U}_0 - \overline{U}_1$ is not suitable. Furthermore the slopes of the profiles for $y < -0.5$ increase with growing streamwise distance.

The $\overline{W}$-distribution of the POSL case shows that although the two jets are co-rotating a velocity gradient $\partial\overline{W}/\partial y$ between the central and external jet remains. As a result the maximal velocity difference $\Delta\overline{W}_{max} = 0.2(\overline{U}_0 - \overline{U}_1)$ occurs. A better adjustment of the vane angles with the intention to eliminate this gradient is difficult because an independent modification of the $\overline{U}$ and the $\overline{W}$ profiles is not possible in this tunnel.

4.2.2 Flow angles

Using the velocity components $\overline{U}$ and $\overline{W}$ the flow angle α was calculated as a function of y. The result is presented in fig. 4.5. In the CSL angles less than 1° were obtained.

The counter-rotation of the coaxial jets used for the generation of the NPOSL is manifested in the opposite sign of Ψ_0. The maximum Ψ-values are about 15° (inner jet) and about -15° (outer jet).

In the co-swirling case (POSL) the maximum flow angles obtained in both jets are of the same magnitude ($\approx 12°$). Lower values were found in the shear layer center which is an effect of the trailing edge wake. The angles grow with streamwise distance in both jets.

4.2.3 Reynolds stress profiles with classical normalization

Fig. 4.6 represents the normal stresses $\overline{u'^2}/\Delta\overline{U}^2$, $\overline{v'^2}/\Delta\overline{U}^2$ and $\overline{w'^2}/\Delta\overline{U}^2$ for all three cases. The $\overline{u'^2}/\Delta\overline{U}^2$-profiles of the CSL show the typical distribution of plane shear layers with peak values of 0.032. The profiles collapse fairly well - another indication of self-similar behavior.

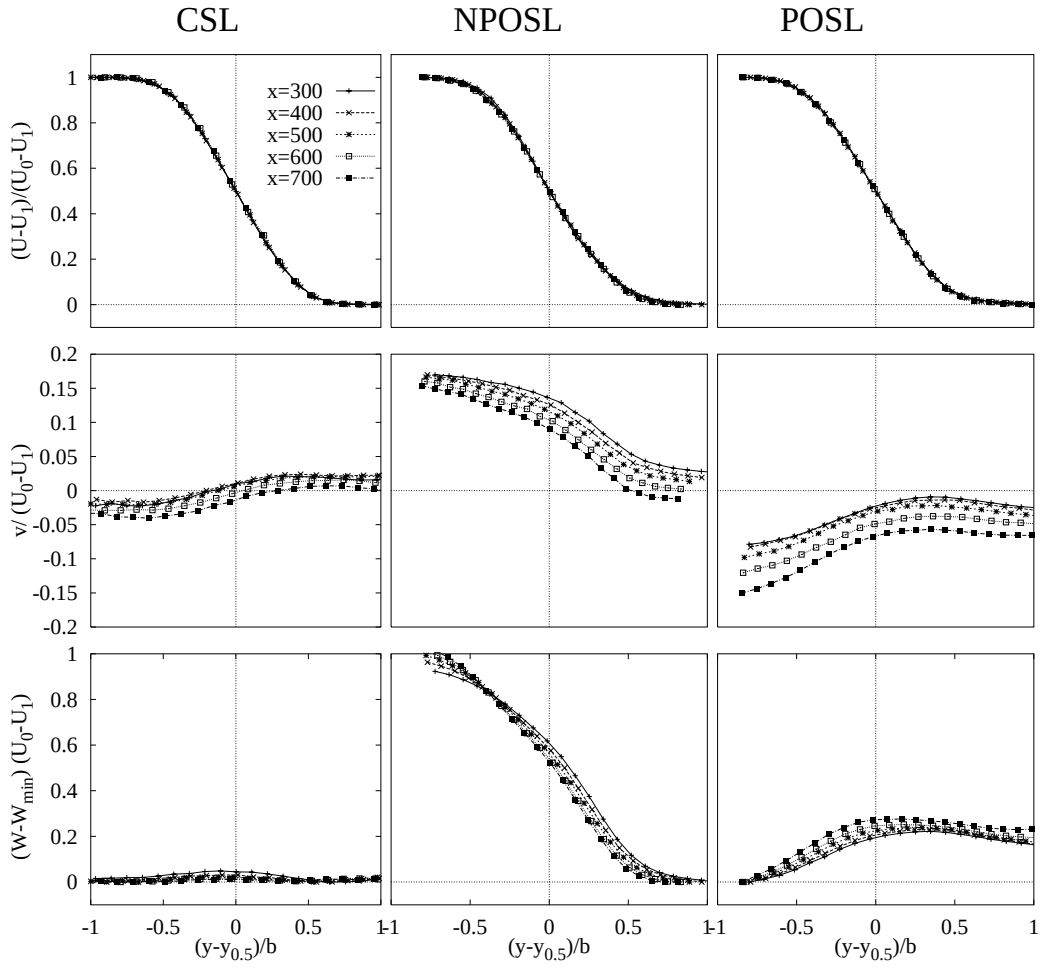

Fig. 4.4: Mean velocity profiles

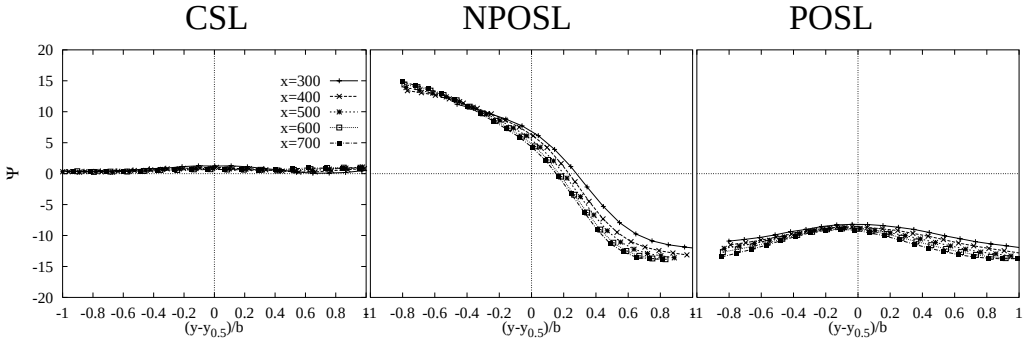

Fig. 4.5: Flow angle Ψ

For the NPOSL case the peak values of $\overline{u'^2}/\Delta\overline{U}^2$ are maximized by up to 5% . This is an effect of the additional shear introduced by the non-parallel streams. The peak values increase with streamwise distance so that there is no self-similarity. The $\overline{u'^2}/\Delta\overline{U}^2$-distribution of the POSL case shows peak values larger than in the classical case but smaller than in the asymmetric case. Again, there is no self-similarity.

The $\overline{v'^2}/\Delta\overline{U}^2$-distributions show qualitatively the same characteristics as the $\overline{u'^2}/\Delta\overline{U}^2$-profiles for all three cases. The largest increase is found again for the NPOSL case. Depending on the transverse position considered two degrees of collapse are observed in NPOSL and POSL . For $y<0$ (i.e. smaller values of r) the collapse is little whereas for $y>0$ it is better. Analog observations are made for the $\overline{w'^2}/\Delta\overline{U}^2$-distributions.

In all three cases the relations between the normal stresses are found to be $\overline{u'^2} > \overline{w'^2} > \overline{v'^2}$. The next quantities considered are the shear-stresses in fig. 4.8. The $\overline{u'v'}/\Delta\overline{U}^2$-profiles of the CSL exhibit a self-similar character and typical peak-values of about 0.012. With the presence of cross-shear in the POSL case the peak-values grow significantly (about 30%) and the collapse of the profiles is less pronounced on the inner side of the shear layer ($y<0$). A comparable tendency is observed in the POSL case but the peak-values have not increased as much as in the NPOSL . The values are about 16% higher than in the CSL case. Collapse of the $\overline{u'v'}/\Delta\overline{U}^2$-profiles is not achieved due to a continuous growth of the peak values with downstream distance shown in fig. 4.7.

The shear stresses $\overline{v'w'}/\Delta\overline{U}^2$ and $\overline{u'w'}/\Delta\overline{U}^2$ should be nominally zero in the CSL . However, small negative values were measured of about 9% and 27% of $\overline{u'v'}/\Delta\overline{U}^2$, respectively. To explain this we must reconsider the azimuthal velocity distributions (fig. 4.4). The $\overline{W}$-profile showed that although the vane angles of the swirl generators were adjusted to zero (i.e. $\Psi_0 = \Psi_1 = 0°$) , a weak azimuthal component $\overline{W}$ corresponding to about 2% of ΔU remained in both jets. This small value created a slight co-rotation. The existence of the secondary shear stresses $\overline{v'w'}/\Delta\overline{U}^2$ and $\overline{u'w'}/\Delta\overline{U}^2$ result from this weak rotation. A similar behaviour was found for the profiles of the POSL case where the jets also co-rotate. In this case $\overline{v'w'}/\Delta\overline{U}^2$ and $\overline{u'w'}/\Delta\overline{U}^2$ are also non-zero but have much higher peak-values than in the CSL case. Thus the weak co-rotation explains the non-zero secondary shear stresses in the CSL case. It should be noted that the two shear stresses may partly be due to

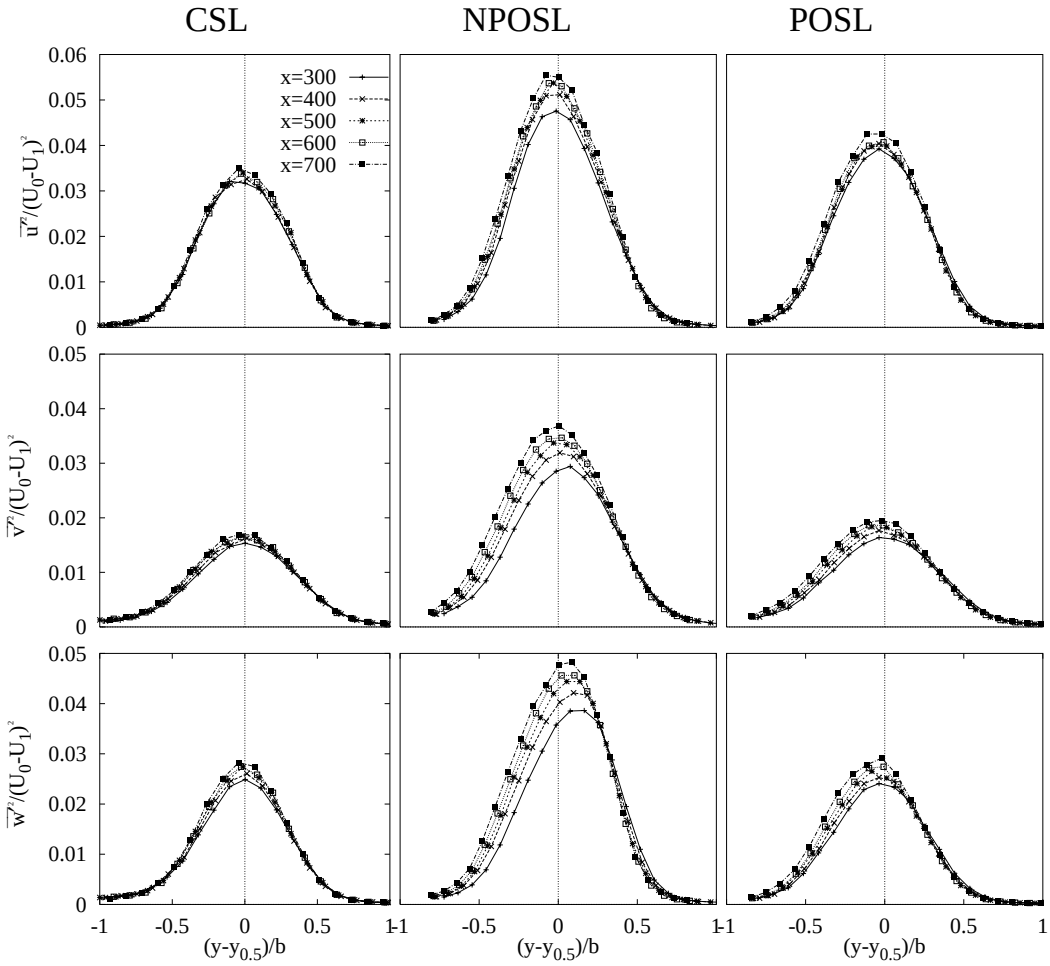

Fig. 4.6: normal stresses

inevitable errors in probe rotation and alignment. The difficulty of obtaining zero values of secondary shear stresses in nominally two-dimensional shear layers was also demonstrated by the results of other experimentalists. For instance in the experiment by Metha et al.[17] in a non-swirling jet $\overline{u'w'}/\Delta\overline{U}^2$ was found to be around 18% of $\overline{u'v'}/\Delta\overline{U}^2$.

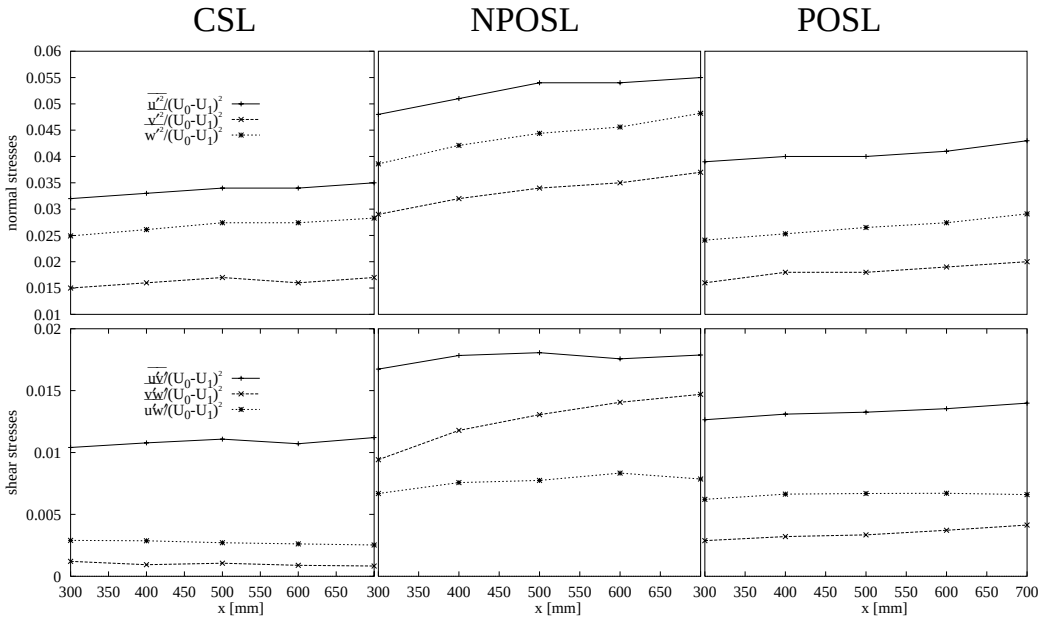

Fig. 4.7: Streamwise evolution of the Reynolds stresses

For the NPOSL configuration the shear stress $\overline{v'w'}/\Delta\overline{U}^2$ reaches peak values of about 70% of $\overline{u'v'}/\Delta\overline{U}^2$ and the peak values grow significantly in streamwise direction (fig. 4.7). The $\overline{u'w'}/\Delta\overline{U}^2$ magnitudes go up to only about 50% of $\overline{u'v'}/\Delta\overline{U}^2$. The profiles have an asymmetric double-hump with higher values in the outer jet ($y > 0$).

The absolute maximum values of all Reynolds-stresses are summarized in Tab. 4.2 for the three cases CSL , POSL and NPOSL . For comparison values obtained by other authors are listed as well. The values of the CSL are in good agreement with those obtained in plane configurations. In the single jet configuration studied by Mehta et al. [17] changes comparable to the present cases take place when swirl is applied. However, there are no experimental data available on configurations corresponding to the POSL and NPOSL case.

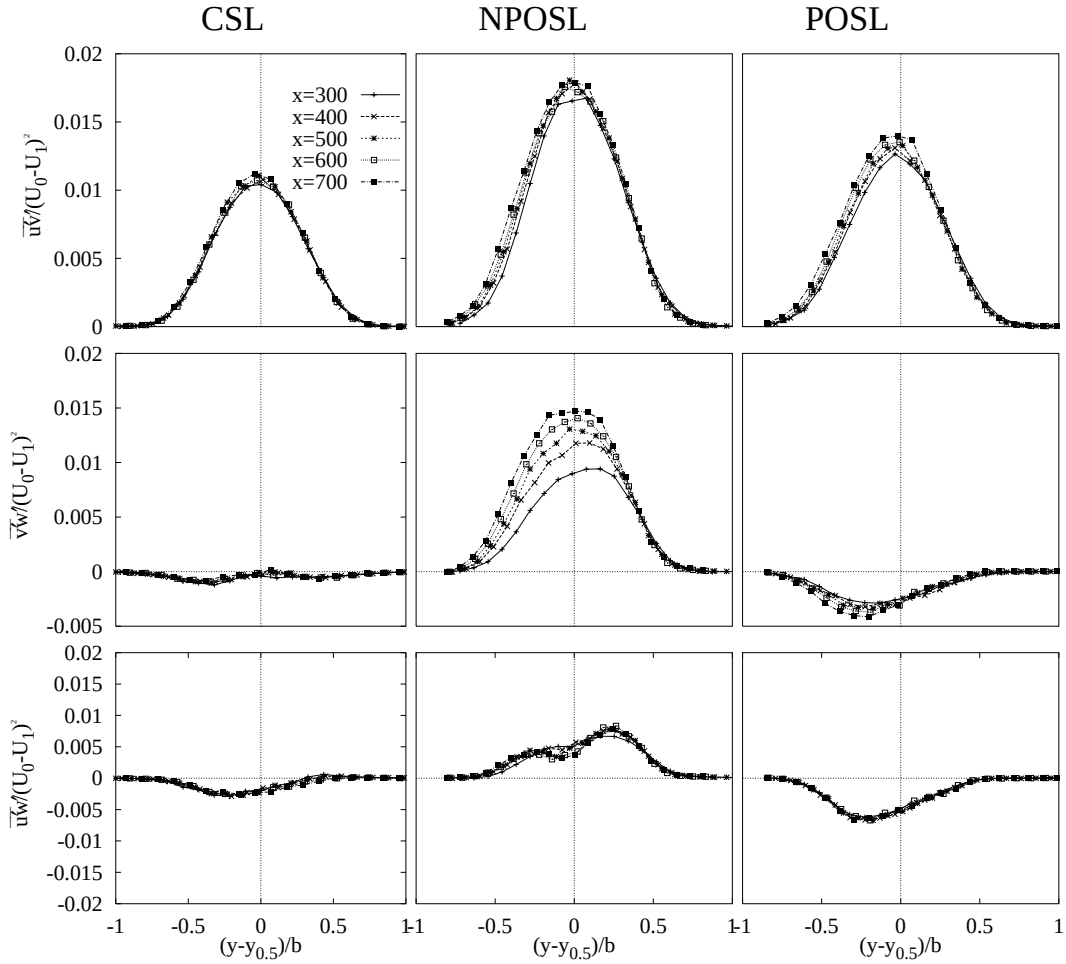

Fig. 4.8: shear stresses

author	configuration	$\frac{\overline{u'^2}}{\Delta U^2}$	$\frac{\overline{v'^2}}{\Delta U^2}$	$\frac{\overline{w'^2}}{\Delta U^2}$	$\frac{\overline{u'v'}}{\Delta U^2}$	$\frac{\overline{v'w'}}{\Delta U^2}$	$\frac{\overline{u'w'}}{\Delta U^2}$
present work	CSL , no swirl	0.033	0.017	0.028	0.011	0.001	0.003
present work	NPOSL , counter swirl	0.055	0.036	0.048	0.018	0.015	0.008
present work	POSL , co-swirl	0.043	0.020	0.029	0.014	0.004	0.007
Wygnanski & Fiedler [51]	pl. s.l., no swirl	0.032	0.020	0.023	0.009	–	–
Oster & Wygnanski [52]	pl. s.l., no swirl	0.032	0.023	–	0.017	–	–
Metha &Westphal [53]	pl. s.l., no swirl	0.032	0.014	–	0.014	–	–
Mehta et al. [17]	a.s.l., no swirl	0.031	0.018	0.020	0.011	0.0003	0.001
Mehta et al. [17]	a.s.l., S=0.2	0.032	0.017	0.021	0.013	0.003	0.003
Mehta et al. [17]	a.s.l., S=0.4	0.035	0.017	0.023	0.015	0.007	0.007

Tab. 4.2: Maximum turbulent quantities from different authors (pl.= plane; s.l. = shear layer; a.= axisymmetric)

4.2.4 Application of the modified normalization to the NPOSL

The results of the NPOSL case exhibit a remarkable lack of self-similarity for the quantities $\overline{W}/\Delta\overline{U}$, $\overline{v'^2}/\Delta\overline{U}^2$, $\overline{w'^2}/\Delta\overline{U}^2$ and $\overline{v'w'}/\Delta\overline{U}^2$. Therefore, we want to introduce the modified normalization of section 2.4 which takes into account the effects of cross-shear and curvature. As can be seen in fig. 4.9 the profiles $\overline{W}^\star$, $\overline{v'^2}$, $\overline{w'^2}$ and $\overline{v'w'}$ agree better with each other justifying the normalization based on the angular momentum. Only $\overline{v'w'}/\Delta\overline{U}^2$ does not show trend, although for axial station downstream of 400 mm the profiles come closer to each other.

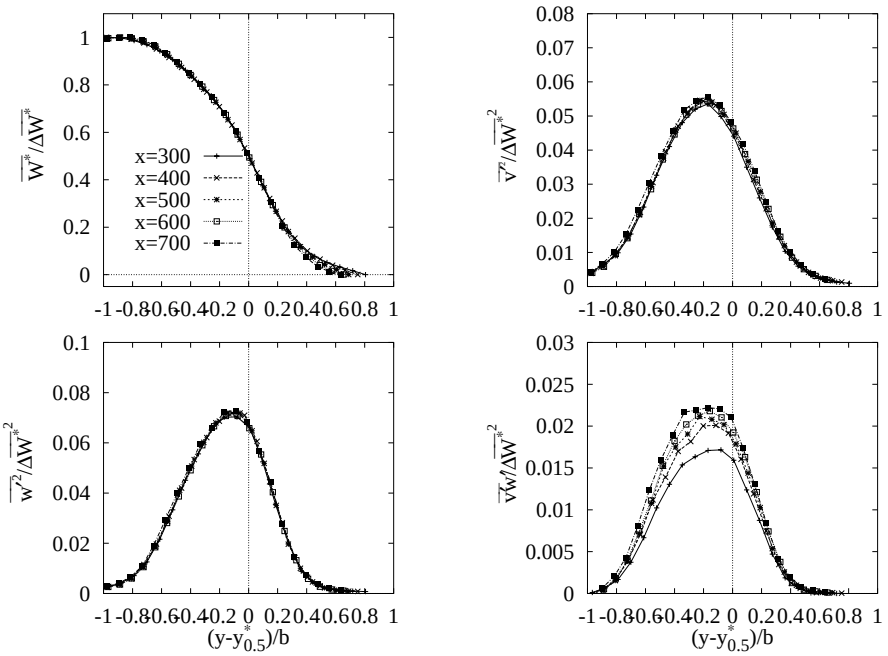

Fig. 4.9: Mean velocity and Reynolds stress profiles with modified normalization

4.2.5 Spread characteristics

The evolution of the shear layer is presented by isotachs in fig. 4.10. The isotachs correspond to distances $y_{0.05}$, $y_{0.50}$, $y_{0.95}$. The comparison shows that the NPOSL case has the fastest growth and the centerline $y_{0.5}$ is inclined towards the outer jet. When the $\overline{V}$-distribution were presented in fig. 4.4 this behavior was already indicated by the outward orientation of the $\overline{V}$-values.

The centerline of the other two cases remain parallel to the streamwise direction. The POSL , which grows faster than the CSL , shows a larger spread angle on the high speed side than on the low speed side. The $\overline{V}$-profiles of this case shown earlier indicated strong negative values in the inner jet, thus confirming the observation.

The virtual origins found by extrapolation of the isotachs are x=-125 mm, -80 mm and 0 mm for the CSL , POSL and the NPOSL , respectively.

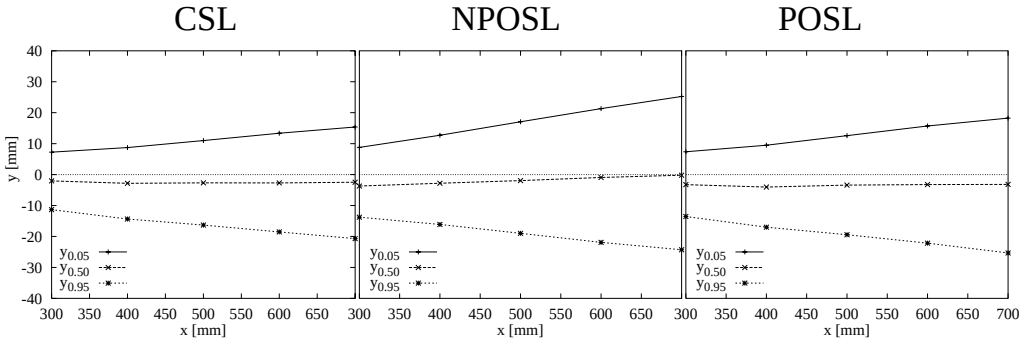

Fig. 4.10: isotachs of $y_{0.05}$, $y_{0.50}$ and $y_{0.95}$

The evolutions of the momentum thickness Θ and of the vorticity thickness δ_ω are presented in fig. 4.11. Both measures show a linear growth rate for the three configurations and the maximum growth rate is found for the NPOSL case followed by POSL and CSL .

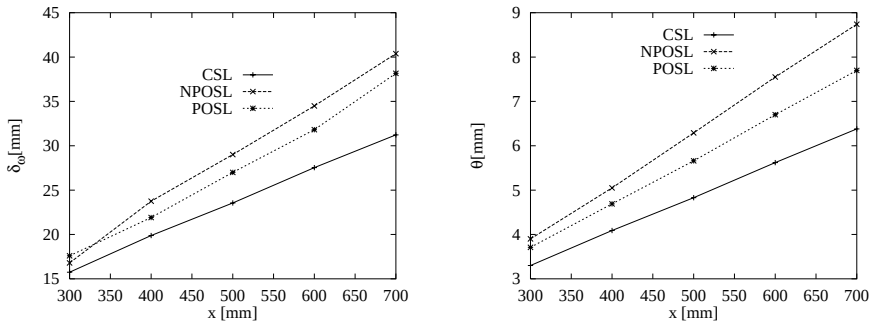

Fig. 4.11: development of δ_ω and Θ

The growth rates of the classical case are $d\delta_\omega/dx$=0.042 and $d\Theta/dx$=0.0075 and are in good agreement with values from other experimentalists tabulated in tab. 4.2.5. The two versions of the spread parameters λ (eqn. 2.4) and λ_ν (eqn. 2.5) are also shown in the table. Linear growth rates for a swirling mixing layer were also found by Mehta et al. [17]. The values from their

experiments show higher growth rates due to the larger spread parameter λ. There the spread increases also with increasing swirl-number.

author	configuration	λ	λ_ν	$d\delta_\omega/dx$	$d\Theta/dx$
this work	CSL	0.23	0.23	0.042	0.008
this work	NPOSL	0.25	0.35	0.057	0.013
this work	POSL	0.25	0.25	0.050	0.010
Delville [54]	pl. s.l.	0.26	–	0.041	0.0085
Mehta [17]	a.s.l. S=0	1.0	–	0.072	–
Mehta [17]	a.s.l. S=0.2	1.0	–	0.071	–
Mehta [17]	a.s.l. S=0.4	1.0	–	0.099	–

Tab. 4.3: Shear layer growth rates from different authors(pl.= plane; s.l. = shear layer; a.= axisymmetric)

In fig. 4.12 the dependence of the vorticity thickness on the spread parameter is illustrated by a collection of measurements from various authors. The points from the present work are well within the scatter band of the results of other investigations suggesting that the modified spread parameter λ_ν which was used here for the NPOSL can also describe the evolution of three-dimensional shear layers.

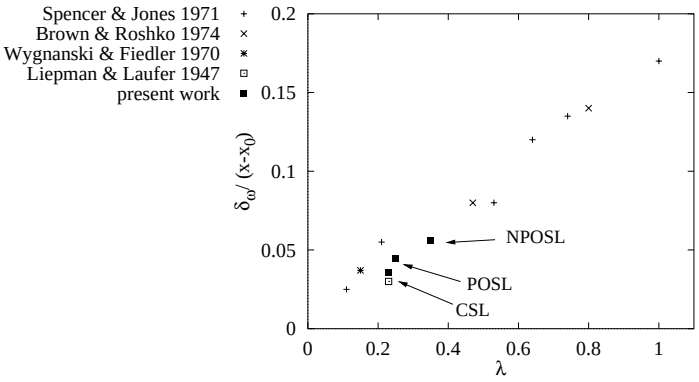

Fig. 4.12: Vorticity thickness dependence on spread parameter

4.2.6 Mean vorticity distributions

Non-dimensionalized vorticity profiles for ω_x and ω_z are represented in fig. 4.13 based on the definitions (3.12). For the non-dimensionalization the term $\delta_\omega/\Delta\overline{U}$ was used which results in values of one for the azimuthal vorticity component ω_z in the center of the shear layer. As expected ω_z has maximum in the center and is zero at the boundaries of the shear layers in all three cases. As ω_z is a function of the gradient $\partial\overline{U}/\partial r$ (or $\partial\overline{U}/\partial y$ in our case), which is similar in the three cases (see the mean velocity profiles in fig. 4.4), the ω_z-distribution is also similar.

The streamwise vorticity component ω_x is practically zero in the CSL . In the NPOSL case, a maximum value of 0.8 was obtained. This means that the streamwise vorticity generated is about of the same order of magnitude as the azimuthal component. The profiles show the formation of a second maximum at the inner side of the shear layer at about $y - y_{0.5}/b$=0.2 with increasing downstream evolution. The $\overline{W}$-profiles discussed earlier showed two different gradients at the two sides which are responsible for the double peak of the streamwise vorticity. This behavior reduces the comparability of the investigated axisymmetric configuration with the corresponding flow in a plane configuration. In the latter case only one peak would occur due to a constant $\partial\overline{W}/\partial y$.

In the co-swirling case, POSL , the vorticity shows also two peaks which probably result on the one hand from the wake characteristic caused by the trailing edge already noticed in the α-profiles, on the other hand, the higher peak on the inner side of the shear layer is affected by the shape of the $\overline{W}$-profiles. A comparison with the $\overline{W}$-profiles shows that a gradient exists in this region which increases with the streamwise evolution.

As was shown earlier the $\overline{W}$-profiles (Fig.)4.4) exhibited two different gradients on either side of the shear layer which are responsible for a double peak in the radial distribution of the streamwise vorticity ω_x. This behavior was more pronounced in the POSL than in the NPOSL . In a plane configuration ω_x would only be created at the interface between the two skewed primary streams. In our axisymmetric case we have a different behaviour although we found exit velocity profiles with only one ω_x-peak. Thus the double peak character can only be attributed to the evolution of the global flow including the shear layer such that the characteristics of the inner jet change. This aspect needs further clarification through measurements in the near field of the shear layer, i.e. in the range of x=0-300 mm.

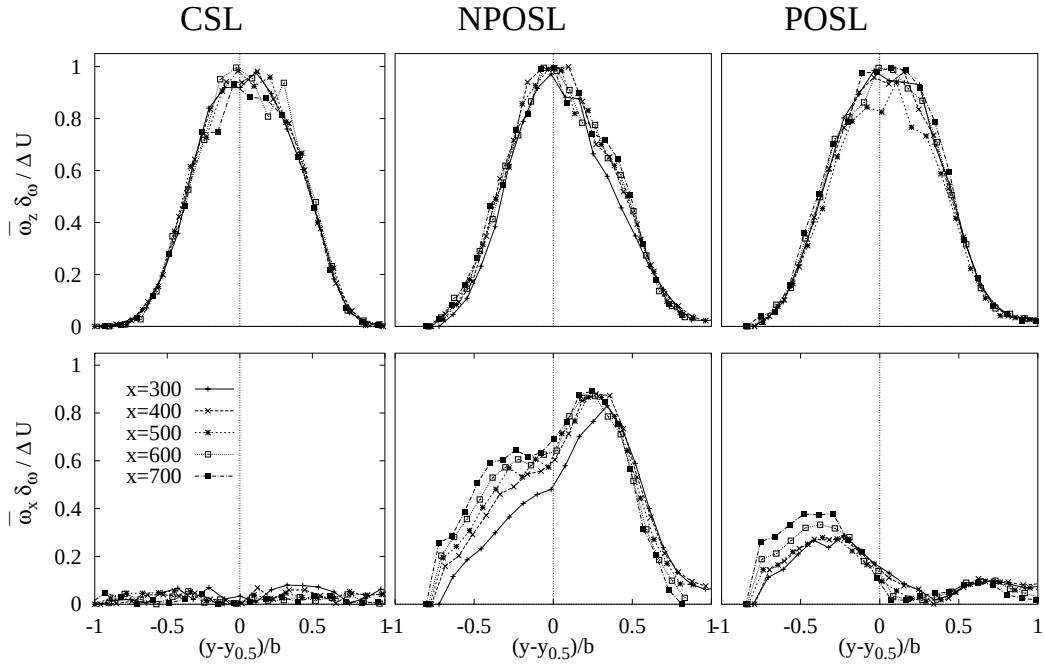

Fig. 4.13: Mean vorticity distributions

4.2.7 Higher order velocity products

Triple velocity correlations

Triple velocity correlations $\overline{u_i' u_j'^2}$ are useful to evaluate the diffusion of mean kinetic energy by the turbulent velocity fluctuations within the shear layer. Moreover, the skewness terms $\overline{u'^3}/\overline{u'^2}^{3/2}$, $\overline{v'^3}/\overline{v'^2}^{3/2}$ and $\overline{w'^3}/\overline{w'^2}^{3/2}$ indicate the preferred transport direction (symmetry of the diffusion process).

In fig. 4.14 correlations of the type $\overline{u' u_j'^2}$ are depicted. These terms describe the flux of u'^2, v'^2 and w'^2 along the *x*-axis. The major qualitative differences between the three cases are that the degree of similarity decreases under the influence of three dimensionality and that the anti-symmetric characteristics is reduced. Further, the absolute magnitudes increase slightly in the cases NPOSL and POSL .

The skewness term $\overline{u'^3}/\overline{u'^2}^{3/2}$ indicates different transport directions in the outer and inner region of the shear layers. All terms are zero at the center-line which means that there is no preferred direction. In the classical configuration the values decrease to zero at the boundary of the shear layer

whereas they are non-zero in the two other cases at the inner boundary ($(y-y_0.5)/b < -0.8$). Obviously, the swirl present in these two cases creates in the central jet an additional axial turbulent transport. The two other terms $\overline{u'v'^2}/\sqrt{\overline{u'^2}\overline{v'^2}}$ and $\overline{u'w'^2}/\sqrt{\overline{u'^2}\overline{w'^2}}$ are almost unaffected by the presence of three dimensionality.

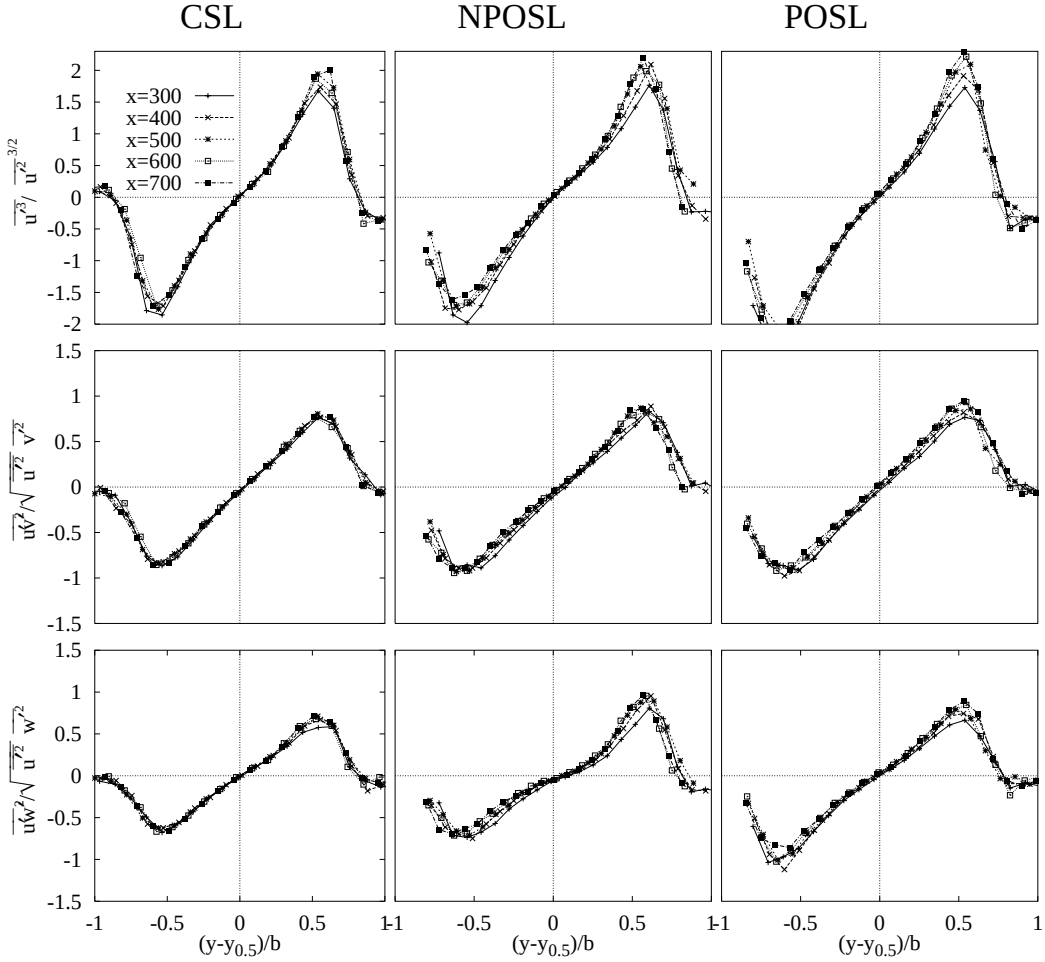

Fig. 4.14: Triple correlations $\overline{u_i' u_j'^2}$

In fig. 4.15 correlations of the type $\overline{v' u_j'^2}$ are represented. These terms describe the radial transport of u'^2, v'^2 and w'^2. The distributions have qualitatively the same shapes as the $\overline{u' u_j'^2}$ correlations. Again, all terms are zero at the center-line and at the two sides of the shear layer opposite transport directions prevail. Hence, turbulent energy is convected away from the center.

Noticeable differences between the shear layer cases become only evident in the absolute magnitudes. The skewness $\overline{v'^3}/\overline{v'^2}^{3/2}$ and the term $\overline{v'w'^2}/\sqrt{\overline{v'^2}\,\overline{w'^2}}$ increase significantly on both sides of the NPOSL . In the POSL these terms increase only in the inner part and remain unchanged in the outer part.

Almost unaffected is the term $\overline{v'u'^2}/\sqrt{\overline{v'^2}\,\overline{u'^2}}$ by the presence of the applied three-dimensional conditions.

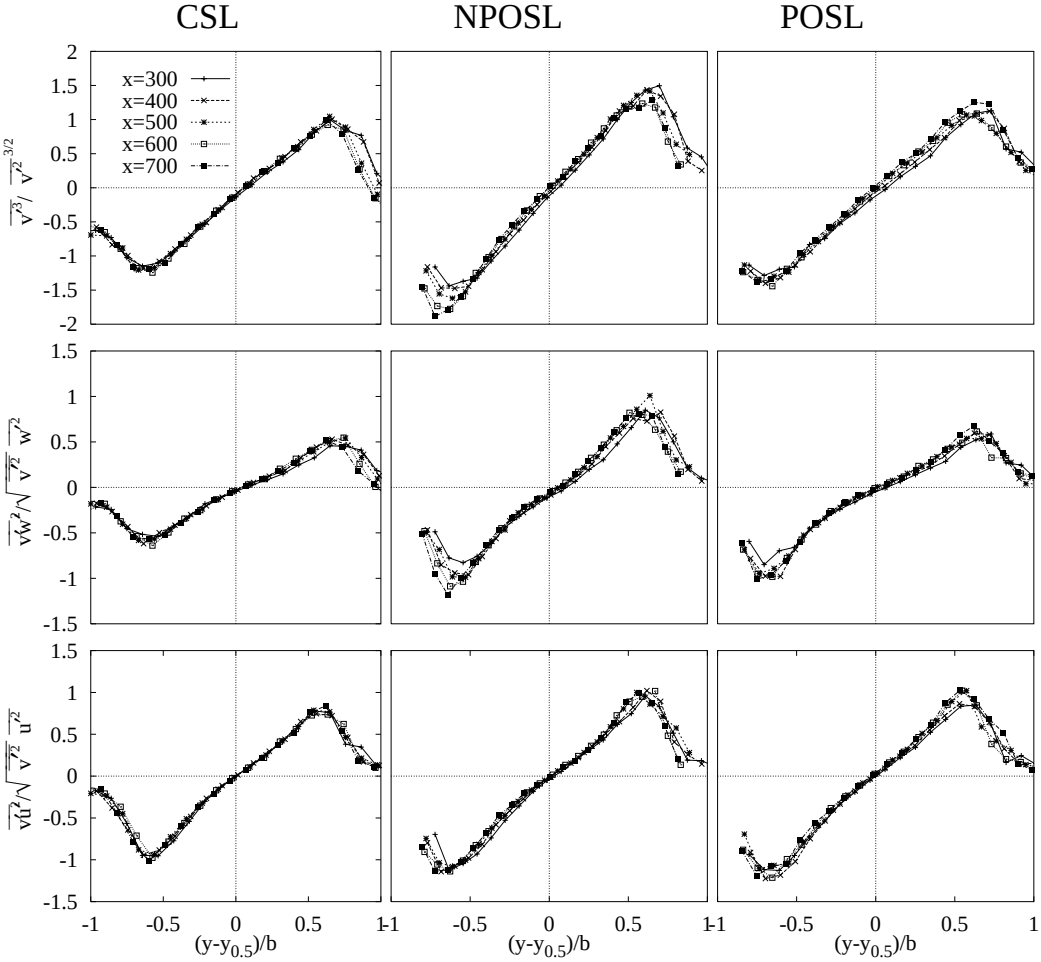

Fig. 4.15: Triple correlations $\overline{v'u_j'^2}$

While the correlations presented so far did not exhibit qualitative differences between the cases studied, drastic differences are found for the terms $\overline{w'u'^2}/\sqrt{\overline{w'^2}\,\overline{u'^2}}$, $\overline{w'v'^2}/\sqrt{\overline{w'^2}\,\overline{v'^2}}$ and $\overline{w'^3}/\overline{w'^2}^{3/2}$ (fig. 4.16). In a nominally

two-dimensional shear layer such as the CSL the transverse transport of turbulent energy be zero since there is no preferred mean transport direction along the *z*-axis. Earlier in this work we found that a small rotational motion of the streams is present in the CSL . This rotation could be responsible for small non-zero values of $\overline{w'u'^2}/\sqrt{\overline{w'^2u'^2}}$, $\overline{w'v'^2}/\sqrt{\overline{w'^2v'^2}}$ and $\overline{w'^3}/\overline{w'^2}^{3/2}$ as can be seen in fig. 4.16. Towards the boundaries these values decrease to zero.

The NPOSL exhibits the largest triple correlation values which occur in the external region of the shear layer. At this location the skewness $\overline{w'^3}/\overline{w'^2}^{3/2}$ is even higher than the skewness of the axial component $\overline{u'^3}/\overline{u'^2}^{3/2}$. The absolute peak value in the inner region is about 40% lower than in the outer region. Thus, the azimuthal flux of turbulent kinetic energy is higher in the external region.The azimuthal transport directions are opposite on the two shear layer sides as are the mean azimuthal flow directions. At the shear layer center all triple correlations are zero. The absolute peak values of $\overline{w'u'^2}/\sqrt{\overline{w'^2u'^2}}$ and $\overline{w'v'^2}/\sqrt{\overline{w'^2v'^2}}$ are about % 50 lower that those of the skewness.

The last triple correlation term presented for the POSL , $\overline{w'v'^2}/\sqrt{\overline{w'^2v'^2}}$, has the same absolute peak values on the two sides of the shear layer which means that.

A distinctive characteristic of the NPOSL compared to the two other cases is, that the $\overline{w'u_j'^2}$-correlations are smaller in the external region than in the inner region. The greatest peak value occurs in the term $\overline{w'u'^2}/\sqrt{\overline{w'^2u'^2}}$.

Flatness and intermittency

The flatness factor is defined as $F = \overline{u_i'^2}^2$ and corresponds to the varianz of the normal stresses. A value of F=3 indicates a Gaussian distribution. The flatness factor has also been associated with the intermittency ([55], [56]). High values are attributed to large sporadic fluctuations which frequently occur at the (intermittent) boundaries of turbulent flow fields.

In fig. 4.17 the flatness factors of all three cases were plotted. The plots show two peaks marking the boundaries of the shear layers. At those positions the

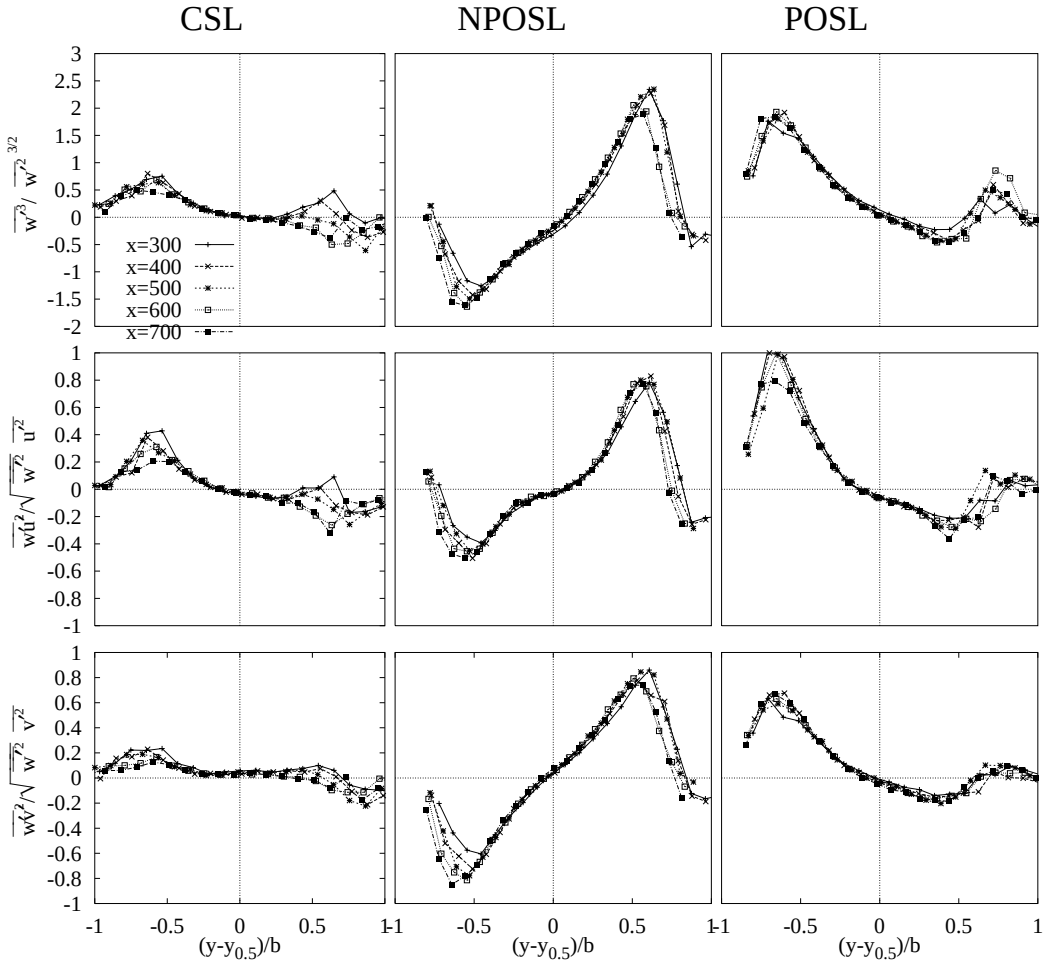

Fig. 4.16: Triple correlations $\overline{w'u_j'^2}$

data scatter as opposed to the shear layer center where a good degree of collapse is achieved and values of about 2.8 to 3.0 are measured. The greatest peak values were measured for $\overline{u'^4}/\overline{u'^2}^2$ of the NPOSL which also has the largest values in the other terms. The POSL peak values range between the NPOSL and CSL . In the shear layers with a mean azimuthal velocity component the flatness factors do not drop to the value of 3.0 at the inner shear layer boundary but remain higher. This behavior indicates a strongly intermittent character due to large-scale motion within the inner turbulent front.

The largest increase compared to the CSL is obtained in the flatness factor $\overline{w'^4}/\overline{w'^2}^2$ of the NPOSL case.

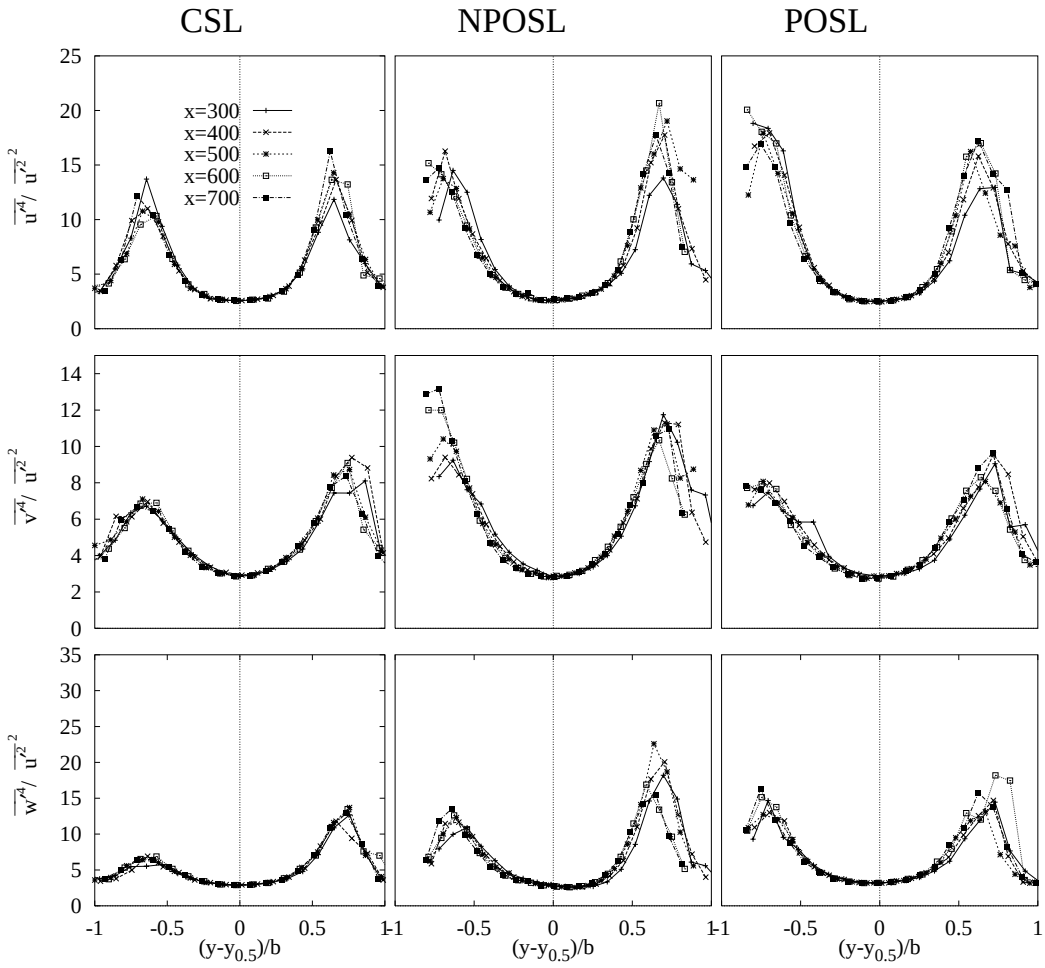

Fig. 4.17: Flatness factor

4.2.8 Energy spectrum

Up to now, we have only considered mean values of fluctuating quantities which gave us an idea of their spatial distribution and the differences between the three cases. Now, we look at the energy distribution of u' in the one dimensional Fourier space $E_{u'} = E_{u'}(f)$ (sometimes the wavenumber $k = 1/f$ is used). In spectra the existence of periodically formed coherent structures which are convected with the mean flow is indicated by the increase of the energy level around a dominating frequency f_d leading to the formation of a broad spike. At high Reynolds numbers local isotropy occurs according to Kolmogorov and the spectrum at high frequencies shows a -5/3 slope (Kolmogorov spectrum).

For the measurement of the spectrum a N-wire of type b) described in section 3.3 was used which allowed high sampling frequencies and spacial resolution (both due to the small wire diameter) necessary for the acquisition of the complete spectrum. At five axial positions (x=300, 400, 500, 600, 700 mm) radial traverses were measured at a sampling frequency of 24 kHz and a sampling time of 22 s. The anemometer signal was low pass filtered at 10 kHz. The resulting spectra for station x=500 mm and 7 different transverse positions are presented in fig. 4.18.

The CSL spectra obtained outside but near the edges of the shear layer (e.g. y= -30, -24 mm) show broad spikes at about f_d= 300 Hz. At positions y= 18, 24, 30 mm (not shown here) the same spikes were found. The resulting Strouhal number (eqn. 2.8) St_{δ_ω}=0.336 is in good agreement with data found in the literature. Thus, it can be assumed that the vortex rings observed in the visualizations of section 4.1 at much lower Reynolds numbers are also the dominating structures in this case. Their so-called 'foot prints' become evident in the spectra. Together with the f_d values of the spectra at the other axial stations (not shown here) a linear evolution of $f_d \propto x$ was derived.

At the shear layer center where the maximum turbulent energy is produced the Kolmogorov slope of -5/3 is valid so that the assumption of local isotropy is satisfied. The flow is thus fully developed which confirms the self similarity found in the previous sections.

At very low frequencies ($<$30 Hz) an increase of turbulent energy is visible which is not a typical behavior in plane configurations. Various checks made clear that this is not a wind tunnel effect (acoustic resonance, vibrations). It is presumed that the residual rotational motion of the jets contribute to this energy increase.

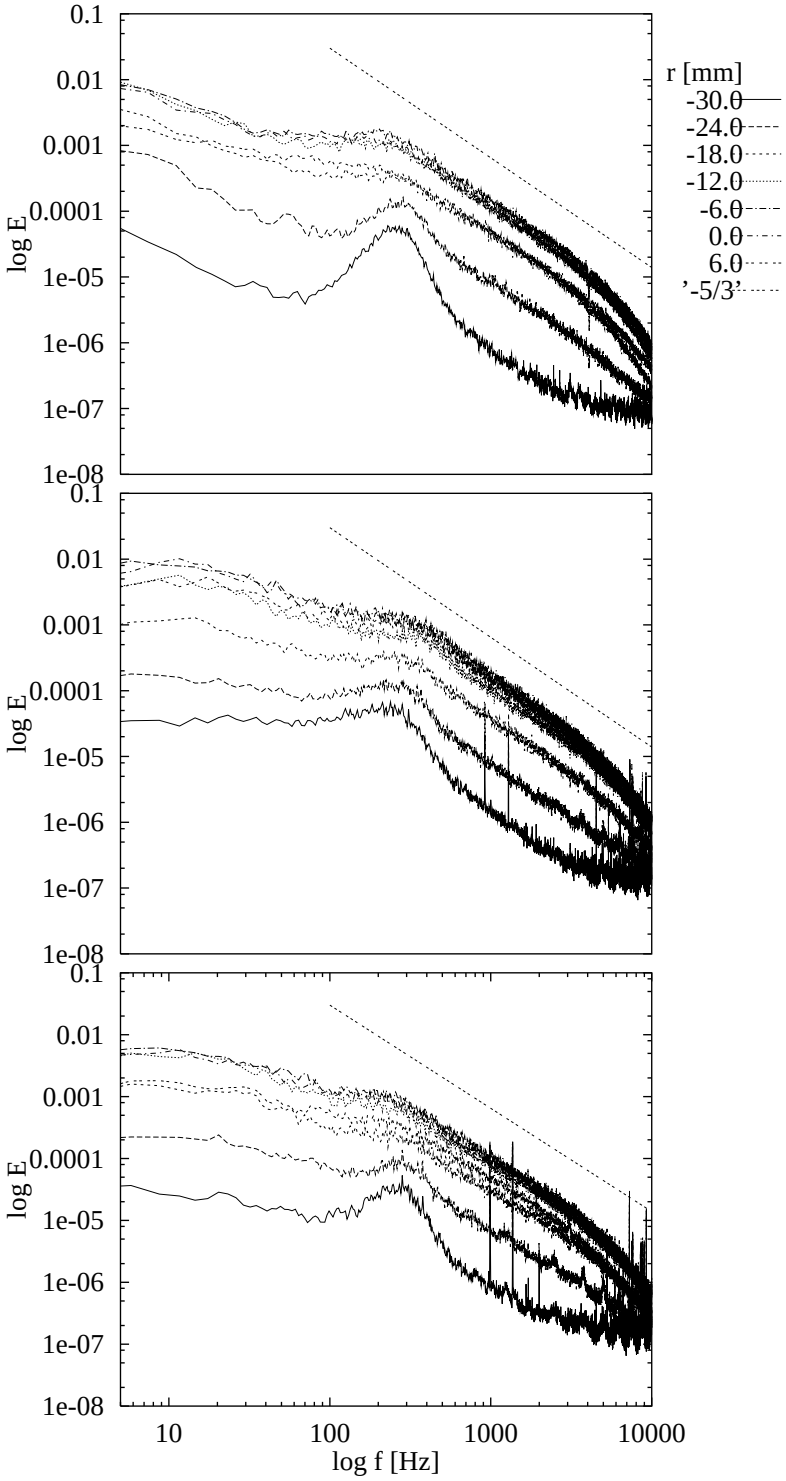

Fig. 4.18: Spectra at x=500 mm; top: CSL ; middle: NPOSL ; bottom: POSL (the dashed line corresponds to the -5/3-slope)

In the spectra of the NPOSL the identification of a typical frequency is difficult as the spikes are embedded in an overall increased energy level. However, at *y*=-30 mm a flat spike is visible at f_d=300 Hz. In the range between this frequency and 15 Hz a plateau has formed where we found a dip in the CSL . Apparently, the NPOSL with its counter rotating jets generates an increased band width of structural activity at lower frequencies. The streamwise evolution of f_d is linear. At the center of the shear layer the increased energy level which we observed in the Reynolds stress profiles in section 4.2.1 is recognizable (the -5/3 slope is at the same position in the three plots so that spectra with higher energy levels are closer to that line). The Kolmogorov spectrum $E(f) \propto -5/3$ is also existent in this case.

The results of the NPOSL allow the assumption that the structural behavior corresponds to that of a classical plane shear layer but with additional effects which need further examination. We will see later that these effects result from a higher structural activity.

The spectra of the POSL case show characteristics which resemble an intermediate case of the CSL and the NPOSL . Again we identify a dominant frequency at f_d=300 Hz and a Kolmogorov spectrum. The low frequency spectrum between 15 Hz and 300 Hz is elevated compared to CSL but less than in the NPOSL case. From this observation we can conclude that the higher level in the NPOSL is an effect of the counter rotation of the jets and not of the rotation as such. It should be noted that the spectra considered are only one-dimensional and that structures which are not aligned with *z* lead to aliasing effects.

4.2.9 Further discussion

The behavior of the CSL described in the previous section is consistent with that of plane shear layer configurations. The maximum Reynolds stress values (see tab. 4.2), the growth rates (see tab. 4.2.5) and the structural organization (e.g. primary structures) are in good agreement with the data given in the literature although we found small rotational motion in the inner jet. Also the relations between the normal stresses are typical $\overline{u'^2} > \overline{w'^2} > \overline{v'^2}$.The constant Reynolds stress levels downstream of *x*=400 mm and the collapse of their normalized profiles indicate self-similarity.

When subjected to three-dimensional conditions, i.e. non-parallel primary streams, strong changes take place which - at least to some extent - were

expected. In the NPOSL the two primary streams are skewed so that cross-shear is introduced. In the Reynolds stress transport equations 2.9-2.14 the term representing the cross-shear is $\frac{\partial \overline{W}}{\partial r}$. The terms directly affected by the extra strain $\overline{W}/r$ are $\overline{w'^2}$ and $\overline{v'w'}$. The results show that these two stresses increase most in the NPOSL . The normal stress $\overline{v'^2}$ increases also followed by $\overline{u'^2}$. Eqn. 2.10 predicts an increase of $\overline{v'^2}$ through the term $\overline{v'w'}\ \frac{\overline{W}}{r}$ which is an additional production term due to the transformation of Cartesian to cylindrical coordinates. The term $\frac{\overline{W}}{r}$ can be interpreted as an extra strain due to the motion along a curved line. However, the gain of $\overline{v'^2}$ in the NPOSL cannot be completely attributed to this curvature effect. The POSL which contains the same curvature but much less additional cross-shear did not exhibit such an increase. The major part of the increase of $\overline{v'^2}$ must therefore be a result of increased structural dynamics (higher order mechanisms) due to the imposed three-dimensionality. The same explanation holds for the growth of $\overline{u'^2}$.

The equations for the shear stress transport 2.12-2.14 indicate an increase of all three components when terms containing $\frac{\overline{W}}{r}$ and $\frac{\partial \overline{W}}{\partial r}$ are activated. According to these equations the greatest contribution should be expected for $\overline{v'w'}$ because it is affected by from both terms. $\overline{u'w'}$ gains from the activation of the dominant gradient $\frac{\partial \overline{U}}{\partial r}$ through the generation of $\overline{v'w'}$. Also the curvature term $\frac{\overline{W}}{r}$ which is multiplied by the large shear stress $\overline{u'v'}$ is supposed to contribute to an increase of $\overline{u'w'}$. As $|\overline{v'w'}| < \overline{v'^2}$ and $\frac{\overline{W}}{r} < \frac{\partial \overline{W}}{\partial r}$ the increase of $\overline{u'v'}$ should be smaller than for $\overline{u'w'}$. This behavior is consistent with the presented results for the NPOSL . In the POSL the situation is not that clear. Here, $\overline{u'w'}$ has increased more than $\overline{v'w'}$ and both have a negative sign. According to eqn. 2.14 a negative sign for $\overline{v'w'}$ is a consequence of a positive $\frac{\partial \overline{W}}{\partial r}$ gradient which indeed is shown in fig. 4.8. The locations of the maximum values for $\overline{v'w'}$ and $\frac{\partial \overline{W}}{\partial r}$ occur at the same transversal positions. The negative sign for $\overline{u'w'}$ can be explained by the combination of the negative $\overline{v'w'}$ and the negative gradient of $\frac{\partial \overline{U}}{\partial r}$. These considerations show that the term $\frac{\overline{W}}{r}$ plays only a small role compared to even small azimuthal gradients because the $\overline{v'w'}$ and $\overline{u'w'}$ profiles show a stronger dependency on $\frac{\partial \overline{W}}{\partial r}$ than on $\frac{\overline{W}}{r}$.

4.3 Structural description based on multi point measurements

4.3.1 Pseudo Flow visualizations

As mentioned earlier, flow visualization with smoke is one of the basic tools of flow structure identification in air flows. However, at high flow speeds smoke visualizations is not satisfactory. In such cases Pseudo Flow visualizations (PFV) can be an alternative. This method requires the simultaneous measurement of the velocity at several points in the flow field. PFV is also an economic way to study quantitatively the large amount of data from multi sensor measurements. Some examples can be found in [57].

Supposing that ξ is the direction in which the hot-wire rake is aligned, then the most simple way to obtain a PFV is to take the instantaneous velocity signals of the hot wire rake $U(\xi,t)$ or their fluctuating part $\overline{u'^2}(\xi,t)$ and to classify them into n classes (i.e. velocity increments). Then each class is allocated to a different color according to a color rule or a look-up table. With the aid of image processing tools these colorized traces are assembled to a single two-dimensional image.

In this study PFV is performed in two directions : in the transversal and in the azimuthal direction. The transversal PFV provides information on the existence and/or modification of vortical structures already observed in the smoke visualizations. The azimuthal PFV will help to determine their orientation (parallel to the trailing edge or slanted).

Transversal direction

To obtain a data basis for the PFV a hot-wire rake with 23 N-hot wires of type c) (see tab.3.1 for details) was used. The rake was designed and built in CEAT and a detailed description is given in [58]. The probe separation is 3 mm and the wires were oriented parallel to the radial direction. The 23 signals were sampled simultaneously at 5000 Hz. 10 records each consisting of 20480 samples were obtained. The effective velocity measured is here $\underline{U_{eff}} = \underline{U} + \underline{W}$. Grey scales are used for the look up table with a linear distribution. High velocities correspond to bright scales and low velocities to dark scales. The time sequences of the PFV's shown in the following figures are equal to $t = 0.0128$ s. The axial position was x=500 mm. The images have not been treated with any smoothing or other algorithms so that

they consist of rather large pixels. The flow direction is from left to right. Each pixel row represents the time trace of a individual sensor.

In fig. 4.19 two PFV for the CSL case are shown. The upper PFV is obtained from the velocity U_{eff} and the lower from the fluctuating part $u\prime_{eff}$. Both images show 4 regularly spaced structures which we identify as the cross-section of vortex rings. The structures are connected with a thin, inclined sheet which represents the braid region. The frequency calculated from the number of structures and the sampling frequency f_s is 312 Hz which is close to f_d found in the energy spectra (section 4.2.8).

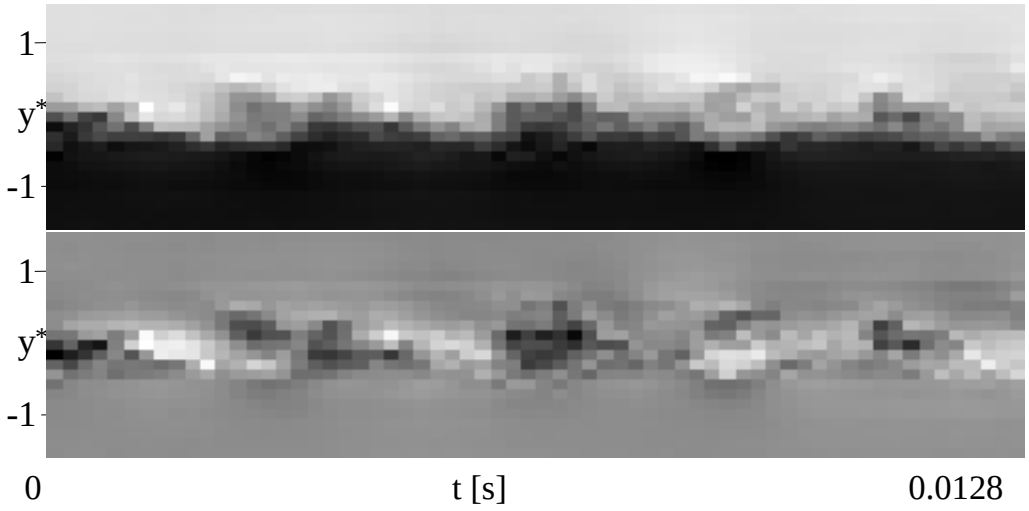

Fig. 4.19: PFV of the CSL , upper image: U_{eff}; lower image :$u\prime_{eff}$

The PFV's of the NPOSL and of the POSL are shown in figs. 4.20 and 4.21. In these cases also the passage of structures is visible but less pronounced as in the CSL . The structures have larger diameters which is in agreement with the results of section 4.2.5. Their spacing and size are less regular and the space between them cannot be identified as a braid region.

As with smoke visualization the interpretation of PFV is also dependent on the observer and visualized structures do not necessarily satisfy the definition of coherent structures. However, in combination with previous experimental results useful information can be extracted. In the only two-dimensional views of the above pfv's the effect of three-dimensionality can be summarized as a perturbation of the shape and regularity of the primary coherent structures which originally stem from the Kelvin-Helmholtz instability of the shear layer.

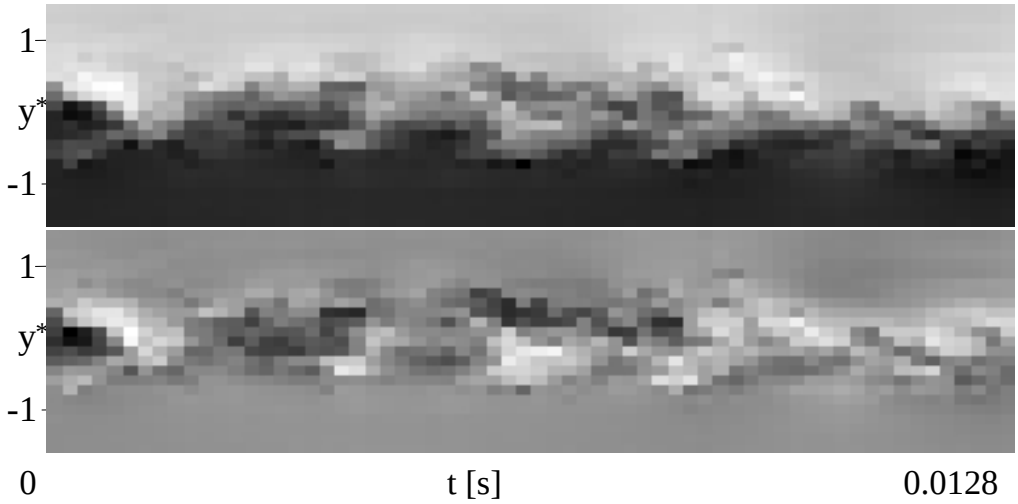

Fig. 4.20: PFV of the NPOSL , upper image: U_{eff}; lower image :$u\prime_{eff}$

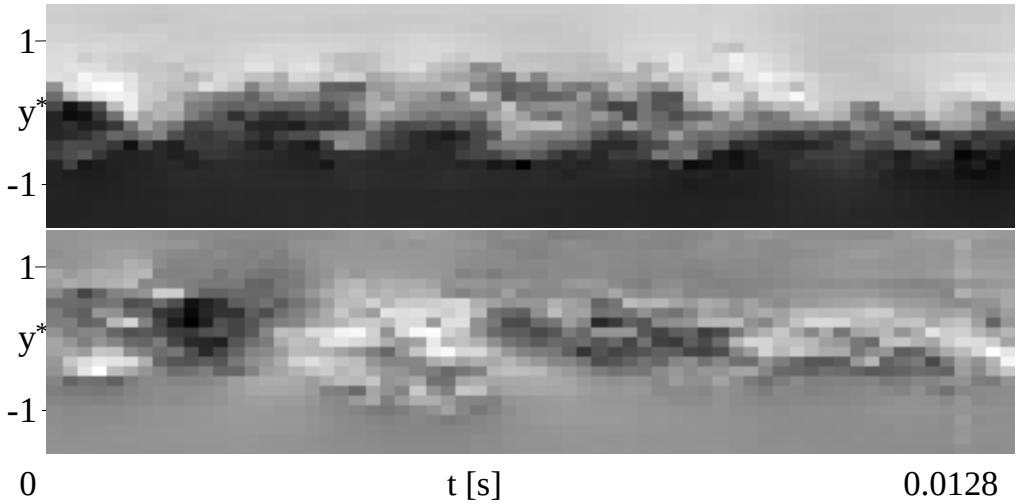

Fig. 4.21: PFV of the POSL , upper image: U_{eff}; lower image :$u\prime_{eff}$

PFV in the azimuthal direction

For this measurement curved rakes (fig. 4.22) oriented parallel to the azimuthal direction with 15 N-wire probes of type a) are used. Three rakes with different radii were employed so that measurements at three radial positions y= -20, 20 mm and 0 were carried out. These locations correspond to the lower edge, upper edge and the center, respectively, of the shear layers studied. The axial position was x=500 mm. The sensor orientation was the radial direction. Thus, the velocity measured corresponds to the magnitude of the vector $\underline{U_{eff}} = \underline{U} + \underline{W}$. The azimuthal distance between the individual sensors was $\overline{15}$ mm. Hence, the measured fraction of the trailing edge circumference (=0.754 mm) is $15 * 15$ mm =225 mm. The data was sampled at a frequency of 2000 Hz. For each case studied two additional data sets were considered besides the original set: Filtering was applied to the original data set in order to separate the structural organization at frequencies near the dominant Strouhal number from that part of the energy spectrum at very low frequencies ($<$50 Hz). In the latter an increased energy level was reported in section 4.2.8 and it is expected that the filtering will give some clue to its origin. The data was low-pass filtered with an analog circuit at 820 Hz during the acquisition. Afterwards a digital low-pass filter at 50 Hz and a digital band-pass filter at 50-820 Hz were applied.

The following samples correspond to a time span of 0.256 s obtained at the outer edge of the shear layers, i.e. in the low speed side. The fluctuating part of the velocity signals are used - u'_{eff}- to construct the PFV. The range of the u'_{eff}-values was projected onto the digits 0 to 256 which was then used for the color rule. The color rule used in this case is shown in fig 4.23. It allocates high velocity values to warm colors (red) and low velocity values to cold colors (blue).

The PFV of the CSL based on the non-filtered data is shown in fig. 4.24(a). It shows somewhat regularly spaced structures among some of them have their axes parallel to the rake. Most of the structures do not have straight axes but are tilted. This pattern corresponds to the so called ”footprints” of the vortex rings already encountered in the transversal PFV. After low-pass filtering at 0-50 Hz the image in fig. 4.24(b) is obtained. In this spectral range also structures are visible but less numerous and orderly. Their existence was already indicated in the spectra and their origin is not clear. In the band-passed filtered data (fig. 4.24c) only negligible differences are visible compared to the unfiltered data.

Fig. 4.22: Hot-wire rake

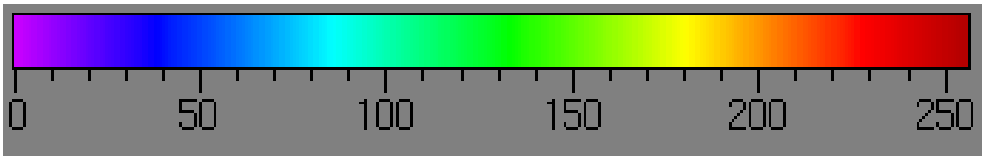

Fig. 4.23: color rule for the azimuthal PFV's and cross correlations

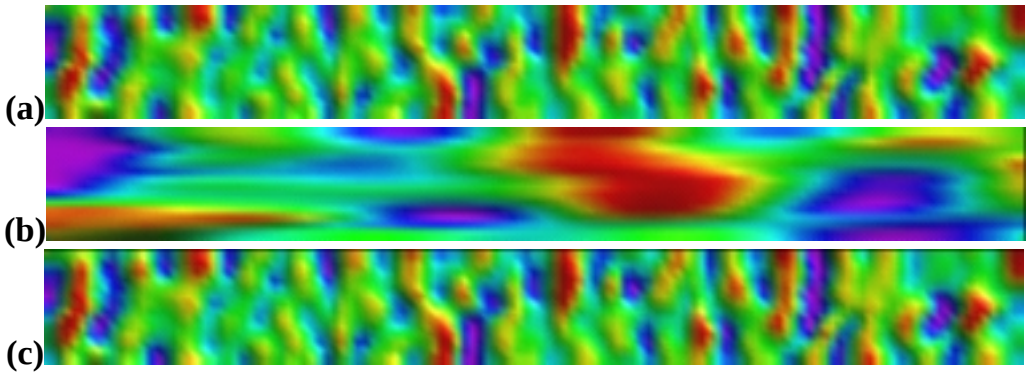

Fig. 4.24: PFV of the CSL , (a) no filter, (b) filtered at 0-50 Hz, (c) filtered at 50-820 Hz

The PFV's of the two other cases (NPOSL : fig. 4.25; POSL : fig. 4.25) do not show any obvious differences. Only compared to the CSL a difference in the azimuthal coherence of the presumed vortex ring structures is recognizable. Also, their regularity in the streamwise direction is reduced. This tendency is more pronounced in the NPOSL than in the POSL .

Since the azimuthal PFV's did not provide a clear picture of the structural organization of the flows at lower frequencies (< 50 Hz), the data were further analyzed. Therefore, the cross correlations will be presented in the next section.

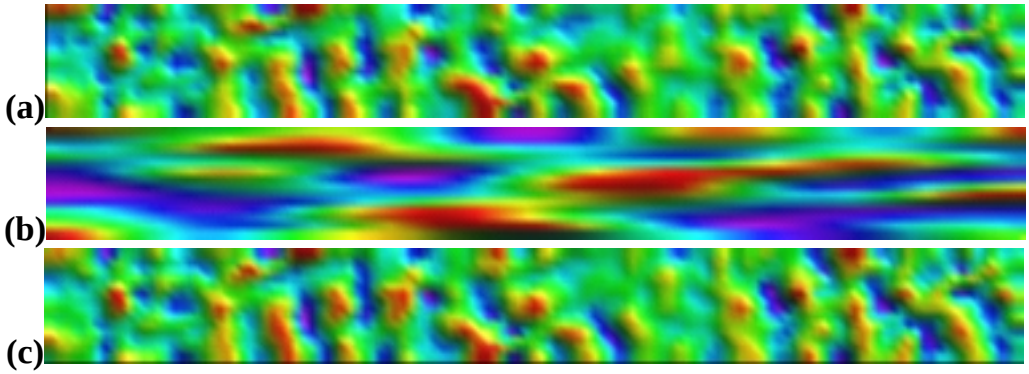

Fig. 4.25: PFV of the NPOSL , (a) no filter, (b) filtered at 0-50 Hz, (c) filtered at 50-820 Hz

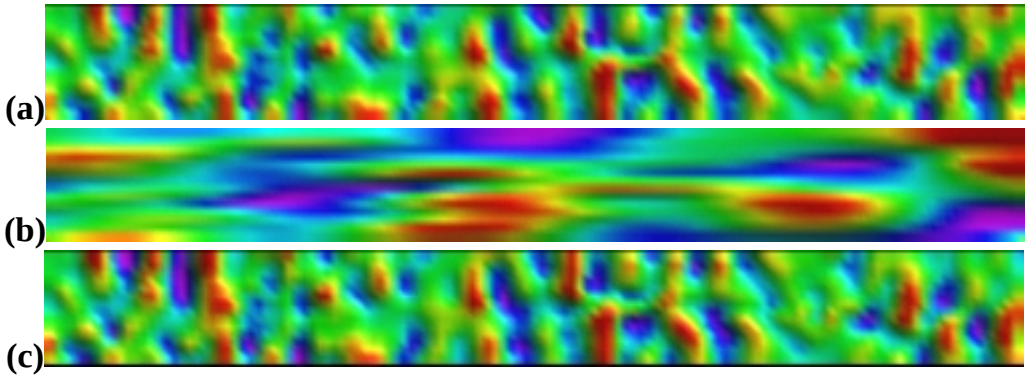

Fig. 4.26: PFV of the POSL , (a) no filter, (b) filtered at 0-50 Hz, (c) filtered at 50-820 Hz

4.3.2 Space-time correlations

Transversal direction

In the transversal PFV's the impression was created that the degree of regularity in shape and spacing of the primary structures (vortex rings) in the two-dimensional shear layer is reduced when subjected to three-dimensional conditions. The effect seemed to be more intense in the NPOSL than in the POSL . With the help of the transversal space-time correlations we want to obtain additional information in order to verify the observations from the PFV. The data used is the same as for the PFV, i.e. 23 N-wires placed on a rake parallel to the y-axis with simultaneous signal acquisition and x=500 mm. The correlation coefficient is then calculated as:

$$R_{u'u'}(\Delta y,\tau) = \frac{\overline{u'(t,y)u'(t+\Delta t,y+\Delta y)}}{\sqrt{\overline{u'^2}}\sqrt{\overline{u'^2}}} \tag{4.1}$$

The result is shown as iso-contours in fig. 4.27. A reference signal probe # 12 was used which is located near the shear layer center-lines. Delville [59] found that this position gave the best results. It should be noted that the choice of the iso-contours levels plays an important role for the qualitative appearance of the plots. Furthermore, the identification of structures on the basis of the transverse cross-correlations of the u'-signal has proved to be somewhat difficult in the turbulent region. Better results were obtained at the edges of shear layer ("foot-prints").

The iso-contours of the CSL show three rows, each having three or four correlation "spots". The locations of the upper and lower rows correspond to the upper and lower edge of the shear layer. There the correlation coefficient changes sign from positive to negative. This is due to the different predominant u'-directions on either side of the shear layer caused by the induction of the large structures. Thus, the spots outside the shear layer are in fact traces of structures. Three of them appear within Δt=0.01 s corresponding to a frequency in the neighborhood of 300 Hz.

In the NPOSL only one broad spot on the center-line with its corresponding spots at the shear layer edges can be seen. This suggests that the correlation used is not well suited for the identification of the structures which were indicated in the spectra and PFV of the NPOSL due to the the high turbulence level.

The picture is somewhat better in the POSL . There we can see a situation similar to the CSL . In the vicinity of the shear layer traces of the structures are visible in form of regularly spaced spots. In the center only a single broad spot is visible so that from this location no clue of the existence of structures is found.

The above results show that the transversal cross correlations based on the u'-signal are affected by the increased turbulence level which makes it harder to identify structures in particular in the NPOSL . It is believed that a correlation based on v' would provide better results as no change of signs takes place across the shear layer.

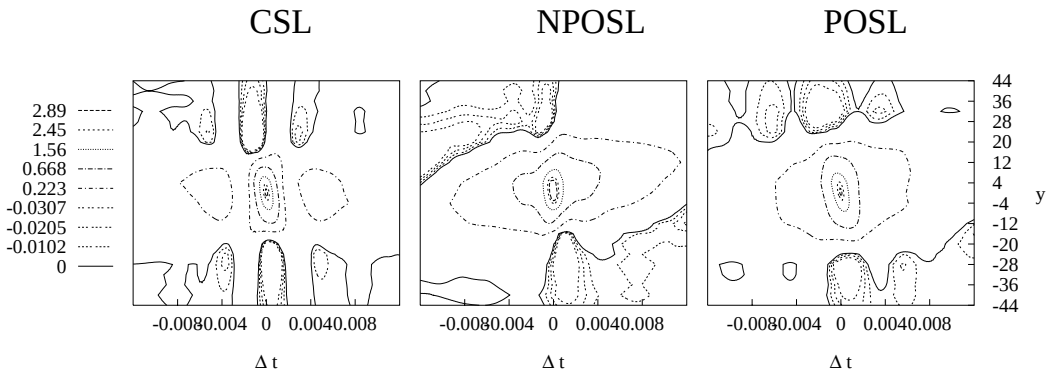

Fig. 4.27: Transversal space-time correlations, $R_{u'u'}(\Delta y, \tau)$

Lateral direction

Finally, we investigated the lateral coherence of the structures and their orientation. From the data set used for the azimuthal PFV, i.e. simultaneously sampled axial velocity signals of 15 sensors, the correlations coefficient

$$R_{u'u'}(\Delta z, \tau) = \frac{\overline{u'(t,z)u'(t+\Delta t, z+\Delta z)}}{\sqrt{\overline{u'^2}}\sqrt{\overline{u'^2}}} \tag{4.2}$$

was calculated. For the economic presentation of the obtained data a method similar to the previous PFV was chosen. The values of the correlation coefficients where projected onto a color rule and a two-dimensional image was assembled with Δt and Δz being the two-dimensions. Furthermore, a three dimensional effect was obtained by adding an amplitude to the surface proportional to the correlation value. The color rule used is the same as for the

PFV (fig. 4.23). The lowest $R_{u'u'}(\Delta z, \tau)$=-1 corresponds to the digit 0 and the highest $R_{u'u'}(\Delta z, \tau)$=1 to the digits 256. With the aid of image processing software light and shadow effects were also created and the surface was smoothed as can been seen in the images below. As for the PFV, two filtered data set were used besides the original one. Low pass filtering at 0-50 Hz and a band pass filtering at 50-820 Hz were carried out.

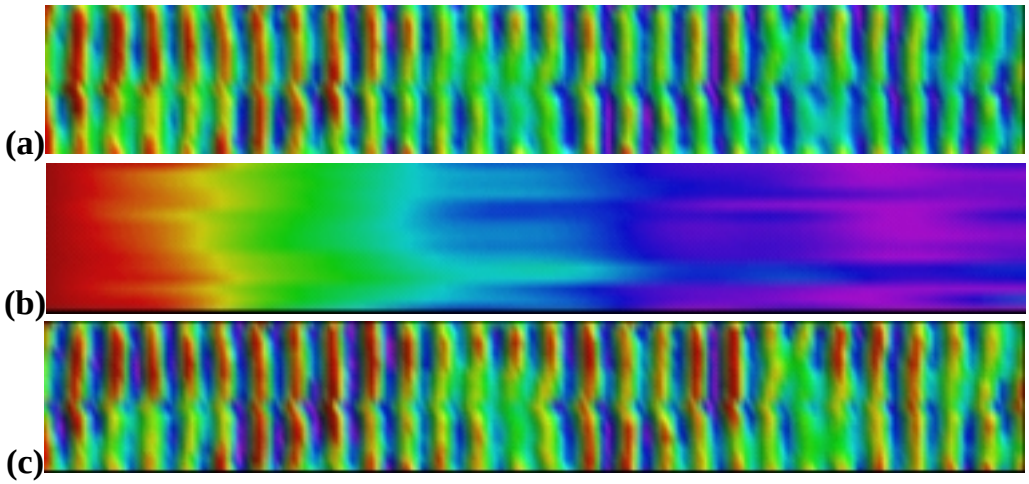

Fig. 4.28: Visualization of $R_{u'u'}(\Delta z, \tau)$, CSL , (a) no filter, (b) filtered at 0-50 Hz, (c) filtered at 50-820 Hz; Δt_{max}= 0.1 s

Fig. 4.28 displays the visualization of the correlation coefficient of the classical shear layer for a maximal time delay of Δt_{max}=0.1 s. Δt is the horizontal dimension. The vertical dimension represents 15 Δz values corresponding to the probe spacing on the hot-wire rake. Thus, Δz ranges from 0 (autocorrelation of probe #1) to 225 mm (cross correlation between probe #1 and #15). The image from the unfiltered data set reveals excellently the passage of the two dimensional vortex ring structures which create regular color changes parallel to the rake, i.e. to the trailing edge. In the PFV these structures were much less regular and straight. This is because in the PFV only instantaneous situations are depicted while from the cross correlations a picture based on averaging is retrieved. Dividing the number of structures by Δt_{max}=0.1 s gives a frequency of 300 Hz - the same found in the spectra at the same axial position. The low-pass filtered data set shows no traces of structures. In the image from the band passed filtered data the presence of the above structures is somewhat clearer.

In fig. 4.29 the original data set of the NPOSL also exhibits the existence

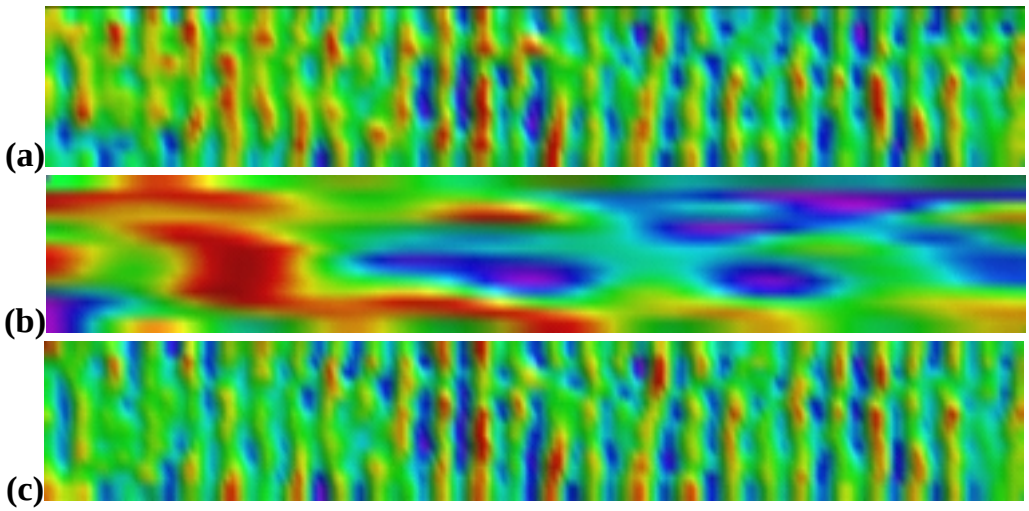

Fig. 4.29: Visualization of $R_{u'u'}(\Delta z, \tau)$, NPOSL , (a) no filter, (b) filtered at 0-50 Hz, (c) filtered at50-820 Hz; Δt_{max}= 0.1 s

of structures parallel to the rake with a frequency of 300 Hz. However, in this case they appear perturbed in the lateral direction and therefore less two dimensional. When low pass filtered at 50 Hz few oblique phenomena become visible which were not found in the CSL . In the third image (filtered between 50 and 820 Hz) where the parallel structures are extracted from the original data displaying the data, it can be seen that structure axis are less straight and sometimes even tilted.

The $R_{u'u'}$-visualizations of the the POSL in fig. 4.30 reveal the same parallel structures at 300 Hz as in the above two cases. Their formation is more regular and more two dimensional than in the NPOSL but less as in the CSL . In the low pass filtered image some non-parallel phenomena are exhibited.

To examine more closely the non-parallel phenomena in the two last cases, visualizations for a longer time delay Δt_{max}=0.85 s were made (fig. 4.31). There it can be seen that the NPOSL and the POSL indeed contain more or less regularly spaced structures oblique to the trailing edge. In the NPOSL case about 5 to 6 and in the POSL 2 such structures can be identified. These structures are responsible for the reduced two-dimensionality of the vortex rings (i.e. their deviation from a ring shape). In the NPOSL the perturbation is higher due to the higher number of oblique structures. The origin of the oblique structures can be attributed to the three dimensional conditions of the flows.

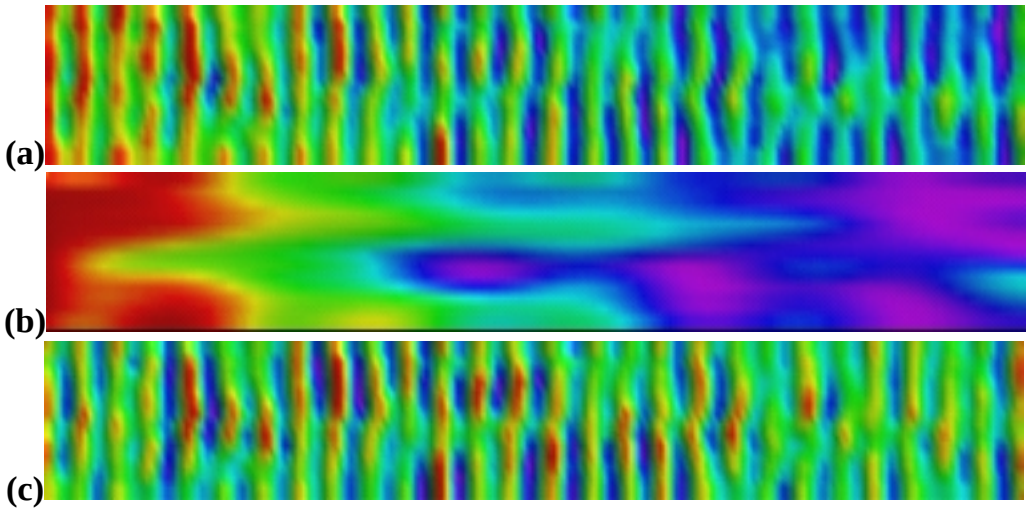

Fig. 4.30: Visualization of $R_{u'u'}(\Delta z, \tau)$, POSL , (a) no filter, (b) filtered at 0-50 Hz, (c) filtered at50-820 Hz; Δt_{max}= 0.1 s

Here is an attempt of an explanation: In the NPOSL besides the primary shear layer with the gradient $\partial\overline{U}/\partial y$ a secondary - superpositioned - one with a gradient $\partial\overline{W}/\partial y$ is created. The primary shear layer generates vortex rings with the vorticity component ω_z and the secondary streamwise vortices with the vorticity component ω_x. The latter are skewed by the helical convection velocity so that oblique structures are formed. In fig. 4.13 the maximal streamwise vorticity - thus the streamwise vortex - is located at $y - y_{0.5}/b$=0.3, i.e. in the outer jet. At that location the flow angle is α=-8° (fig. 4.5) which represents the convection direction of the streamwise vortices. This direction is the same as the direction of the structures visible in the correlation images.

In the POSL a small amount of streamwise vorticity is generated as well as was shown in fig. 4.13. As explained above, the resulting streamwise structure is then skewed in the direction of the mean convection (flow angle). From the plot in fig. 4.5 the flow angle in the POSL can be retrieved as about α=-10° which is the same direction as in the correlation images.

4.3.3 Proper Orthogonal Decomposition

POD is a method which was suggested by Lumley in 1967 [60] and which can be used to identify preferred modes in turbulent flows. These modes

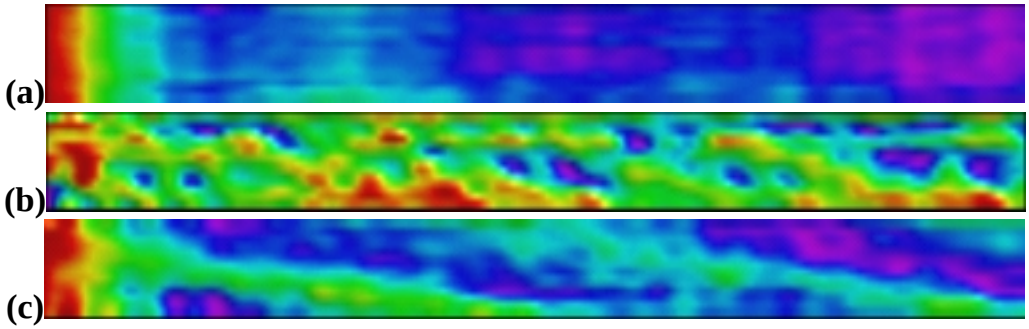

Fig. 4.31: Visualization of $R_{u'u'}(\Delta z, \tau)$ filtered at 0-50 Hz, Δt_{max}= 0.85 s, (a): CSL ; (b):NPOSL ; (c):POSL

correspond to flow patterns or coherent structures which are independent of each other. Advantages of this method are its objectivity, because no apriori knowledge of the structure is necessary, and its lack of bias. POD is also optimal in the sense that for a given number of modes, no other decomposition captures as much energy. A disadvantage of this method is the necessity of the knowledge of the two-point correlation tensor over a large number of points so that multi-probe measurements are required.

In order to find the modes a candidate structure is projected on the ensemble of the flow field realizations. That candidate structure which has the largest mean square projection is then a preferred mode or coherent structure. Mathematically the method involves maximizing the mean square energy through the calculus of variations leading to the Fredholm integral equation of the first kind:

$$\int R_{ij}(\underline{x},\underline{x}')\Phi_j(\underline{x}')d\underline{x}' = \lambda\Phi_i(\underline{x})$$

The symmetric kernel in this eigenvalue problem is the two-point correlation tensor

$$R_{ij}(\underline{x},\underline{x}') = \overline{u_i(\underline{x})u_j(\underline{x}')}$$

. The candidate structure is denoted by $\underline{\Phi}$, $\underline{x}$ and $\underline{x}'$ ans represents different spatial points and times. The solution of the above equation is described by the Hilbert-Schmidt theory which requires an energy integrable velocity field. In cases where the velocity field has a homogeneous or periodic direction or is stationary in time the problem reduces to a harmonic orthogonal decomposition (Fourier modes). The theory also states that the solution of

the Fredholm integral of the first kind for a symmetric kernel is a discrete set so that

$$\int R_{ij}(\underline{x},\underline{x}')\Phi_j^{(n)}(\underline{x}')d\underline{x}' = \lambda^{(n)}\Phi_i^{(n)}(\underline{x})$$

The set of eigen-functions are orthonormal:

$$\int \Phi_i^{(p)}(\underline{x})\Phi_i^{(q)}(\underline{x}) = \delta_{qp}$$

The fluctuating velocity field can be reconstructed from the eigen-functions:

$$u_i(\underline{x}) = \sum_{n=1}^{\infty} a^{(n)}\Phi_i^{(n)}(\underline{x})$$

where the random coefficients $a^{(n)}$ are obtained from (projection of u_i on Φ_i)

$$a^{(n)} = \int u_i(\underline{x})\Phi_i^{(n)}(\underline{x})d\underline{x}$$

The turbulent kinetic energy is the sum over n eigenvalues λ_n. Each mode or structure contributes its part the kinetic energy and Reynolds stress. The eigenvalues are real, positive, their sum is finite and their series converges $\lambda^{(1)} > \lambda^{(2)} > \lambda^{(3)}, \cdots$.

When only one velocity components is considered the POD is called scalar POD. When two ore more components are taken into account the POD is called vectorial POD.

General introductions and surveys on the POD are given in [59, 61]. Some interesting applications of the POD to turbulent shear flows can be found in [62, 63] and references therein.

In the present work the scalar POD is applied to the inhomogeneous direction, y, of the shear layer. The data used is the same as for the lateral PFV and the correlations. The applied POD is only two-dimensional and will not provide any information on the three-dimensional character of the modes but is rather expected to assess the applicability to the flows investigated.

Convergence of the eigenvalues

Here we want to compare how the convergence of the POD decomposition differs for the three flow cases . According to Delville [59] the convergence of the POD can be defined as the ratio between the turbulent energy content of the first *n* modes and the total energy:

$$\sum_{i=1}^{n} E^{(i)}/E \quad \text{, where}$$

$$E^{(i)} = \int_0^\infty \lambda^{(i)}(f)df \quad \text{and} \quad E = \sum_{i=1}^{N} E^{(i)}$$

Fig. 4.32 exhibits a monotonic convergence for all three cases. In the classical shear layer case convergence is somewhat faster. The first mode of the CSL captures about 60 % of the total energy. About 88 % of the total energy are contained in the three first modes. In the plane shear layer investigation by Delville [59] 79 % of energy the total were captured. It is surprising that the curves of the POSL and the NPOSL collapse. In these cases the first three modes contain 75 % of E.

These results show hat the shear layer cases studied can be very well represented by few POD-modes. This is a further verification of the existence of dominating structures observed in the previous sections.

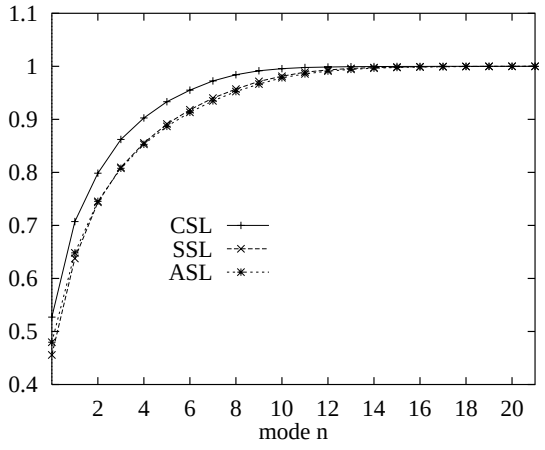

Fig. 4.32: Convergence of the eigenvalues

The shape of the eigenvectors

In fig. 4.33 the eigenvectors $\Phi_i^{(n)}$ are shown. As the POD is based on the energy content of presumed structures the first modes of the three cases considered have distributions equal to their turbulent kinetic energy, i.e. the maximum is in the shear layer center. The number of extrema and zero-crossings increases with the mode number considered. The first mode is symmetric, the second is antisymmetric , the third is symmetric again and so on. This indicates that the higher the mode numbers the more the form of the eigenvectors assumes the character of a harmonic decomposition. These properties are typical of a POD in shear layers [54] and indicate that the higher modes of the POD divide the energy containing domain of the large scale structures (=mode 1) into subdomains with their proper maxima.

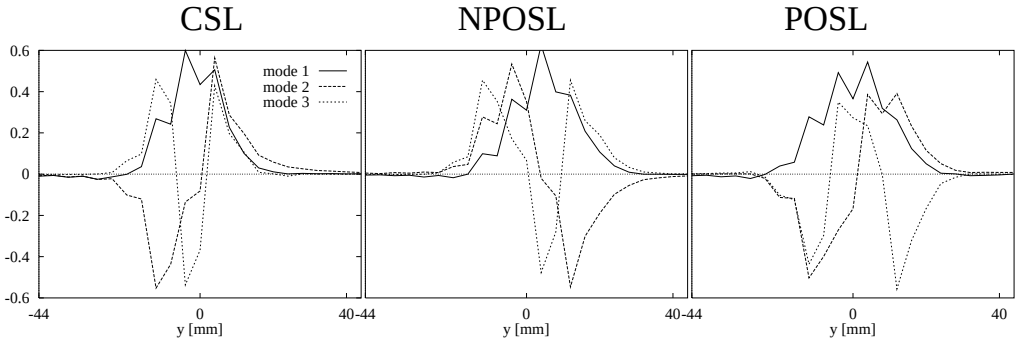

Fig. 4.33: Plots of the the eigen-vectors of the first 3 modes

Eigen-spectra

The POD allows the calculation of mode dependent spectra, the so called "eigen-spectra". The eigen-values are a function of f and not of the transversal position y. They represent the energy level of the individual modes. In fig. 4.34 the spectra of the first three modes are shown. The first mode of all three cases contains the most energy. The spectra of the first mode of the CSL shows a spike at 200 Hz which is near the frequency of the structures found in the classical spectra (this experiment had different velocity settings $\overline{U}_1$ and $\overline{U}_0$ so the peak is not at 300 Hz as in section 4.2.8, however, the dominant frequency in the appropriate spectrum was found to be 200 Hz). The two other modes contain much less energy. The first modes of the two other cases do not exhibit any characteristic frequency.

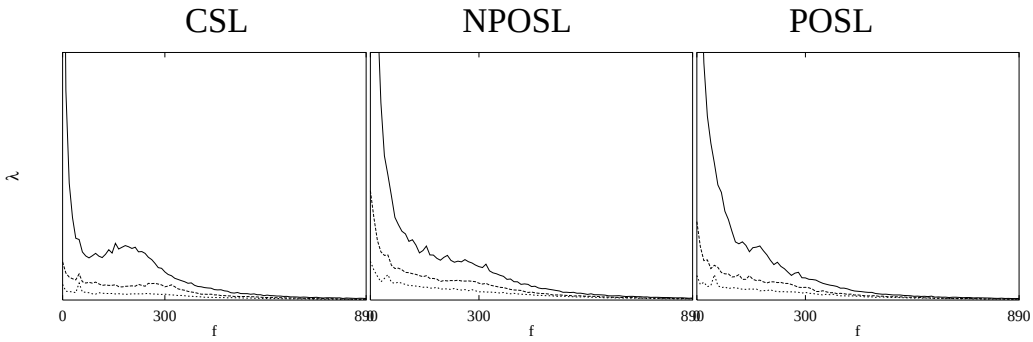

Fig. 4.34: Spectra of the eigen values (first three modes)

The application of the POD in this work covers only a minimum of its capacity, only a few details were worked out. A deeper insight into the structural organization of the flows would probably be obtained if vectorial POD and 3-D POD (use of 2 or more hot-wire rakes) would be applied. These investigations require a large amount of experimental apparatus which exceeds the scope of this work. It was shown, however, that with the scalar POD differences between the three cases can be shown.

5. Summary , conclusions and outlook

In this experimental investigation the turbulent structure and the turbulent quantities of an axisymmetric shear layer subjected to three-dimensional stationary boundary condition are presented. In the context of a classification presented in section 2.2 this condition was identified as condition II: Three-dimensionality of the basic flow configuration. This can be realized by skewing velocity vector relative to the trailing edge (i.e. the flow direction of the convection velocity is not perpendicular to the trailing edge) as were performed by e.g. Gründel [1], Spieweg [3] and Hackett & Cox [29] in plane configurations.

For this task a wind tunnel was designed including two coaxial jets with adjustible rotation. This way axisymmetric shear layers subjected to three-dimensional stationary boundary conditions were produced. Three cases were investigated:

- A shear layer between two coaxial jets with no three-dimensional stationary boundary condition (i.e. the CSL case)
- A shear layer between two coaxial jets subjected to a three-dimensional stationary boundary condition by the means of counter-rotation (i.e. the NPOSL case)
- A shear layer between two coaxial jets subjected to a three-dimensional stationary boundary condition by the means of co-rotation (i.e. the POSL case)

In order to allow comparison with planar configurations no mean streamwise vorticity ω_x in the free streams should occur. It turned out, however, that the properties of the azimuthal velocity profiles of the central jet prohibit such an comparison. The $\overline{W}$-profiles exhibited two different gradients on either side of the shear layer which were responsible for a double peak in the

radial distribution of the streamwise vorticity ω_x. This behavior was more pronounced in the POSL than in the NPOSL . In plane configurations ω_x would only be created at the interface between two skewed primary streams. It should be noted that the exit velocity profiles were found to have only one ω_x-peak at the interface between two jets so that the double peak character could be attributed to the evolution of the shear layer which changes the characteristics of the inner jet . This aspect, which is attributed to the wind tunnel, needs further clarification through measurements in the near field of the shear layer, i.e. in the range of x=0-300 mm. This could not be carried out in this work due to the lack of time.

Another interesting phenomenon is the formation of an axial velocity peak in the central jet when swirl is applied. From measurements in a smaller model tunnel with two tangential inlets it was concluded that this is an effect of the screens in the plenum chamber. The underlying fluid-dynamical mechanism needs to be analyzed through measurements of the velocity profiles in the plenum chambers upstream and downstream of the screens.

A general effect of the three-dimensional conditions is an increase of the total turbulent kinetic energy $\overline{q} = 1/3(\overline{u'^2} + \overline{v'^2} + \overline{w'^2})$. The increase in the NPOSL case was about 78 % in the NPOSL and about 18 % in the POSL case compared to the CSL case. In increase of the shear layer spreading of the same order was observed which is qualitatively in agreement with the modified spread parameter λ_ν.

Several observations indicated an increased structural complexity of the three-dimensional shear layers. Triple correlations of the POSL showed an increased radial transport of turbulent energy which is attributed to the increased structural activity. The flatness factors indicate an intermittent character at the inner shear layer front which may be due to large-scale motion. The shape and regularity of the vortex rings observed in the two-dimensional case were smeared out in the POSL and - more severe - in the NPOSL case. In the spectra an increased energy level at lower frequencies indicated that this effect must come from other structures which deform through interaction with the initially ring-shaped vortex structures.

The “pseudo flow vizualizations” based on azimuthal correlations showed the presence of oblique structures in the NPOSL and POSL cases which could be due to helical structures. Presumedly, these helical structures result from the two shear layers in the $x-y$-plane and in the $x-r$-plane which interfere with each other. This is a similar situation as the flow investigated by

Gründel [1] and Nayeri [2] (symmetric oblique shear layer, fig. 2.8b). There, a three-dimensional shear flow consisting of a wake flow in the streamwise direction ($x-y$-plane) and of a shear layer in the lateral direction $x-r$-plane was studied. In fig. 2.3 it can be seen that, on the one hand streamwise vortices, and on the other hand, the wake structures are present. As a result helical structures were formed. One of the reasons for the difficulty in vizualizing the structures in the present case is certainly the non-symmetric flow situation. Gründel [1] and Spieweg [3] found that asymmetric flow conditions inhibit the formation of well-defined flow structures.

However, the acquisition of a conclusive structural picture requires extensive experimental techniques capable to obtaining instantaneous flow information in a three-dimensional field. Such an approach is suggested to be performed with experiments in water using Laser Induced Fluorescence (LIF). The use of two radial hot wire rakes in the wind tunnel in order to perform 3-D POD as a complementary investigation is also advisable.

6. Appendix

6.1 References on swirl generating devices

Since the development of a swirl generating device was a important task in this work, a list of references is given covering this issue. It is sorted after the mechanism of swirl generation.

- rotating honeycomb[64, 17, 30]
- rotating vanes [36, 65]
- rotating tube [49, 66, 67]
- tangential inlets [68, 48, 69, 70, 71, 34, 72]
- radial inlet vanes[73, 74, 42, 75]
- twisted tapes, stationary vanes [76, 77, 78, 79, 80]

6.2 Wind tunnel dimensions

Fig. 6.1: The wind tunnel with major dimensions

Bibliography

[1] H. Gründel. *Strukturen in symmetrischen und asymmetrischen Scherschichten*. PhD thesis, Hermann-Föttinger-Institut, Technische Universität Berlin, 1995.

[2] C. N. Nayeri. Unterdrückung der Nachlaufstruktur in einer Scherschicht - Einflu einer Ausblasung, Studienarbeit, Hermann-Föttinger-Institut, Technische Universität Berlin, 1992.

[3] R. Spieweg. Strukturen in turbulenten Scherschichten mit schräger Abströmkante. Diplomarbeit, Hermann-Föttinger-Institut, Technische Universität Berlin, 1994.

[4] A. K. M. F. Hussain. Coherent structures - reality and myth. *Phys. Fluids*, 26, 2816–2850, 1983.

[5] H. E. Fiedler, C. Nayeri, R. Spieweg, and C.O. Paschereit. Three-dimensional mixing layers and their relatives. *Experimental Thermal and Fluid Science*, 16, 3–21, 1998.

[6] C. O. Paschereit, M. Schüttpelz, and H. E. Fiedler. The mixing layer between non-parallel walls. In H.-H. Fernholz and H. E. Fiedler, editors, *Advances in Turbulence II* 467–471, 1988.

[7] S. Béharelle, C. N. Nayeri, J. Delville, J.-P. Bonnet, and H. E. Fiedler. Influence of the traverse shear on the development of wake flows. In S. Gavrilakis, L. Machiels, and P.A. Monkewitz, editors, *Advances in Turbulence VI*, Fluid Mechanics and its Applications 511–512, 1996.

[8] H. Gründel and H. E. Fiedler. The mixing layer between non-parallel streams. In *Advances in Turbulence IV* 167–171. Kluwer Academic Publishers, 1993.

[9] H. E. Fiedler, A. Glezer, and I. J. Wygnanski. Control of the plane mixing layer: some novel experiments. *AIAA J.*, 112, 30–64, 1988.

[10] G. L. Brown and A. Roshko. On density effects and large structure in turbulent mixing layers. *J. Fluid Mech.*, 64, 775–816, 1974.

[11] H. E. Fiedler, K. Nottmeyer, P. P. Wegener, and S. Raghu. Schlieren photography of water. *Experiments in Fluids*, 3, 145–151, 1985.

[12] B. Dziomba and H. E. Fiedler. Effect of initial conditions on two-dimensional free shear layers. *J. Fluid Mech.*, **151**, 419–442, 1985.

[13] F. K. Browand and C. M. Ho. The mixing layer: an example of quasi two-dimensional turbulence. *J. Méch. Numér. Spécial: Turbulence Bidimensionelle* 99–120, 1983.

[14] G. N. Abramovich. *The theory of turbulent jets*. MIT Press, Cambridge, 1963.

[15] C. M. Sabin. An analytical and experimental study of the plane, incompressible, turbulent free shear layer with arbitrary velocity ratio and pressure gradient. Technical Report MD-9, Stanford Univ., Stanford, California, 1963.

[16] J. P. Johnston M. W. Plesniak, R. D. Mehta. Curved two-stream turbulent mixing layers: three-dimensional structure and streamwise evolution. *J. Fluid Mech.*, 270, 1–51, 1994.

[17] R. D. Mehta, D. H. Wood, and P. D. Clausen. Some effects of swirl on turbulent mixing layer development. *Phys. Fluids*, 3, 2716–2724, 1991.

[18] P. Bradshaw. *AGARDograph*, 169, 1973.

[19] J. Silvestrini. Master's thesis, Grenoble, 1993.

[20] H. E. Fiedler and H.-H. Fernholz. On management and control of turbulent shear flow. *Prog. Aerospace Sci.*, 27, 305–387, 1990.

[21] H. E. Fiedler. Coherent structures in turbulent flows. *Progress in Aerospace Sciences*, 25, 305–387, 1988.

[22] H. E. Fiedler. Coherent structures. *Advances in Turbulence* 320–336, 1987.

[23] H. E. Fiedler, B. Dziomba, P. Mensing, and T. Rösgen. Initiation, evolution and global consequences of coherent structures in turbulent shear flows. In J. Jimenez, editor, *The Role of Coherent Structures in Modelling Turbulence and Mixing*, volume 136 of *Lecture Notes in Physics*, Madrid, Spain, June 1981. Springer-Verlag Berlin Heidelberg New York.

[24] A. K. M. F. Hussain. Coherent structures and turbulence. *J. Fluid Mech.*, 173, 303–356, 1986.

[25] L. P. Bernal and A. Roshko. Streamwise vortex structure in plane mixing layers. *J. Fluid Mech.*, 170, 499–525, 1986.

[26] G. M. Corcos and S. J. Lin. The mixing layer: Deterministic models of a turbulent flow. part 2: The origin of three-dimensional motion. *J. Fluid Mech.*, 141, 139–178, 1984.

[27] J. C. Lasheras and H. Choi. Three-dimensional instability of a plane shear layer: an experimental study of the formation and evolution of streamwise vortices. *J. Fluid Mech.*, 189, 53–86, 1988.

[28] K. J. Nygaard and A. Glezer. Phase excitation of a plane mixing layer. *J. Fluid Mech.*, 1991.

[29] J. E. Hackett and D. K. Cox. The three-dimensional mixing layer between two grazing perpendicular streams. *J. Fluid Mech.*, 43, 77–96, 1970.

[30] Hans Gründel, Rene Spieweg, and H. E. Fiedler. The mixing layer behind a slanted trailing edge. *submitted to ETC94*, 1994.

[31] V. Kibens, R. W. Wlezien, and J. T. Kegelman. Trailing-edge sweep and three-dimensional vortex interactions in jets and mixing layers. *AGARD*, CP 438, 1988.

[32] P. Atsavapranee and M. Gharib. A plane mixing layer with cross-shear. *Phys. Fluids*, 6(9), 2880–2882, September 1994.

[33] W. Steenbergen. *Turbulent pipe flow with swirl*. PhD thesis, Eindhoven University of Technology, 1995.

[34] M. Samet and S. Einav. Mean value measurements of a turbulent swirling-jet. *AIAA J.*, 26, no. 5, 619–620, 1988.

[35] R. Taghavi, E. J. Rice, and S. Farokhi. Controlled excitation of a cold turbulent swirling free jet. *Journal of Vibration, Stress, and Reliability in Design*, 110, 234–237, april 1988.

[36] J. Panda and D. K. McLaughlin. Experiments on the instabilities of a swirling jet. *Phys. Fluids*, 6(1), 263–276, 1994.

[37] J. E. Martin and E. Meiburg. The nonlinear evolution of swirling jets. *Meccanica*, 29, 331, 1994.

[38] P. I. Singh and M. S. Uberoi. Experiments on vortex stability. *Phys. Fluids*, 19(12), December 1976.

[39] A. Michalke. Instabilitäten eines kompressiblen, runden Freistrahls unter Berücksichtigung des Einflusses der Strahlgrenzschichtdicke. *Zeitschrift für Flugwissenschaften und Weltraumforschung*, 9, 319–321, 1971.

[40] Ramjee V. and Hussain A. K. M. F. Influence of the axisymmetric contraction ratio on free-stream turbulence. *J. Fluids Eng.*, 16, June 1976.

[41] T. Morel. Comprehensive design of axisymmetric wind tunnel contractions. *J. Fluids Eng.*, 5, 225–233, 1975.

[42] F. C. Gouldin, J. S. Depsky, and S.-L. Lee. Velocity field characteristics of a swirling flow combuster. *AIAA J.*, 23, no. 1, 95–102, 1985.

[43] W. S. Saric. Görtler vortices. *Ann. Rev. Fluid Mech.*, 26, 379–409, 1994.

[44] J. Delville, S. Bellin, J. H. Garem, and J.-P. Bonnet. Analysis of structures in a turbulent, plane mixing layer by use of a pseudo flow visualization method based on hot-wire anemometry. In H.-H. Fernholz and H. E. Fiedler, editors, *Advances in Turbulence 2* 251–256. Springer-Verlag, 1988.

[45] L. S. G. Kovasnay. *High Speed Aerodynamics and Jet Propulsion*. Princeton University Press, 1954.

[46] J.-H. Kim. *Wirbelstärkemessungen in einer turbulenten Scherschicht*. Dissertation, Hermann-Föttinger-Institut, Technische Universität Berlin, 1989.

[47] L. Jacquin, O. Leuchter, and P. Geffroy. Use of quadripole hotwire probes for studying turbulent flows. *La Recherche Aérospatiale*, (6), 427–444, 1995.

[48] N. A. Chigier and A. Chervinsky. Experimental investigation of swirling vortex motion in jets. *J. of Applied Mech., Trans. ASME* 445–451, June 1967.

[49] W. G. Rose. A swirling round turbulent jet. *J. Applied Mech.* 615–625, December 1962.

[50] D. G. Lilley. Swirl flows in combustion: A review. *AIAA J.*, 15, 1063–1078, 1977.

[51] I. Wygnanski and H. E. Fiedler. The two–dimensional mixing region. *J. Fluid Mech.*, 31, 327–361, 1970.

[52] D. Oster and I. Wygnanski. The forced mixing layer between parallel streams. *J. Fluid Mech.*, 123, 91–130, 1982.

[53] R. D. Metha and R. V. Westphal. Near-field turbulence properties of single- and two-stream plane mixing layers. *Experiments in Fluids*, 4, 257–266, 1986.

[54] J. Delville, S. Bellin, and J.-P. Bonnet. Use of the proper orthogonal decomposition in a plane turbulent mixing layer. In M. Lesieur and O. Metais, editors, *Turbulence and Coherent Structures* 75–90. Kluwer Academic Publisher, 1990.

[55] A. A. Townsend. *The Structure of Turbulent Shear Flow*. Cambridge Monographs on Mechanics and Applied Mathematics. Cambridge University Press, 1956.

[56] J. O. Hinze. *Turbulence*. McGraw-Hill Series in Mechanical Engineering. McGraw-Hill, 1959.

[57] S. Bellin, J. Delville, E. Vincendeau, J. H. Garem, and J. P. Bonnet. Large scale structure characterization in a 2d mixing layer by pseudo-flow-visualization and delocalized conditional sampling. In J. P. Bonnet and M. N. Glauser, editors, *Eddy Structure Identification in Free Turbulent Shear Flows*, volume 21 of *Fluid Mechanics and its Applications* 91–101. Kluwer Academic Publishers, 1992.

[58] J. Delville, S. Bellin, and J. P. Bonnet. Use of the proper orthogonal decomposition in a plane turbulent mixing layer. In O. Metais and M. Lesieur, editor, *Turbulence and Coherent Structures*. Kluwer Academic Publishers, 1989.

[59] J. Delville. *La Décomposition Orthogonal aus valeur propres et l'analyse de l'organisation tridimensionelle des écoulement trubulents cisaillés libres*. PhD thesis, Université de Poitiers, 1995.

[60] J. L. Lumley. The structure of inhomogenous turbulent flows. In Yaglom and Tatarski, editors, *Atmospheric Turbulence and Radio wave Propagation*. 1967.

[61] G. Berkooz, P. Holmes, and J. Lumley. The proper orthogonal decomposition in the analysis of turbulent flows. *Annual Review of Fluid Mechanics*, 25, 1993.

[62] D. Hilberg, W. Lazik, and H. E. Fiedler. The application of classical POD and snapshot POD in a turbulent shear layer with periodic structures. In *Eddy Structure Identification in Free Turbulent Shear Flows*, Poitiers, october 1992. IUTAM Symposium.

[63] J. Delville. Characterization of the organization in shear layers via proper orthogonal decomposition. In J.-P. Bonnet and M. N. Glauser, editors, *Eddy Structure Identification in Free Turbulent Shear Flows*. Kluwer Academic Publ., 1993.

[64] D. R. Weske and G. Y. Sturov. experimental study of turbulent swirled flows in a cylindrical tube. *Fluid Mechanics-Soviet Research*, 3, no.1, 1974.

[65] J. W. Elsner and L. Kurzak. Characteristics of turbulent flow in slightly heated free swirling jets. *J. Fluid Mech.*, 180, 147–169, 1987.

[66] B. D. Pratte and J. F. Keffer. the swirling turbulent jet. *J. Basic Eng.* 739–748, 1972.

[67] S. Komori and H. Ueda. Turbulent flow structure in the near field of a swirling round free jet. *Phys. Fluids*, 28(7), 2075–2082, july 1985.

[68] R. Taghavi, E. J. Rice, and S. Farokhi. Large amplitude acoustic excitation of swirling turbulent jets. Technical Report 89-0970, AIAA paper, 1989.

[69] T. F. Dixon, J. S. Truelove, and T. F. Wall. aerodynamic studies on swirled coaxial jets from nozzles with divergent quarls. *J. Fluids Eng.*, 105, 197–203, 1983.

[70] M. M. Ribeiro and J. H. Whitelaw. coaxial jets with and without swirl. *J. Fluid Mech.*, 96(4), 769–795, 1980.

[71] V. M. Domkundwar, V. Sriramulu, and M. C. Gupta. analysis of swirling recirculating reacting turbulent jets passing through diffusers. *Combustion and Fluid*, 33, 241–249, 1978.

[72] W.L.H. Hallett. swirl generator for independent variation of swirl and velocity profile. *AIAA J.*, 24, no. 7, 1212–1213, 1986.

[73] K. S. Yajnik and M. V. Subbaiah. Experiments on swirling turbulent flows. part 1: similarity in swirling flows. *J. Fluid Mech.*, 60(4), 665–687, 1973.

[74] B. T. Vu and F. C. Gouldin. Flow measurements in a model swirl combuster. *AIAA J.*, 20, 642–651, 1980.

[75] J. D. Mattingly and G. C. Oates. An experimental investigation of the mixing of coannular swirling flows. *AIAA J.*, 24(5), 785–792, 1986.

[76] F. Takahashi, M. D. Vangness, and V. M. Belovich. Conditional LDV measurements in swirling and non-swirling coaxial turbulent air jets for model validation. Technical Report 92-0580, AIAA paper, 1992.

[77] H. Y. Lu, J. W. Ramsay, and D. L. Miller. Noise of swirling exhaust jets. *AIAA J.*, 15, 642–646, 1977.

[78] E.W. Grandmaison and H.A. Becker. Turbulent mixing in free swirling jets. *The Canadian Journal of Chemical Engineering*, 60, 76–82, February 1982.

[79] J. P. Sislian and R. A. Cusworth. Measurements of mean velocity and turbulent intensities in a free isothermal swirling jet. *AIAA J.*, 24(2), 303–309, 1986.

[80] R. M. C. So, S. A. Ahmed, and H. C. Mongia. Jet characteristics in confined swirling flow. *Experiments in Fluids*, 3, 221–230, 1985.

List of Figures